Adaptive Error Control for Stratospheric Long-Distance Optical Links

Von der Fakultät 5 - Informatik, Elektrotechnik und Informationstechnik
der Universität Stuttgart zur Erlangung der Würde eines
Doktor-Ingenieurs (Dr.-Ing.) genehmigte Abhandlung

Vorgelegt von

Swaminathan Parthasarathy

aus Madurai, Indien

Hauptberichter:	Prof. Dr.-Ing. Andreas Kirstädter
Mitberichter:	Prof. Dr.-Ing. Stephan ten Brink
Tag der mündlichen Prüfung:	22.04.2024

Institut für Kommunikationsnetze und Rechnersysteme
der Universität Stuttgart
2024

In loving memory of my dear parents.

Abstract

Free-space optical (FSO) communication plays a crucial role in aerospace technology, utilizing lasers to establish high-speed, wireless connections over long distances. FSO surpasses conventional RF wireless technology in various aspects and supports high-data-rate connectivity for services such as Internet access, data transfer, voice communication, and image transfer. High-Altitude Platforms (HAPs) have emerged as ideal hosts for FSO communication networks, offering ultra-high data rates for applications like high-speed Internet, video conferencing, telemedicine, smart cities, and autonomous driving. FSO via HAPs ensures minimal latency, making it suitable for real-time tasks like remote surgery and autonomous vehicle control. The swift, long-distance communication links with low delays make FSO-equipped HAPs ideal for RF-congested areas, providing cost-effective solutions in remote regions and contributing to environmental monitoring.

This thesis explores the use of adaptive code-rate Hybrid Automatic Repeat Request (HARQ) methods and channel state information (CSI) to improve the transmission efficiency of Free-Space Optical (FSO) links between High Altitude Platforms (HAPs). The study looks at channel problems like atmospheric turbulence and static pointing errors, with a focus on the weak fluctuation regime of atmospheric turbulence. It explores the reciprocal behavior in bidirectional FSO channels to improve performance efficiency, providing evidence of channel reciprocity. The research proposes the use of HARQ, an adaptive Reed-Solomon (RS) code-rate technique, and different CSI types to address these impairments. Simulations of different situations are used to test how well these methods work. This helps us learn more about how efficient HARQ protocols are in inter-HAP FSO links, how important different CSI are in adaptive rate HARQ, and possible ways to make the system more efficient. This thesis looks at the channel model for inter-High Altitude Platform (HAP) Free-Space Optical (FSO) links in great detail, taking atmospheric conditions and static pointing errors into account. The channel is modeled as a lognormal fading channel under a weak fluctuation regime. The principle of channel reciprocity and the measures used to quantify it are discussed, providing a foundational understanding for the subsequent investigations.

Forward Error Correction (FEC) schemes, with a specific emphasis on the Reed-Solomon (RS) scheme, and various Automatic Repeat reQuest (ARQ) schemes are thoroughly examined. A meticulous comparison of different ARQ schemes highlights that Selective Repeat ARQ (SR-ARQ) is the most efficient for high-error-rate channels, making it the preferred choice for inter-HAP FSO channels. Conversely, Stop and Wait ARQ (SW-ARQ) and Go-Back-N ARQ (GBN-ARQ) are found to be less suitable for these channels. An innovative approach is introduced, leveraging various types of Channel State Information (CSI) to adjust the Reed-Solomon Forward Error Correction (FEC) code-rate. Four types of CSI: perfect CSI (P-CSI), reciprocal CSI (R-CSI), delayed CSI (D-CSI), and fixed mean CSI (F-CSI) are employed. The adaptation of the Reed-Solomon FEC code-rate, aligned with Selective Repeat ARQ, is explored, and the optimal power selection is identified through rigorous analysis. It shows simulation models that use OMNET++ and gives information about the inter-HAP channel and the event-based selective repeat HARQ model.

The study demonstrates reciprocity in the longest recorded ground-to-ground bidirectional Free-Space Optical (FSO) link, holding promise to mitigate signal scintillation caused by atmospheric turbulence. It evaluates the performance of different ARQ protocols and adaptive Hybrid Automatic Repeat Request (HARQ) schemes in inter-HAP FSO communication systems. The results show how channel state information, turbulence in the atmosphere, and pointing errors affect the performance of the system. They also suggest ways to improve system efficiency, such as using CSI prediction and soft combining. These findings offer valuable insights for the design and optimization of ARQ and HARQ schemes in inter-HAP FSO communication systems and suggest promising avenues for future research.

Kurzfassung

Die optische Freiraumkommunikation (FSO) ist in der Luft- und Raumfahrttechnik von entscheidender Bedeutung, da sie Laser nutzt, um drahtlose Hochgeschwindigkeitsverbindungen über große Entfernungen herzustellen. Für Internetzugang, Datenübertragung, Sprachkommunikation und Bildübertragung ermöglicht FSO Verbindungen mit hoher Datenrate. Zudem übertrifft die konventionelle drahtlose RF-Technologie in verschiedenen Punkten. High Altitude Platforms (HAPs) haben sich als ideale Träger für FSO-Netzwerke etabliert und bieten ultrahohe Datenraten für Anwendungen wie High-Speed-Internet, Videokonferenzen, Telemedizin, Smart Cities und autonomes Fahren. FSO über HAPs gewährleistet minimale Latenzzeiten und eignet sich daher perfekt für Echtzeitanwendungen wie Fernoperationen und die Steuerung autonomer Fahrzeuge. Die schnellen, weitreichenden Kommunikationsverbindungen mit geringen Verzögerungen machen HAPs mit FSO ideal für RF-überlastete Gebiete, bieten kostengünstige Lösungen in abgelegenen Regionen und unterstützen die Umweltüberwachung.

Diese Arbeit untersucht den Einsatz von adaptiven Code-Rate Hybrid Automatic Repeat Request (HARQ) Methoden und Channel State Information (CSI) zur Verbesserung der Übertragungseffizienz von Free-Space Optical (FSO) Verbindungen zwischen High Altitude Platforms (HAPs). Die Studie befasst sich mit Kanalproblemen wie atmosphärischen Turbulenzen und statischen Ausrichtungsfehlern, wobei der Schwerpunkt auf dem schwachen Fluktuationsbereich der atmosphärischen Turbulenzen liegt. Sie erforscht das reziproke Verhalten in bidirektionalen FSO-Kanälen, um die Leistungseffizienz zu verbessern, und liefert Beweise für die Reziprozität der Kanäle. Die Forschung schlägt die Verwendung von HARQ, einer adaptiven Reed-Solomon (RS)-Coderate-Technik und verschiedenen CSI-Typen vor, um diesen Beeinträchtigungen zu begegnen. Anhand von Simulationen verschiedener Situationen wird getestet, wie gut diese Methoden funktionieren. Dies hilft uns, mehr darüber zu erfahren, wie effizient HARQ-Protokolle in Inter-HAP-FSO-Verbindungen sind, wie wichtig verschiedene CSI bei adaptiver HARQ-Rate sind und welche Möglichkeiten es gibt, das System effizienter zu machen. In dieser Arbeit wird das Kanalmodell für optische Freiraumverbindungen (FSO) zwischen High Altitude Platforms (HAP) unter Berücksichtigung der atmosphärischen Bedingungen und statischer Ausrichtungsfehler eingehend untersucht. Der Kanal wird als lognormaler Fading-Kanal mit schwacher Fluktuation modelliert. Das Prinzip der Kanalreziprozität und die zu ihrer Quantifizierung verwendeten Maße werden erörtert, um ein grundlegendes Verständnis für die nachfolgenden Untersuchungen zu schaffen.

Forward Error Correction (FEC) Schemata, mit besonderem Schwerpunkt auf dem Reed-Solomon (RS) Schema, und verschiedene Automatic Repeat reQuest (ARQ) Schemata werden gründlich untersucht. Ein sorgfältiger Vergleich verschiedener ARQ-Verfahren zeigt, dass Selective Repeat ARQ (SR-ARQ) bei Kanälen mit hoher Fehlerrate am effizientesten ist und daher die bevorzugte Wahl für Inter-HAP-FSO-Kanäle darstellt. Umgekehrt sind Stop and Wait ARQ (SW-ARQ) und Go-Back-N ARQ (GBN-ARQ) für diese Kanäle weniger geeignet. Es wird ein innovativer Ansatz eingeführt, der verschiedene Arten von Kanalzustandsinformationen (CSI) nutzt, um die Reed-Solomon-FEC-Code-Rate (Forward Error Correction) anzupassen. Es werden vier Arten von CSI

verwendet: perfekte CSI (P-CSI), reziproke CSI (R-CSI), verzögerte CSI (D-CSI) und CSI mit festem Mittelwert (F-CSI). Die Anpassung der Reed-Solomon FEC Coderate, die mit Selective Repeat ARQ abgestimmt ist, wird untersucht und die optimale Leistungsauswahl wird durch eine strenge Analyse ermittelt. Es werden Simulationsmodelle gezeigt, die OMNET++ verwenden und Informationen über den Inter-HAP-Kanal und das ereignisbasierte Selective Repeat HARQ-Modell liefern.

Die Studie stellt die Reziprozität in der längsten aufgezeichneten bidirektionalen optischen Boden-zu-Boden-Verbindung (FSO) fest, die vielversprechend ist, um die durch atmosphärische Turbulenzen verursachte Signal-Szintillation zu mildern. Es wird die Leistung verschiedener ARQ-Protokolle und adaptiver Hybrid Automatic Repeat Request (HARQ)-Schemata in Inter-HAP-FSO-Kommunikationssystemen bewertet. Die Ergebnisse zeigen, wie Kanalzustandsinformationen, Turbulenzen in der Atmosphäre und Ausrichtungsfehler die Leistung des Systems beeinflussen. Sie schlagen auch Möglichkeiten zur Verbesserung der Systemeffizienz vor, wie z. B. die Verwendung von CSI-Vorhersagen und Soft Combining. Diese Ergebnisse bieten wertvolle Einblicke für die Entwicklung und Optimierung von ARQ- und HARQ-Verfahren in Inter-HAP-FSO-Kommunikationssystemen und zeigen vielversprechende Wege für die zukünftige Forschung auf.

Acknowledgments

This thesis showcases the findings of the research I conducted at the Institute of Communications and Navigation (IKN) within the German Aerospace Center (DLR), located in Oberpfaffenhofen, Germany. The research was made possible through the full funding provided by the DLR-DAAD Research fellowship program, which is jointly implemented by the DLR and the German Academic Exchange Service (DAAD). I would also like to express my gratitude to the IKN Institute at DLR for their generous financial support, as well as their provision of office, lab, and manpower resources. The opportunity to explore various fascinating and challenging subjects was made possible by the support of DAAD-DLR, and I am thankful for this opportunity.

DAAD Deutscher Akademischer Austauschdienst
German Academic Exchange Service

DLR Deutsches Zentrum für Luft- und Raumfahrt
German Aerospace Center

I would like to express my sincere gratitude to Prof. Andreas Kirstädter for his supervision throughout my work. I appreciate his time, guidance, and extremely helpful constructive criticism. His valuable suggestions, ideas, and advice have made a significant contribution to this thesis. In addition, I would like to express my gratitude to Prof. Dr. Stephan ten Brink for his role as my secondary examiner.

Furthermore, I extend my thanks to Dr.-Ing. Dirk Giggenbach for the fruitful discussions, valuable feedback, and constructive comments on my research. I am grateful for his willingness to act as my supervisor at the DLR Institute. Special thanks also go to my colleagues at the Optical Communications Group (OCG) at DLR, both current and former, as well as the administrative and technical staff. The pleasant working atmosphere, diverse discussions, and meetings have been an unforgettable experience for me.

Lastly, I would like to express my deepest gratitude to my wife and daughter for their unwavering support, care, and love, as well as their trust in me. I consider myself fortunate to have them, and I dedicate this work to them. I also want to extend my special thanks to my family and friends who have always been there for me, supporting me in every decision I've made.

2024

Swaminathan Parthasarathy

Contents

List of Figures

Page

List of Tables

Page

Nomenclature

Acronyms

ACK	Acknowledgment
APD	Avalanche Photo Detector
ARQ	Automatic Repeat Request
ASN	Acknowledgement Sequence Number
BDP	Bandwidth Delay Product
BEP	Bit Error Probability
BER	Bit Error Rate
CACK	Cumulative Acknowledgment
CCF	Correlation Coefficient
CRC	Cyclic Redundancy Check
CSI	Channel State Information
CSIT	Channel State Information at the Transmitter
D-CSI	Delayed Channel State Information
DD	Direct detection
ECC	Error Control Coding
F-CSI	Fixed Mean Channel State Information
FEC	Forward Error Correction
FSO	Free Space Optics (Optical)
GBN-ARQ	Go-Back-N ARQ
Gbps	Gigabits per second
GEO	Geosynchronous Equatorial Orbit
H-V	Hufnagel-Valley model
HAP	High Altitude Platform
HARQ	Hybrid Automatic Repeat Request
HWHM	Half Width Half Maximum
IM/DD	Iintensity modulation and Direct detection
IR	Incremental Redundancy
IRT	Index of Refraction
ISI	Intensity Scintillation Index
ISL	Inter-Satellite Link

LDPC	Low-Density Parity Check
LN	Log Normal Distribution
LOS	Line Of Sight
NACK	Negative Acknowledgment
NED	Network Description
NMSE	Normalized Mean Squared Error
NRZ	Non-Return-to-Zero
OIPL	Optical Inter-Platform Link
OMNET++	Objective Modular Network Testbed in C++
OOK	On-Off Keying
OSI	Open Systems Interconnection
OSNR	Optical Signal-to-Noise Ratio
P-CSI	Perfect Channel State Information
PDF	Probability Density Function
PEP	Packet Error Probability
PIB	Power in Bucket
PILab	Propagation and Imaging Lab
PSC	Polar Stratospheric Cloud
PSI	Power Scintillation Index
PVGeT	Power Vector Generation Tool
R-CSI	Reciprocal Channel State Information
RF	Radio Frequency
RFE	Receiver Front End
RMS	Root Mean Square
RSN	Received Packet Sequence Number
RTT	Round-trip time (s)
SACK	Selective Acknowledgment
SDL	Specification and Description Language
SEP	Symbol Error Probability
SI	Scintillation Index
SR-ARQ	Selective Repeat ARQ
SW-ARQ	Stop and Wait ARQ
TE	Throughput/ Transmission Efficiency
ToF	Time of Flight
UAV	Unmanned Aerial Vehicle

Symbols

$2t$	number of parity (symbols)
$\bar{I}$	average intensity
β_0^2	spherical wave Rytov variance
δ_x	resolutions along x of the image
δ_y	resolutions along y of the image
λ	wavelength (m)
$\left(\frac{E_b}{N_0}\right)_{coded}$	required E_b/N_0 coded (dB)
$\left(\frac{E_b}{N_0}\right)_{uncoded}$	required E_b/N_0 uncoded (dB)
$\left(\overline{P}_{rx}\right)_{coded}$	required mean received power coded (nW)
$\left(\overline{P}_{rx}\right)_{uncoded}$	required mean received power uncoded (nW)
$\langle . \rangle$	time averaging function
$\langle \rangle$	ensemble average (sample mean)
μ_A	mean of received optical power at terminal A
μ_B	mean of received optical power at terminal B
$\overline{BEP}$	mean Bit Error Probability (unitless)
$\overline{P}_{rx}$	mean received power (Watt)
ρ	ratio of round trip time over correlation time of the channel (unitless)
ρ_i	intensity coherence width
σ_A	standard deviation of received optical power at terminal A
σ_B	standard deviation of received optical power at terminal B
$\sigma_I^2(0)$	scintillation index of a point receiver
$\sigma_I^2(D_{rx})$	scintillation index of a receiving aperture with diameter D_{rx}
σ_P^2	power scintillation index (unitless)
σ_{rms}^2	pointing error variance (unitless)
σ_R^2	plane wave Rytov variance
σ_R^2	plane wave Rytov variance
τ	correlation time of the channel (s)
ζ	zenith angle
A	value of refractive index structure parameter at ground ($m^{-2/3}$)
A_{AF}	aperture averaging factor
A_i	received optical power over time measured at terminal A
B	Bandwidth of the channel (Hertz)

B_i	received optical power over time measured at terminal B
C	channel capacity (bps)
c	speed of light in the vacuum (m/s)
$C_n^2(h_0)$	reference refractive index structure value at h_0 ($m^{-2/3}$)
C_T^2	temperature structure parameter ($deg^2/m^{2/3}$)
d	distance of a phase screen from the transmitter (m)
D_{rx}	diameter of receiver aperture (m)
D_{rx}	receiver aperture diameter
E_b	energy per information bit
$erfc$	complementary error function
G	coding gain (dB)
G_h	graze height of HAP
h	altitude of the link (m)
h_0	reference height above ground (m)
h_L	height profile above ground (m)
h_A	height above sea level at which the terminal-A is placed (m)
h_B	height above sea level at which the terminal-B is placed (m)
H_{hap}	HAP height
I	irradiance (intensity) of the optical wave
k	number of data symbols being encoded (symbols)
k	optical wave number (m^{-1})
L	inter-HAP link distance (m)
N	Average power of the noise and interference over the bandwidth (Watt or volts-squared)
n	total number of code symbols in the encoded block (symbols)
N_0	noise spectral density at the receiver
N_x	number of pixels to shift along the direction x
N_y	number of pixels to shift along the direction y
P	atmospheric pressure (bars)
P	received optical power (W)
p	power law parameter (unitless)
P_0	mean optical power (W)
$Q-factor$	qualitative factor of the receiver performance (unitless)
R	data transmission at a line rate (b/s)

R_{net}	net data rate (bps)
S	Average received signal power over the bandwidth (Watt or volts-squared)
T	temperature (kelvin)
t	symbol error correcting capability of RS code
t_{packet}	transmission time (seconds)
t_{RTT}	round-trip time (seconds)
t_{TOF}	time-of-flight
v	orthogonal wind speed (in m/s)
v_g	ground wind speed (m/s)
v_x	wind speeds projected to the directions x (m/s)
v_y	wind speeds projected to the direction y (m/s)
w	RMS wind speed or pseudo wind (m/s)
w_s	slew rate of the optical beam (m/s)
w_0	full $1/e^2$ divergence angle (rad)
W_s	ARQ window size (packets)
z	propagation path along the inter-HAP link (m)

1 Introduction

In this chapter, the topics of Free Space Optical (FSO) communication, High Altitude Platforms (HAPs), and Error Control Coding (ECC) are introduced in separate sections, namely Section 1.1, Section 1.2, and Section 1.3. Additionally, the purpose, intent, and significant contributions of the research are outlined in Section 1.4, and the thesis outline is provided in Section 1.5.

1.1. Free Space Optical (FSO) Communication

Free-space optical (FSO) communication is a crucial technology in the aerospace industry, enabling multi-gigabit-per-second (multi-Gbps) communications [1, 2, 3]. FSO lasercom utilizes lasers to establish line-of-sight, wireless connections between distant locations, offering distinct advantages over conventional Radio Frequency (RF) wireless technology. These advantages include higher data rates, low probability of interception, low energy requirements, and compact form factors. The capabilities of FSO align with the increasing demand for high-data-rate connectivity, catering to services such as Internet access, interactive data transfer, voice transfer, and image transfer [4].

FSO applications are diverse, serving satellites, high-altitude platforms (HAPs), unmanned aerial vehicles (UAVs), aircraft, and ground stations in both civilian and military domains. Examples of FSO applications include inter-satellite links (ISLs), deep space missions, UAV-to-UAV links, and data links from geostationary satellites (GEO) to terrestrial ground stations. FSO connections excel in scenarios where lightweight platforms, high data links, and fiber-optic connections are impractical, such as inter-building city links and space links [5, 4, 6, 2, 7, 8, 9]. Despite atmospheric challenges like scintillation, atmospheric turbulence, weather conditions, obstructions, dispersion, beam wandering, absorption, and interference [10, 11, 3, 12], FSO outperforms conventional radio communication by delivering multi-gigabit data rates and overcoming interference and bandwidth limitations [2]. By providing faster data transfer rates and a secure communication option, FSO has the potential to revolutionize communication systems.

1.2. High Altitude Platforms (HAPs)

High Altitude Platforms (HAPs) are unmanned aerial vehicles or airships that can be permanently deployed and operated independently across diverse locations [13, 14, 15, 16, 17, 18, 19]. They serve as versatile bases for various applications, including mobile user data connectivity, remote sensing, earth observation, and communication hubs. HAPs offer strategic deployment capabilities, even in crisis zones, and can be easily modified for maintenance and payload requirements. They operate within the lower stratosphere, above civil air routes, jet streams, and clouds, while remaining below orbiting satellites. HAPs can exist as unpowered balloons or unmanned, powered airships. Airships, despite their challenges during takeoff and landing due to dynamic drag, have the advantage of accommodating substantial payloads and generating power through solar cells.

Optical Inter-Platform Links (OIPL) have emerged as a technology for enabling high-speed communication connections between stratospheric platforms. HAPs, operating at altitudes of 17 to 22 kilometers and capable of remaining airborne for months, are well-suited for communication, surveillance, and environmental monitoring applications. OIPL-based inter-HAP communication scenarios can be realized above cloud ceilings [5, 16, 15]. These platforms possess the endurance required for extended flight periods. Optical inter-platform links establish efficient and high-speed communication pathways among stratospheric platforms. Leveraging their capacity for substantial payloads and solar-powered energy generation, HAPs offer distinct advantages. However, their

significant size poses challenges during flight and landing due to dynamic drag. An illustrative example of an inter-HAP communication scenario employing optical links above cloud ceilings can be seen in Figure 1.1.

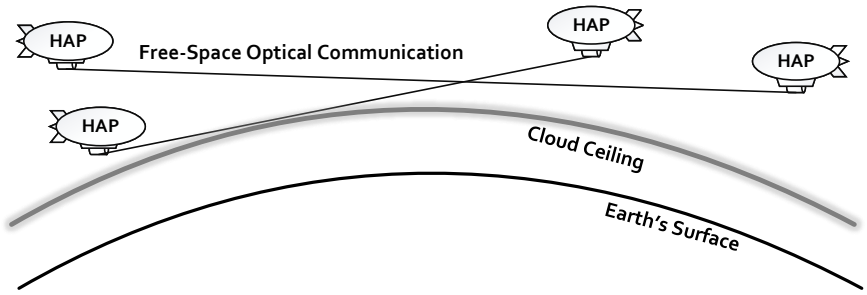

Figure 1.1.: Illustration of inter-HAP scenarios with stratospheric links above cloud ceiling.

High-Altitude Platforms (HAPs) have emerged as a promising solution for Free-Space Optical (FSO) communication networks [13, 18, 19]. Positioned at elevated altitudes, HAPs provide an optimal foundation for FSO communication, supporting ultra-high data rates exceeding several gigabits per second. This capability serves diverse applications, from high-speed internet and video conferencing to telemedicine, smart cities, and autonomous driving. FSO communication via HAPs boasts minimal latency, rendering it suitable for real-time tasks like remote surgery and autonomous vehicle control. HAPs ensure swift communication links spanning tens of kilometers, with delays below 1 millisecond. The immunity of FSO to interference positions HAPs equipped with FSO transceivers as ideal for RF-congested environments such as urban centers and military zones. For critical domains like national security, disaster response, and remote operations, dependable communication is paramount. Furthermore, FSO via HAPs presents cost-effective solutions, particularly in remote or inaccessible regions, negating the need for expensive ground infrastructure. This technology also serves as a substitute for RF-based satellite communication, curtailing conventional communication costs. Leveraging FSO transceivers, HAPs find utility in environmental monitoring tasks like detecting greenhouse gases, ensuring air quality, and observing weather patterns, catering to sectors like environmental monitoring, agriculture, and oil and gas [14, 16, 20, 21, 22, 23].

While projects like Google Loon [24, 25] and Facebook's Internet.org [26] employed optical free-space links for remote internet access, only Google Loon utilized FSO technology. Although Google Loon ceased operations in 2021, Internet.org continues to operate in select regions despite regulatory challenges. HAPs, with their advantages encompassing rapid communication, low latency, reliability, affordability, and environmental monitoring, are poised to play a pivotal role in the future of FSO communication networks. Ongoing research and development efforts are expected to further enhance the capabilities of HAPs equipped with FSO transceivers in the next wave of communication technologies.

1.3. Error Control Coding

According to Claude Shannon [27],

> *"The fundamental problem of communication is that of reproducing at one point either exactly or approximately a message selected at another point"*

In communication systems, the presence of channel impairments can lead to transmission errors, resulting in the reception of incorrect information. To address this issue, Error Control Coding (ECC) techniques are employed. ECC consists of two main phases: error detection and error correction. Error correction schemes include Forward Error Correction (FEC) and Automatic Repeat Request (ARQ), while error detection schemes encompass parity codes, checksums, and Cyclic Redundancy Check (CRC). FEC is a method for error correction that can identify and rectify a certain number of errors in transmitted data without requiring retransmission [27, 28]. On the other hand, ARQ is an adaptive mechanism that initiates re-transmission only when errors occur, utilizing a feedback channel. Although ARQ provides better error performance in certain scenarios than FEC, it leads to lower overall throughput. Additionally, ARQ requires less complex decoding equipment for error detection compared to error correction. Hybrid ARQ combines the advantages and disadvantages of FEC and ARQ, making it a more efficient utilization of the channel [29, 30]. A HARQ system [31, 32, 33], combining an FEC subsystem within an ARQ system, decreases retransmissions by fixing received packet errors, boosting throughput. If FEC fails, ARQ improves reliability, hence, combining FEC and ARQ offers higher reliability and throughput than using either system alone. According to [34, 32, 33], two common types of HARQ processes exist, each determined by how the receiver deals with packets received with errors: HARQ-Type I: If an error is detected in a received packet after a transmission attempt, it is discarded. HARQ-Type II: When a packet with errors is received, it's stored in a buffer after every transmission attempt and then combined with subsequent transmitted packets to boost the efficiency of the FEC code. Ongoing research and development efforts continue to enhance the capabilities of ECC techniques in communication systems. HARQ schemes are discussed in detail in Section 3.3.4.

1.4. Research Questions and Contributions

This thesis investigates the application of adaptive code-rate Hybrid Automatic Repeat Request (HARQ) methods and channel state information (CSI) to boost the transmission efficiency of inter-High Altitude Platform (HAP) Free-Space Optical (FSO) links. The study's main areas of focus are structured into three research questions and corresponding contributions:

1. **Determining Channel Impairments and Scenario Refinement:** This dissertation identifies the channel impairments impacting inter-HAP FSO links, including atmospheric turbulence and static pointing errors. A particular emphasis is placed on the weak fluctuation regime of atmospheric turbulence, where the scintillation index can be effectively modeled.

2. **Exploiting Reciprocal Behavior in Bidirectional FSO Channels for Enhanced Performance Efficiency:** The research explores the reciprocal behavior in bidirectional FSO channels as a means to improve performance efficiency of HARQ schemes. It provides both experimental and simulation-based proof of channel reciprocity, showing that the transmitter can use low-delay CSI to manage adaptive link errors in inter-HAP FSO links.

3. **Choosing Suitable HARQ Technology and Dynamic Code Rate Adaptation Using CSI to Boost Performance and Address Inter-HAP FSO Channel Impairments:** The study proposes the application of HARQ along with an adaptive Reed-Solomon (RS) code-rate technique and different types of CSI. Furthermore, it introduces an OMNET++-based simulation model to simulate this proposed strategy.

The dissertation assesses the effectiveness of the suggested concepts via simulations of inter-HAP FSO links under various scenarios, taking into account parameters for both traditional and reciprocal channels. It provides a performance evaluation of the adaptive Reed-Solomon (RS) code-rate HARQ method, comparing its effectiveness across different inter-HAP FSO scenarios and CSI types. In essence, the dissertation enhances our comprehension of the efficiency of HARQ protocols in inter-HAP FSO links, the pivotal role of various CSI in adaptive rate HARQ, and potential solutions for system efficiency. The findings from this dissertation research have been disseminated through numerous conference proceedings, with citations including [35, 36, 37, 38, 39, 40, 41]. These are further detailed in Appendix A.

1.5. Thesis Outline

This section provides an overview of the dissertation, which is organized as follows:

Chapter 1: This introductory chapter presents the motivation behind the thesis, which is to investigate the performance of Automatic Repeat Request (ARQ) and Hybrid Automatic Repeat Request (HARQ) techniques in inter-High Altitude Platform (HAP) Free-Space Optical (FSO) links. Furthermore, the chapter explores the research questions that the thesis aims to address and provides an outline of the thesis.

Chapter 2: This chapter explores the channel model for inter-High Altitude Platform (HAP) Free-Space Optical (FSO) communication in turbulent atmospheric conditions. It discusses the impact of atmospheric effects on the FSO link, including optical turbulence profiles, the effects of aperture averaging, and static pointing errors. The model for the Receiver Front End (RFE) and the link budget are also presented. Furthermore, the chapter explores the modeling of the scintillation index in a regime of low fluctuations. It offers a thorough explanation of reciprocity in FSO channels and introduces assessment measures for reciprocity.

Chapter 3: This chapter offers a comprehensive review of error control techniques, including a focused discussion on Forward Error Correction (FEC) methods, particularly Reed-Solomon (RS)

FEC. It also outlines Automatic Repeat Request (ARQ) schemes and their performance measures. In conclusion, the chapter identifies the most suitable ARQ scheme for this thesis through a quantitative comparison.

Chapter 4: This chapter introduces a novel approach to modify the Forward Error Correction (FEC) code-rate in accordance with the specific CSI type. This method consists of choosing the ideal code-rate based on the CSI type and fine-tuning it for the Receiver Front End (RFE) to enhance transmission efficiency for each CSI type. It recommends the use of an adaptive code-rate selection look-up table and suggests incorporating this strategy into the Selective Repeat (SR) Automatic Repeat Request (ARQ) mechanism.

Chapter 5: This chapter outlines the two simulation environments utilized in this thesis. The first one, based on Matlab, is used for the inter-High Altitude Platform (HAP) Free-Space Optical (FSO) channel to generate the received power vectors. The second environment, running on OMNET++, serves to simulate Automatic Repeat Request (ARQ) and Hybrid Automatic Repeat Request (HARQ) schemes.

Chapter 6: This chapter presents the outcomes of the performance evaluation. Initially, it introduces and assesses the results of reciprocity measurements from a long-distance bidirectional free-space optical (FSO) communication system, which features a ground-to-ground reciprocal FSO link distance of 62.86 km - the longest ever recorded. In addition, the chapter offers a simulation-based performance analysis of Hybrid Automatic Repeat Request (HARQ) in inter-High Altitude Platform (HAP) FSO links, exploring a broad array of channels and parameters. It further scrutinizes the effectiveness of adaptive code rate HARQ, both with and without different forms of channel state information (CSI).

Chapter 7: This chapter summarizes the research findings, contributions, and conclusions presented in the thesis. It also discusses the limitations of the work and provides recommendations for future research directions.

2 | Inter-HAP FSO Channel Model

This chapter presents the channel model for inter-High Altitude Platform (inter-HAP) Free-Space Optical (FSO) links under conditions of atmospheric turbulence. It examines the effects of such turbulence on the channel in Section 2.2. This section sheds light on stratospheric conditions and presents pertinent optical turbulence models in Section Section 2.4. The model is then adapted for HAP-to-HAP communication scenarios using well-established analytical models. The scenarios employed in this study are explored in Section 2.3. Additionally, the impact of pointing errors on the channel is investigated in Section 2.8. The channel model's suitability for various scenarios, as described in Section 2.3, is assessed, alongside crucial link budget calculations. With a focus on HAP-HAP communication systems, Section 2.9 provides an in-depth discussion of the receiver and link budget, and presents an overview of channel parameters. A detailed explanation of FSO channel reciprocity is provided in Section 2.10. The chapter wraps up with a summary of the key points in Section 2.11.

2.1. Introduction

In this section, we will explore the significance of accurate modeling of the communication channel between two high-altitude platforms (HAPs) using free-space optical (FSO) links. The optimal configuration of a communication system's transmitter and receiver is largely influenced by the communication channel. For inter-HAP communication, atmospheric turbulence affects the channel, leading to scintillations or random variations in the intensity of the laser beam carrying the signal [4]. These variations, compounded with beam spreading and wander, can cause signal losses and fading, thereby increasing the system's bit error ratios. To accurately gauge the performance of an inter-HAP communication system, it's crucial to start with an appropriate model of optical turbulence.

Turbulent atmospheric motion, influenced by moisture and temperature gradients, causes disturbances in the atmosphere's refractive index in the form of optical turbulence cells, known as *optical turbules* [4, 2]. According to [4], optical turbulence arises from fluctuations in the refractive index due to small temperature variations. The random redistribution of the refractive index in space and time leads to several effects on an optical wave, including temporal irradiance fluctuations (scintillation) and phase fluctuations. The index of refraction structure constant C_n^2 serves to characterize these fluctuations. To categorize different turbulence regimes, it's necessary to determine the height profiles of C_n^2.

While numerous standard profiles exist, most are tailored to specific objectives, geographical locations, and climate conditions, and may not be suitable for new areas. To fully understand and characterize FSO communication between two HAPs, the channel must be accurately modeled, taking into account various factors. This involves modeling the optical turbulence, the effects of pointing error, the reciprocity of the FSO channel, and defining the necessary link budget calculations. By characterizing the communication channel using various parameters, optimal channel performance can be effectively achieved.

The main effects on the inter-HAP FSO link, relevant to this thesis, are elaborated in the subsequent sections of this chapter:

- **Atmospheric Turbulence Effects:** As the optical signal travels through layers of turbulence with different refractive indices, the wavefront becomes distorted. This distortion causes constructive and destructive interference within the beam itself, resulting in variations in optical intensity, or scintillations, at the HAP receiver.

- **Pointing Error:** This refers to the total displacement between the center of the laser beam and the center of the receiver aperture, known as Pointing Error. It comprises two components: constant misalignment and random pointing error.

- **Channel Reciprocity:** This term refers to the correlation of received powers at both ends of the inter-HAP FSO bidirectional link. This phenomenon arises when laser beams traverse the same refractive index inhomogeneities and atmospheric turbulence.

2.2. The Stratosphere

Several atmospheric elements, including rain, snow, fog, haze, and pollution, adversely affect electromagnetic radiation as it travels through the atmosphere [42]. These elements contribute to the absorption, scattering, and refraction of the optical wave, leading to the wave's attenuation. The propagated optical wave undergoes irradiance fluctuations, beam spreading, and a loss of spatial coherence due to refraction effects. The turbulence effect stems from small-scale dynamical changes in the atmospheric index of refraction, forming temporary pockets of air with slightly varied temperature and density, known as turbulence cells. Consequently, these cells develop different refraction indices, which leads to beam wandering-the random shifting of the instantaneous beam center-if the turbulence cells are larger than the beam diameter. Conversely, if the turbulence cells are smaller than the beam diameter, ray bending and diffraction will distort the laser beam's wave front. Changes in the arrival time of the laser beam at the receiver lead to both constructive and destructive interference, causing fluctuations in beam intensity, also known as scintillations.

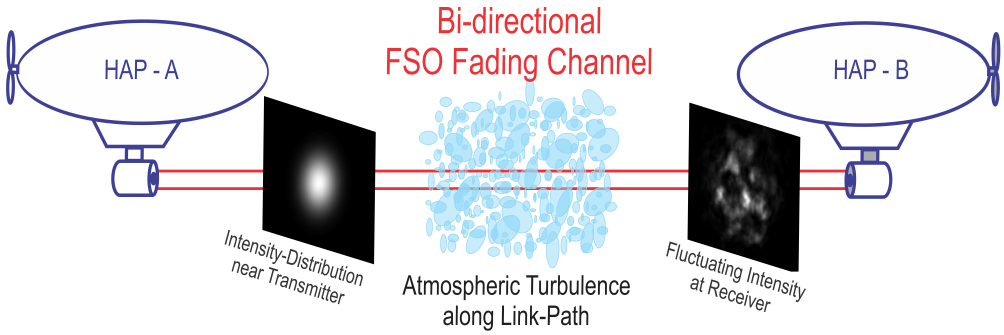

Figure 2.1.: A schematic of the stratospheric inter-HAP FSO bi-directional link.

To gain a deeper understanding of the effects of atmospheric turbulence on the free-space optical (FSO) channel, a bi-directional FSO inter-HAP communication between HAPs A and B is showcased in Figure 2.1. The diagram demonstrates how atmospheric turbulence influences the propagation path and the subsequent intensity fluctuations at the receiver. Atmospheric factors such as absorption, scattering, and refraction diminish the performance of the FSO link, causing signal fading and impairing the communication system's performance. Thus, it's crucial to characterize the FSO channel using models that account for these atmospheric factors. By modeling the channel using various parameters, we can optimize the performance of the communication channel effectively.

This thesis primarily concerns the stratosphere, a layer of the Earth's atmosphere, as it focuses on communication between platforms at this altitude. The stratosphere lies between the troposphere and the mesosphere and is characterized by its relative dryness, minimal water vapor content, and temperature that rises with altitude. Clouds are rare in this layer, except for Polar Stratospheric Clouds (PSCs) that can form in the lower stratosphere near the poles when temperatures fall below -78°C. The altitude of the stratosphere varies depending on location. The stratosphere starts at around 18 km near the equator, but at mid-latitudes, it begins between 10 and 13 km. It extends up to 50 km in altitude. At the poles, the stratosphere's lower boundary is about 8 km, compared to

roughly 18 km at the equator. Due to the lack of vertical convection in the stratosphere, substances can linger there for considerable periods. The air in the stratosphere is about a thousand times less dense than at sea level, making it an optimal altitude for jet aircraft and weather balloons. The temperature in the stratosphere increases with altitude, resulting in diminished turbulence and updraft, or air movement perpendicular to the ground. The stratosphere's unique characteristics significantly influence the communication capabilities of platforms operating within it. Therefore, understanding these properties is vital for this thesis, which investigates communication between stratospheric platforms and the potential impact on communication systems

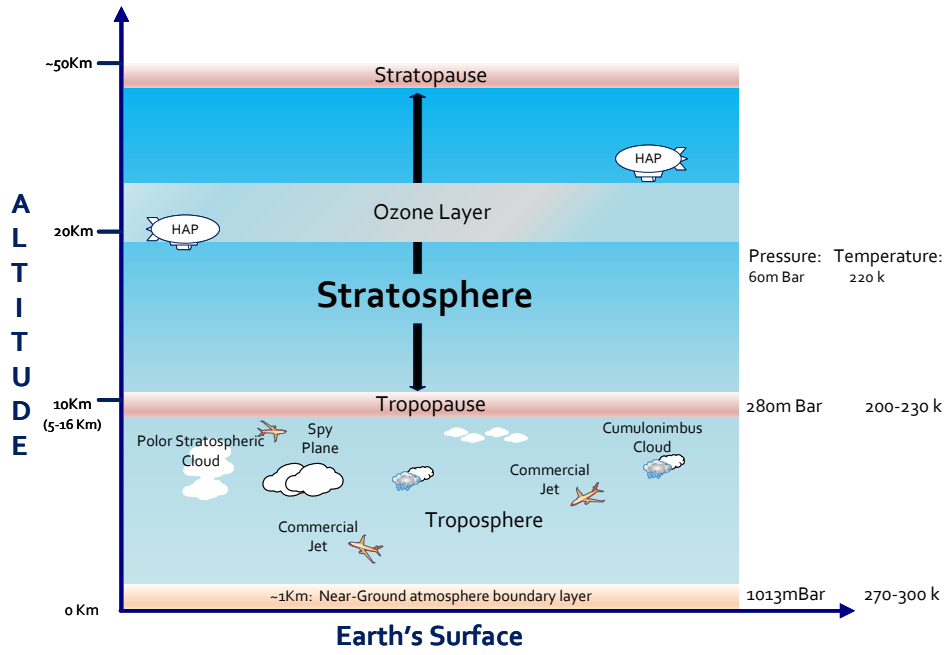

Figure 2.2.: Characteristics of the Earth's atmosphere and the stratosphere.

Figure 2.2 highlights the characteristics of the Earth's atmosphere, particularly the stratosphere. High-altitude platforms (HAPs) are positioned well above cloud level, ensuring that changing weather conditions do not interfere with communication links. However, the minimum graze height for any inter-HAP link must consider local climatic conditions like tropopause height. As referenced in [5], a graze height of 13 km is deemed an acceptable limit for mid-latitude inter-HAP links.

Atmospheric wind speed varies based on season, geographic location, and temperature gradient. The highest wind speeds are found at approximately 12 km, 70 km, and 100 km altitudes. However, between altitudes of 20 km and 90 km, air masses remain relatively stable and predictable, with very slow winds. According to [13], most stationary stratospheric platforms are positioned at a height of around 20 km. Figure 4 in [13] indicates that the optimal altitude range for these platforms is between 19 and 25 kilometers, with slightly higher wind speeds observed between 17 and 19 km. Above 25 km altitude, wind speeds typically increase up to 70 km, then decrease from 70 km to 90 km.

2.3. Inter-HAP Scenarios

This section presents an overview of the inter-HAP scenarios and their respective geometries examined in this thesis. The goal of this research was to investigate the impact of various atmospheric and geometric parameters by analyzing scenarios with different HAP heights and link distances. A typical inter-HAP bidirectional link geometry is depicted in Figure 2.3, featuring two link distances (L) of 150 km and 900 km, each associated with specific HAP heights (H_{hap}) and a graze height (G_h). The cloud ceiling sets the graze height (G_h), representing the lowest height of the optical link above the Earth's surface. In all scenarios, we stipulate a graze height (G_h) of 18 km, where the highest level of turbulence is observed [5].

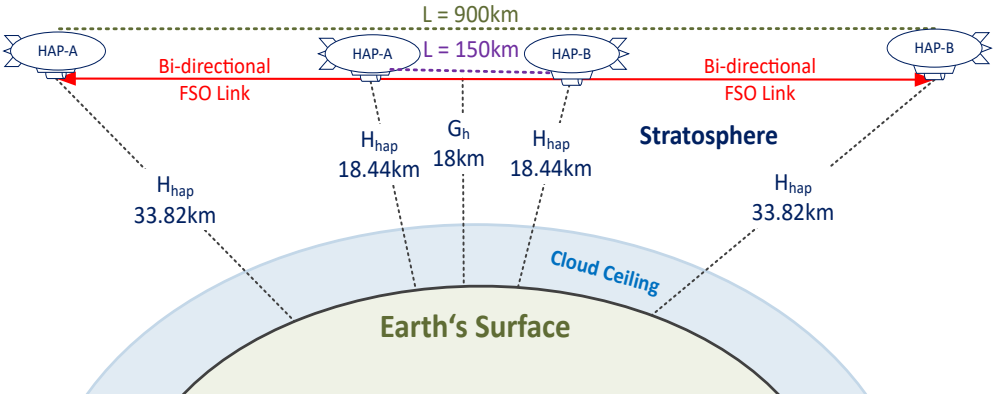

Figure 2.3.: Illustration of the bi-directional inter-HAP FSO link geometry at the stratosphere (distances not to scale).

In Table 2.1, we detail various bidirectional inter-HAP scenarios, considering eight link distances for HAPs situated at H_{hap}. We maintain a single graze height (G_h) across all scenarios. The term t_{TOF} denotes the time-of-flight (ToF) or propagation delay for the various link distances. These scenarios were selected for further scrutiny. We set the graze height at 18 km, the elevation of maximum turbulence above the Earth's surface, and adjusted the HAP heights to achieve different link distances. By varying the inter-HAP link distance, we could study the influence of the atmosphere and reciprocity on FSO links. Additionally, the scenarios were chosen to accommodate different potential times of flight, allowing us to examine the delay effects of the CSIs on HARQ performances. The speed of the channel in the proposed scenarios was also varied according to different stratospheric wind speeds (v), which impacts the channel's correlation time (τ_0), thereby influencing the performance of the HARQ schemes discussed in Chapter 6.

Link Distance L **(km)**	**Time of Flight** t_{TOF} **(ms)**	**Graze Height**[a] G_h **(km)**	**HAP Height** H_{hap} **(km)**
150	0.5	18	18.44
200	0.66		18.78
300	1		19.76
450	1.33		21.96
600	2		25.09
700	2.33		25.57
800	2.66		30.51
900	3		33.82

Table 2.1.: Overview of inter-HAP scenarios.

Note: [a] Graze height (G_h) is the minimum height of the optical link above the Earth's surface, where turbulence is at its maximum.

2.4. Optical Turbulence Profile

An optical turbulence profile provides insights into how turbulence in the Earth's atmosphere affects optical signal propagation, which is crucial for atmospheric optics and free-space optical (FSO) communication [43, 4]. It typically includes the variation of the refractive index structure constant (C_n^2) with altitude. This profile helps us understand how atmospheric turbulence changes with altitude, leading to phenomena like scintillation and beam wander. These changes can significantly impact the quality of optical communication links over large distances. The design and optimization of FSO systems heavily rely on these turbulence profiles, as they illuminate how turbulence changes with altitude and influences signal quality and transmission under various atmospheric conditions.

The refractive-index structure parameter C_n^2, expressed in $m^{-2/3}$ units, is widely used to quantify atmospheric turbulence by indicating the degree of refractive-index fluctuations [4, 2, 44]. Variations in C_n^2 along the propagation path are significant, prompting numerous researchers to predict its behavior. Although several models exist, they are often based on site-specific experimental data, limiting their broader applicability. Models for calculating C_n^2 can be empirical, theoretical, analytical, or numerical, each requiring different input parameters. As noted in [#2005_Andrews], C_n^2 can be treated as "constant" along a horizontal path but varies along a slant path due to changing temperature gradients, air pressure, and density at different altitudes. The intensity of these fluctuations relates to the temperature structure function, as discussed in [43, 4]:

$$C_n^2 = \left(79 \cdot 10^{-6} \frac{P}{T^2}\right)^2 C_T^2 \qquad [m^{-2/3}] \tag{2.1}$$

C_T^2 temperature structure parameter ($deg^2/m^{2/3}$)
P atmospheric pressure ($bars$)
T temperature ($kelvin$)

The refractive index structure parameter C_T^2 is determined by measuring the mean square temperature between two points at a specific distance along the propagation path, as outlined in [43, 4]. Eq. (2.1) illustrates that the refractive index structure parameter can be calculated by measuring the pressure, temperature, and spatial temperature fluctuations along the optical link's propagation path.

2.4.1. Hufnagel-Valley (H-V) Model

The altitude profile for this parameter, C_n^2, is determined using the Hufnagel-Valley (H-V) model as described in [4]:

$$C_n^2(h) = 0.00594 \cdot (\frac{w}{27})^2 (10^{-5}h)^{10} exp(\frac{-h}{1000}) + 2.7 \cdot 10^{-16} exp(-\frac{h}{1500}) + A exp(-\frac{h}{100}) \quad [m^{-2/3}] \tag{2.2}$$

h altitude of the link (m)
w RMS wind speed from 5 km to 20 km altitude (m/s)
A value of C_n^2 at $h = 0$ ($m^{-2/3}$)

For our calculations, we employ the H-V model with $w = 21 m/s$ and $A = 1.7 \cdot 10^{-14} m^{-2/3}$, a configuration often referred to as the $HV_{5/7}$ model [4].

It's crucial to distinguish between RMS wind speed and link orthogonal wind speed (v). The orthogonal wind speed solely considers the wind component that is perpendicular to the optical path. However, the RMS wind speed takes into account wind variations throughout the entire optical path, offering a more all-encompassing perspective on wind-induced turbulence and its influence on FSO link performance. Represented by w and stated in meters per second, RMS (Root Mean Square) wind speed is provided as per [4]:

$$w = \left[\frac{1}{15 \cdot 10^3} \int_{5 \cdot 10^3}^{20 \cdot 10^3} V_B^2(h) dh\right]^{1/2} \qquad [m/s] \tag{2.3}$$

where $V_B(h)$ is derived from the Bufton wind model as referenced in [4, 45], specified as follows:

$$V_B(h) = w_s h + v_g + 30exp\left[-\frac{h-9400}{4800}\right] \qquad [m/s] \tag{2.4}$$

v_g ground wind speed (m/s)

h altitude (m)

w_s slew rate of the optical beam (m/s) (angular velocity of the laser beam derived from the HAP moving speed)

The refractive-index structure parameter C_n^2-profiles are depicted in Figure 2.4, which are calculated using Eq. (2.2). The C_n^2-profiles displayed in Figure 2.4 (a) for various inter-HAP link distances L along the propagation path z of the FSO link. These correspond to the scenarios described in Table 2.1. The peak value of C_n^2 is found in the middle of the inter-HAP link path, and the mean value of the C_n^2-profile increases with link distance. These C_n^2-profiles in Figure 2.4 (b) and Figure 2.4 (c) illustrate the intensity of refractive index fluctuations in the altitude range of interest, between 16 and 22 km. The profiles are derived based on RMS wind speeds of $w = 10m/s$ (representing the best case of C_n^2) and$w = 30m/s$ (representing the worst case of C_n^2), with the tropopause at 13 km and the maximum stratosphere altitude at 26 km. The figures highlight a significant discrepancy between the best and worst case C_n^2 profiles. The C_n^2-profile along the inter-HAP link distance L is illustrated in Figure 2.4 (c). It indicates that at a graze height of 13 km, the highest turbulence is noticed at the link's center.

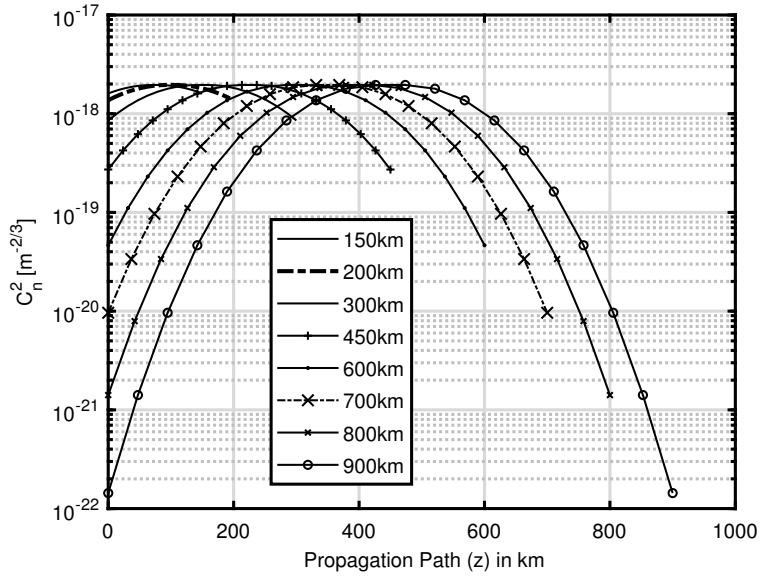

(a) C_n^2-profile along the propagation path (z) for varying link distances (L).

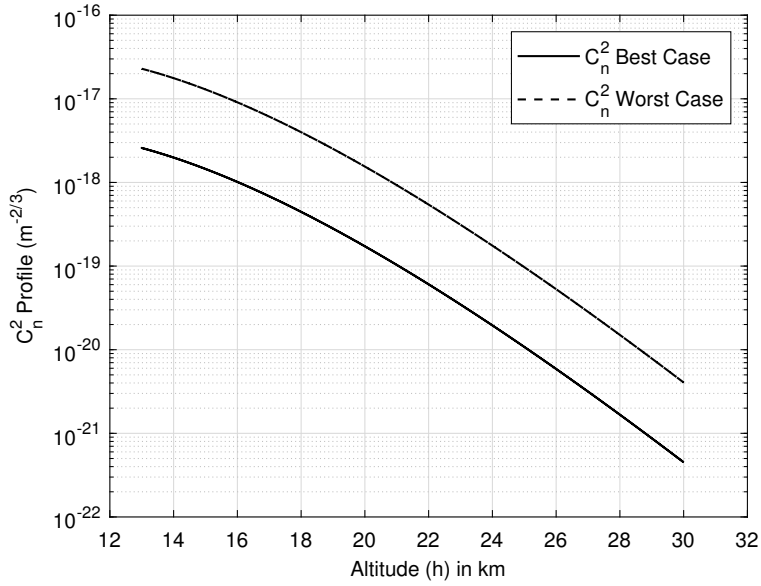

(b) C_n^2-profile across varying altitudes (h).

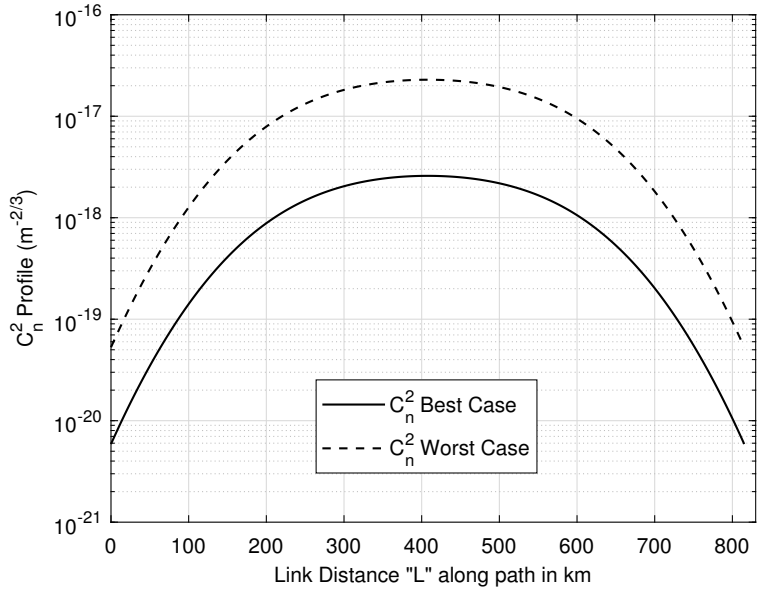

(c) C_n^2-profile for the link distance (L) between HAPs, with a minimum graze height of 13 km.

Figure 2.4.: Analyzing turbulence strength (C_n^2) through the H-V Model.

Note: In the Best and Worst-case scenarios for C_n^2, the RMS wind speed (w) is $10m/s$ and $30m/s$ respectively.

2.4.2. Walters and Kunkel Model

The first step in evaluating the effect of turbulence on FSO links involves calculating the C_n^2-profile based on altitude. The Hufnagel-Valley (HV) model [4], which scales the atmospheric IRT structure function, is the most prevalent method for this computation. However, this model falls short in validating reciprocity measurements in near-ground horizontal paths that range from a few meters to approximately 250 meters above ground level. In a bidirectional turbulent channel, channel reciprocity suggests that received powers at the transmitter and receiver ends are somewhat correlated [46, 47, 40].

To validate channel reciprocity for bidirectional horizontal links and extend its applicability to inter-HAP FSO links, we conducted an experiment on a 62.86 km turbulent FSO bi-directional link. The experiment is elaborated in Section 6.1. For our numerical simulations, we employ the Walters and Kunkel model [48], which is described as follows:

$$C_n^2(h) = C_n^2(h_0)(\frac{h_0}{h_L})^p,\ h_L > h_0, \qquad [m^{-2/3}] \tag{2.5}$$

h_0	reference height above ground (m)
h_L	height profile above ground (m)
$C_n^2(h_0)$	reference refractive index structure value at h_0 ($m^{-2/3}$)
p	power law parameter varies from $4/3$ during the daytime
	to $2/3$ for measurements between sunset and sunrise (unitless)

2.5. Modeling Scintillation Index: Weak Fluctutation Regime

In this chapter, we explore the scintillation index, a crucial factor in determining the performance of our laser HAP communication systems. The expressions developed here are limited to weak irradiance fluctuation regimes, for which the Rytov method is applicable. In such cases, the scintillation index is directly linked to the log-amplitude variance. According to [43, 4], traditional approaches to optical wave propagation primarily rely on uniform plane wave and spherical wave models. However, these simple wave models neglect various effects attributable to the finite size of a beam wave, along with its diverging and focusing capabilities. We employ the lowest-order Gaussian-beam wave as our basic wave model, typical of a single transverse electromagnetic wave (TEM_{00}) originating from a laser. By establishing theory for a beam wave, we can easily derive classical results related to infinite plane wave and spherical wave models. As per [4], the spherical wave model is utilized for a small-aperture source or a source with a large divergence angle. For inter-HAP FSO links, we use the spherical wave model approximation to determine the scintillation index. To account for the effects of static pointing error, we align the wave with the Gaussian

wave model. Since we only consider a static pointing error (σ_{rms}) on top of atmospheric fading impacts, we do not model the scintillation approximation for a Gaussian beam.

Scintillation, or variations in irradiance or intensity, occurs when an optical wave travels through the atmosphere, even on short propagation paths. Almost entirely, atmospheric temperature variations of a small magnitude produce oscillations in the index of refraction, or optical turbulence, which is the cause of scintillation. The Scintillation Index (SI), also known as the normalized variance of irradiance fluctuations, is the central focus of both theoretical and experimental investigations in the study of irradiance fluctuations given by [43, 4]:

$$\sigma_I^2 = \frac{\langle I^2 \rangle - \langle I \rangle^2}{\langle I \rangle^2} \qquad [unitless] \tag{2.6}$$

I irradiance (intensity) of the optical wave
$\langle\rangle$ ensemble average (sample mean)

The *Rytov variance* can be used to quantify the severity of intensity scintillation caused by atmospheric turbulence. In the case of weak fluctuations, it represents the normalized irradiance variance, or scintillation index, of an unbounded plane wave. When extended to strong fluctuation regimes by increasing either C_n^2 or the propagation distance L, or both [43], it is considered a measure of optical turbulence strength.

SI is proportional to the plane wave Rytov variance σ_R^2 in the weak turbulence condition, and it is defined for a constant C_n^2-profile as shown in [4]

$$\sigma_I^2 \simeq \sigma_R^2 = 1.23 C_n^2 k^{\frac{7}{6}} L^{\frac{11}{6}} \qquad [unitless] \tag{2.7}$$

C_n^2 refractive index structure constant ($m^{-2/3}$)
k optical wave number (m^{-1})
L propagation path length (m)

The turbulence strength shall be classified as *weak*, *moderate* or *strong*. According to [4] weak fluctuations are associated with $\sigma_R^2 < 1$, moderate fluctuations with $\sigma_R^2 \sim 1$ and strong fluctuations with $\sigma_R^2 > 1$ and the so called saturation regime is defined when $\sigma_R^2 \to \infty$.

Scintillations occur mainly due to small-scale inhomogeneities, roughly equivalent to the dimensions of the Fresnel zone[1]. The inner scale effects are insignificant when the inner scale is significantly smaller than the Fresnel zone's size. However, when the inner scale (smallest eddies or

[1] Fresnel zone named for physicist Augustin-Jean Fresnel. It is one of a (theoretically infinite) number of concentric ellipsoids that defines volumes in the radiation pattern of a (usually) circular aperture [49].

turbulent structures that occur within the boundary layer of the atmosphere) and the Fresnel zone are of similar size, an increase in scintillations is observed, as seen in the refractive-index spectrum. Weak irradiance scintillations are generally not sensitive to large-scale inhomogeneities, except near the beam edge. Outer scale effects (refers to the characteristic length scale associated with the largest turbulent structures or eddies within a turbulent flow) tend to decrease scintillations off the beam axis, but have negligible impact on unbounded plane waves, spherical waves, or the optical axis of a Gaussian-beam wave [4]. The scale size which is most effective to produce scintillation is influenced by the turbulence strength. According to [4] for zero inner scale and outer scale effects FSO irradiance is mainly affected by three cell sizes termed: spatial coherence radius ρ_0, Fresnel zone size $\sqrt{L/k}$ and the scattering disk $L/k\rho_0$. In weak scintillations [4], the correlation width of irradiance fluctuations is dictated by the Fresnel zone, while in strong fluctuation regimes, it is defined by the spatial coherence radius ρ_0. Under weak irradiance fluctuations ($\sigma_R^2 << 1$), the scintillation index of an optical wave navigating through atmospheric turbulence is primarily determined by scale sizes equivalent to the first Fresnel zone, where L is the propagation path length, and k is the optical wave number.

The plane wave Rytov variance commonly denoted as σ_R^2 is a parameter which defines the areas of fluctuation regimes in the atmosphere. For a variable C_n^2-profile, the Rytov variance for a plane wave is defined as [4]:

$$\sigma_R^2 = 2.25k^{7/6}\int_0^L C_n^2(z)(L-z)^{5/6}dz \qquad [unitless] \tag{2.8}$$

$k = \frac{2\pi}{\lambda}$	optical wave number (m^{-1})
λ	wavelength (m)
L	link distance (m)
z	propagation path (m)

The *Intensity Scintillation Index (ISI)* σ_I^2 is the normalized variance of irradiance fluctuations. For inter-HAP links, this thesis employs the spherical wave approximation. When the receiver is in the center of a diverging Gaussian beam and has a small diameter in comparison to the beam diameter, spherical wave equations are appropriate. The ISI σ_I^2 is defined as [43, 4]:

$$\sigma_I^2 = exp\left[\frac{0.49\beta_0^2}{(1+0.56\beta_0^{12/5})^{7/6}} + \frac{0.51\beta_0^2}{(1+0.69\beta_0^{12/5})^{5/6}}\right] - 1, \quad 0 \leq \beta_0^2 < \infty \qquad [unitless] \tag{2.9}$$

$\beta_0^2 = 0.4\sigma_R^2$ spherical wave Rytov variance
σ_R^2 plane wave Rytov variance

The plot in Figure 2.5 depicts the relationship between the predicted intensity scintillation index Eq. (2.9) and the Rytov variance for zero inner scale effects for spherical waves. As shown in Figure 2.5, the ISI for spherical waves increases with increasing Rytov variance until it reaches a maximum value greater than one. Following this peak, the ISI decreases with increasing Rytov variance until it reaches one. The saturation region is defined as in [43, 4]. Furthermore, the spherical wave's peak scintillation occurs near $\sigma_R = 4$. In the regime of weak fluctuation, the SI initially increases with increasing sigma σ_R^2. The weak fluctuation conditions correspond to regimes with a scintillation index σ_I^2 less than one throughout the beam profile, which is the focus of this Inter-HAP channel model.

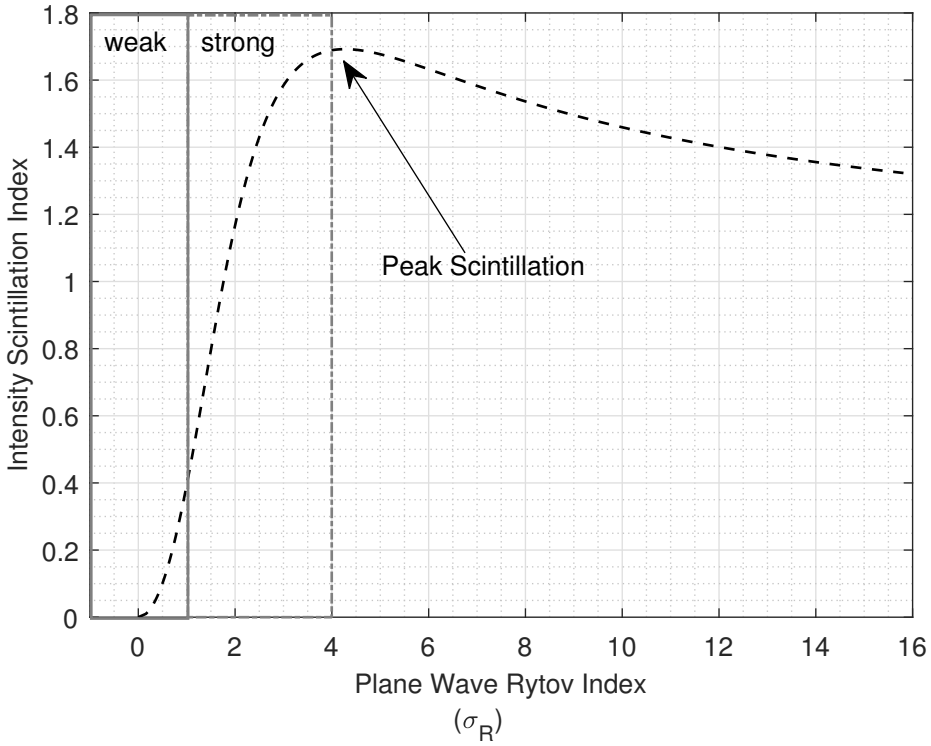

Figure 2.5.: Visualization of the intensity scintillation index for the spherical wave model, excluding inner-scale effects.

The Figure 2.6 shows the increase in Rytov variance along the beam or link profile as link distance or C_n^2-profile increases for the best and worst cases (for RMS wind speeds: w=10 m/s (C_n^2 Best case) and w=30 m/s (C_n^2 Worst case)) assuming a HAP altitude of 22 km.

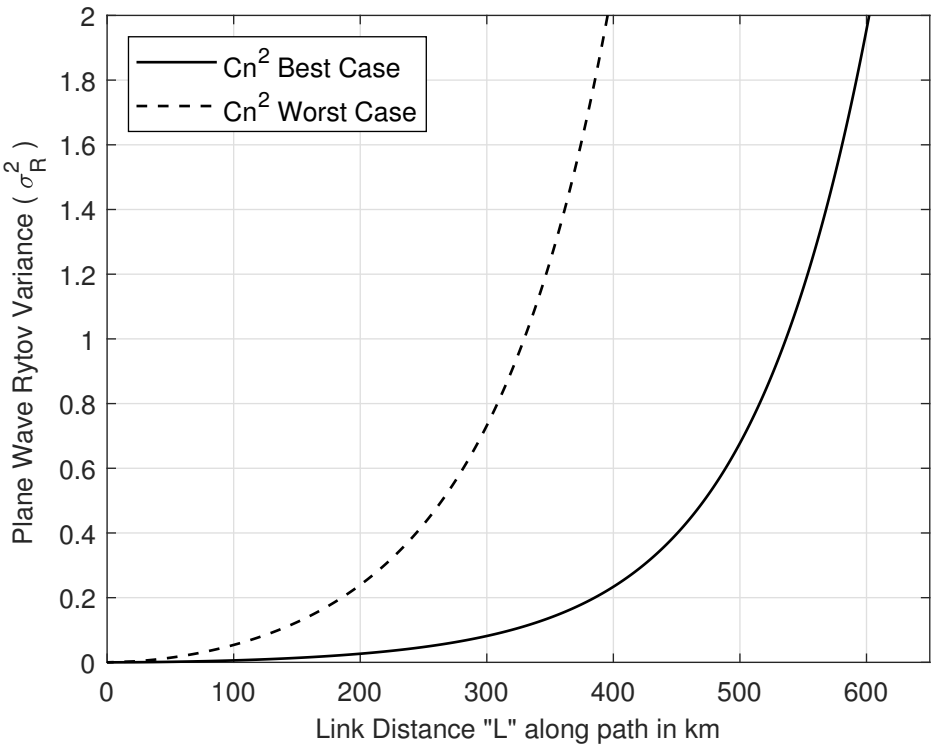

Figure 2.6.: Variation of Rytov variance along the inter-HAP link path.

Note: Comparison of C_n^2 in Best Case and Worst Case scenarios with RMS wind speeds of 10 m/s and 30 m/s respectively. The depicted Rytov variance corresponds to an H_{hap} of 22 km.

Turbulence-induced scintillation, a consequence of beam propagation through the atmosphere, can significantly impair the performance of an Inter-HAP FSO communication system. More specifically, scintillation can cause power reductions at the receiver, potentially causing the received signal to fade below a detectable level. As the laser beam moves through the atmosphere, it will undergo intensity changes due to turbulence-induced variations in the Index of Refraction (IRT), a phenomenon known as scintillations.

In this thesis, the *Power Scintillation Index (PSI)* is characterized as the normalized variance of the optical power fluctuations (P) observed in the receiver plane, specifically within the diameter (D_{rx}) of a circular aperture. The optical power is defined as the intensity integrated over the aperture area. This means that the total power is calculated by summing up the intensity (power per unit area) across the entire area of the aperture[4]. The spherical wave Rytov variance is denoted as $\beta_0^2 = 0.4\sigma_R^2$, where$\sigma_R^2$ stands for the plane wave Rytov variance. The PSI, as given by [43, 4], represents the normalized variance of the received power P into a specified receiver aperture diameter (D_{rx}):

$$\sigma_P^2(D_{rx}) = \frac{\langle P^2 \rangle - \langle P \rangle^2}{\langle P \rangle^2} \qquad [unitless] \tag{2.10}$$

P received optical power (W)
D_{rx} receiver aperture diameter (m)
$\langle . \rangle$ time averaging

2.6. Lognormal Distribution: Inter-HAP Fading Channel

Atmospheric turbulence is a natural phenomenon that arises from the fluctuations in the refractive index caused by variations in temperature and pressure in the atmosphere. As a result, the atmospheric turbulence channel is highly unpredictable and subject to weather effects, causing fluctuations in the phase and intensity of the received signal due to refractive index variations along the propagation path. This randomness in the received signal can lead to significant error rates in free-space optical (FSO) links [4, 42, 3]. Various studies have been conducted to examine the effects of atmospheric turbulence on the error rates of FSO links, resulting in the development of statistical models that describe the fluctuations in both weak and strong fading regimes. The two most widely used models are the lognormal (LN) and gamma-gamma distributions. The lognormal model is appropriate for weak-to-moderate intensity fluctuations, while the gamma-gamma model is more suitable for strong turbulent conditions.

In the weak fluctuation regime, the irradiance statistics of an optical wave are assumed to be governed by a lognormal probability density function (PDF) [50, 4]. The lognormal distribution with a PDF is expressed using the power scintillation index σ_P^2, and the mean power P_0 is given by [51, 50, 52]:

$$p(P,\sigma_P^2) = \frac{1}{P\sqrt{2\pi ln(\sigma_P^2+1)}} e^{-\frac{\left(ln\frac{P}{P_0}+\frac{1}{2}ln\left(\sigma_P^2+1\right)\right)^2}{2ln\left(\sigma_P^2+1\right)}} \qquad [unitless] \tag{2.11}$$

P_0 mean optical power (W)
σ_P^2 power scintillation index (unitless)

Figure 2.7 depicts the resulting PDF for PSIs of 0.1, 0.5, and 2 calculated using Eq. (2.11). The distribution is clearly skewed to the right, but the exact shape depends on the scintillation strength σ_P^2. When the scintillation index is high, the PDF rises sharply from zero to the maximum value but is highly skewed in comparison to lower scintillation indices.

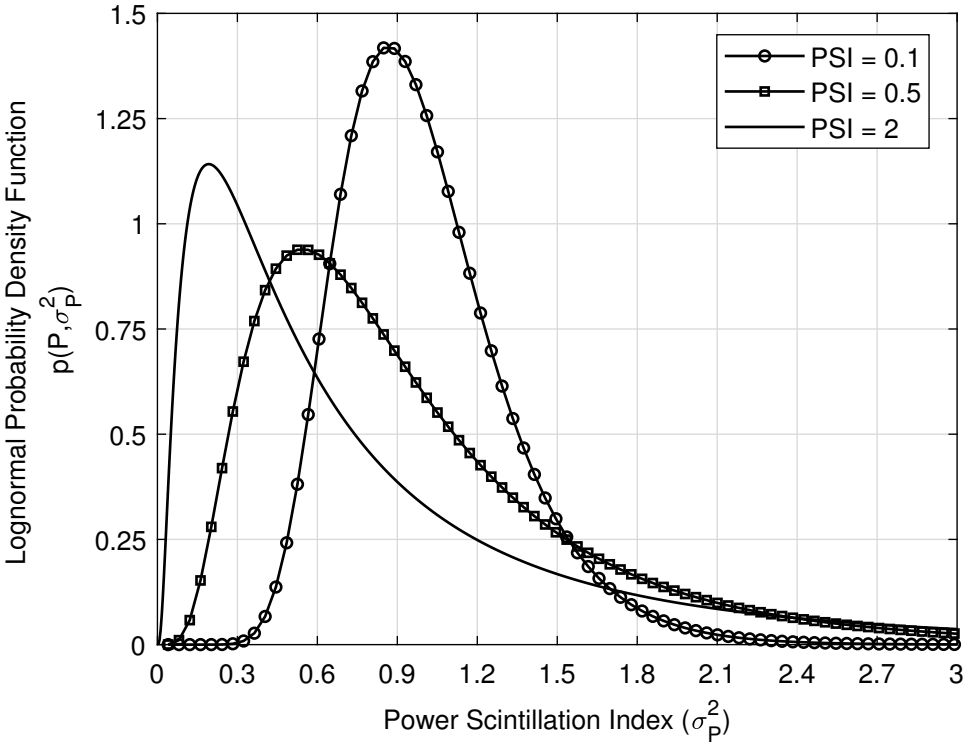

Figure 2.7.: Characterization of the PDFs comparison for the lognormal distribution calculated using Eq. (2.11).

2.7. Aperture Averaging

To mitigate the effects of scintillations on optical link performance, it's beneficial to have a large detection plane area to accumulate as much light as possible. The irradiance model introduced in Section 2.5 is predicated on spherical waves travelling through horizontal paths and irradiance fluctuations gathered by small or point apertures. In the scenario of a large receiving aperture, the irradiance fluctuations get averaged over the aperture area, thereby reducing scintillation compared to that measured by a point receiver [53, 4]. This phenomenon is referred to as the aperture averaging effect [54, 55, 4].

A sufficiently large aperture smooths out the small-scale fluctuations. Notably, under weak scintillation conditions, aperture-averaged irradiance fluctuations are well-matched by the lognormal PDF model (as discussed in Section 2.6) for all aperture sizes. For an aperture size greater than or equal to the intensity coherence width (denotes the spatial range within which fluctuations in intensity remain correlated or coherent) ρ_i, the irradiance distribution appears to conform to a lognormal distribution [56, 57, 51]. The aperture averaging factor A_{AF} is mathematically expressed as defined by [4]:

$$A_{AF} = \frac{\sigma_I^2(D_{rx})}{\sigma_I^2(0)} = \frac{\sigma_P^2}{\sigma_I^2} \qquad [unitless] \tag{2.12}$$

$\sigma_I^2(0)$	scintillation index of a point receiver (unitless)
$\sigma_I^2(D_{rx})$	power scintillation index (unitless)
D_{rx}	receiver aperture diameter (m)

A_{AF} can have values in the range of 0 to 1, with lower values denoting greater aperture averaging. A_{AF} is used to reduce the variance of intensity fluctuations at the receiver. The lowest possible value of A_{AF} is expected, in order to average out signal fluctuations due to atmospheric turbulence. The aperture averaging factor for a spherical beam is given by [58]:

$$A_{AF} = \left[1 + 0.333\left(\frac{kD_{rx}^2}{4L}\right)^{5/6}\right]^{-7/5} \qquad [unitless] \tag{2.13}$$

$k = \frac{2\pi}{\lambda}$	wave number (m^{-1})
λ	wavelength (m)
D_{rx}	receiver aperture diameter (m)
L	link distance (m)

The intensity coherence width ρ_i, obtained from the irradiance covariance function, marks the maximum size of the receiver aperture that functions like a point receiver. Apertures larger than ρ_i will experience a form of aperture averaging, which essentially reduces the scintillation observed by the receiver photodetector [4]. In the context of our inter-HAP FSO links, the receiver apertures are designed to be smaller than the intensity coherence width (ρ_i). This results not only in increased scintillations but also in a higher reciprocity effect. Therefore, maintaining a receiver aperture size smaller than ρ_i is crucial for preserving enhanced reciprocity. This aperture averaging effect is only relevant to the reciprocity measurements outlined in Section 6.1 within this thesis and is not pertinent to the inter-HAP scenarios.

2.8. Pointing Error in Inter-HAP Links

Pointing is a critical component of High-Altitude Platforms (HAPs) communication systems because it directs the transmission laser to the receiver based on prior knowledge of their positions. To accomplish this, rough estimates of the HAPs' positions are calculated while they are orbiting in the stratosphere. The finite speed of light and the relative velocity of the two HAP terminals, on the other hand, cause pointing errors that must be compensated for. This is accomplished by directing the transmit beam to the location where the receiver terminal will be after propagation time. The overall displacement between the center of the laser beam and the center of the receiver aperture is referred to as *Pointing Error* [10]. It is made up of two parts: constant misalignment and random pointing error. Turbulence-induced beam wander, optical misalignment, mechanical vibrations, and relative movement of the transmitter and receiver can all cause pointing errors. When

there is no or imperfect slow tracking, the pointing error is the combined effect of turbulence-induced beam wander and the relative mechanical displacement of the transmitter and receiver. Slow tracking eliminates the relative movement of the transmitter and receiver, leaving only the turbulence-induced beam wander as the pointing error. Fast tracking reduces the overall displacement caused by beam wander. The remaining fast-tracking error is then referred to as pointing error.

The pointing error is a laser beam offset angular deviation from the line of sight (LOS) direction between transmitter and receiver. The zenith angle is defined as the angle formed by the zenith direction and the laser beam's direction towards the HAP terminal. Figure 2.8 depicts the pointing error, with the zenith angle, ζ representing the angle between the zenith direction and the laser beam direction towards the HAP terminal. The pointing error is measured and the pointing accuracy is determined based on the acceptable level of error to evaluate the quality of pointing. The acceptable level of error varies according to the system specifications and requirements is generally lower for higher data rate systems. As a result, minimizing pointing errors is critical for accurate communication between HAPs and their receivers.

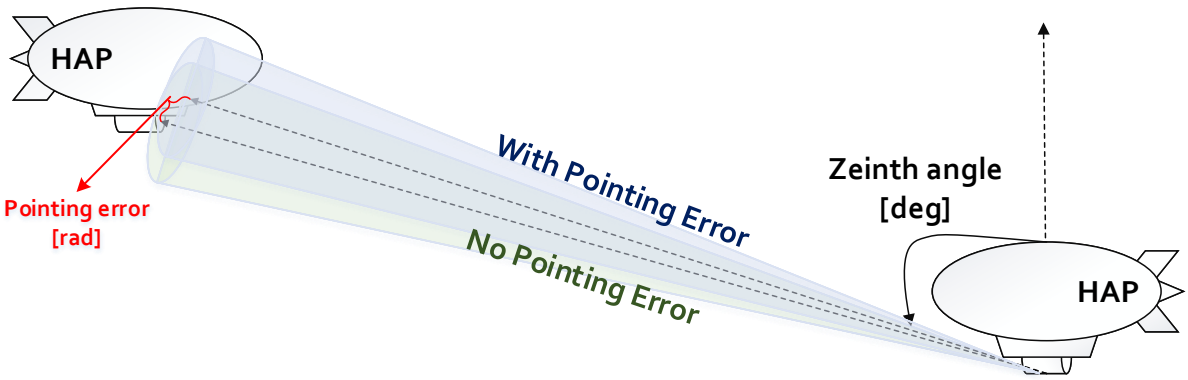

Figure 2.8.: Illustration of the inter-HAP communication scenario, depicting the zenith angle and angular pointing error with line-of-sight (LOS).

According to [4], atmospheric turbulence can cause a loss of direct line of sight, known as *Beam Wander*. The receiver aperture, represented by a solid cycle in Figure 2.9, has its center at (0,0), whereas the average beam spot of the received random beams, represented by a dashed cycle, has its center at (x,y). The optical beam's pointing error can be caused by residual fast-tracking, turbulence-induced beam wander, or the combined effects of beam wander and transceiver-induced extra pointing error. In this thesis, while modeling pointing errors in inter-HAP channels, we only consider static pointing errors caused by miss-pointing (transceiver-induced extra pointing error) and assume there are no losses due to beam wander.

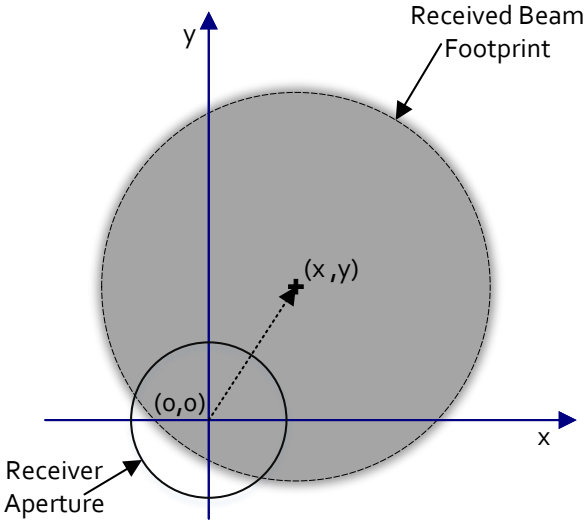

Figure 2.9.: Visualization of the beam center exhibiting random movement.

Several studies [59, 60, 61, 62, 23] proposed procedures to derive the statistical distribution of pointing errors. Random angular jitter caused by optical platform mount vibrations is a source of random variations in optical power at the receiver [63, 12]. Random angular jitter in this context refers to the uncertainty in the optical axis's direction with respect to the desired line of sight, resulting in a residual Root Mean Square (RMS) pointing error. To achieve optimal performance in FSO systems, the tracking and pointing capability must be accurate enough to match the divergence angle of the transmitted laser beam. In practice, however, FSO terminals operate with random angular pointing jitter. To achieve the best average Packet Error Probability (PEP) performance, a trade-off between the divergence angle and a reasonable pointing error must be found [60]. A greater divergence angle reduces pointing error losses while increasing intensity losses. Smaller divergence angles, on the other hand, result in larger pointing errors, increasing losses due to pointing error.

Based on [64], we consider a losses due to a static pointing error of $\sigma_{rms} = 20\mu rad$ Eq. (2.16). For small divergence angles, the pointing error is large. However, larger divergence angles result in losses due to reduced irradiance at the receiver. We consider, an optimal value of a full $1/e^2$ divergence angle of $85\mu rad$. It's important to note that this value heavily depends on factors such as the desired mean bit error probability, receiver characteristics, and other fluctuations in received power caused by atmospheric disturbances [10, 64, 4].

The probability density function (PDF) of the received optical intensity can be represented by the beta distribution, which is expressed as [10, 59, 61]:

$$p(I) = \beta I^{\beta-1} \; for \; 0 \leq I \leq 1, \tag{2.14}$$

$$\bar{I} = \frac{\beta}{\beta + 1} \tag{2.15}$$

I normalized intensity
$\bar{I}$ average intensity

The relationship between the β parameter and the variance of pointing error and beam divergence is expressed as:

$$\beta = \frac{w_0^2}{4\sigma_{rms}^2} \tag{2.16}$$

w_0 full $1/e^2$ divergence angle (rad)
σ_{rms}^2 pointing error variance (unitless)

2.8.1. Bit Error Probability

According to [4], the fading behavior of an optical channel is determined by atmospheric turbulence-induced scintillation and pointing errors at the receiver [65]. This indicates that the interaction of scintillation effects and pointing errors results in signal fluctuations such as fades and surges. These variations occur on timescales longer than the propagation delays between high-altitude platforms (HAP). Surge is defined as when the instantaneous received power exceeds the average received power, whereas fade is defined as when the instantaneous received power falls below the average received power.

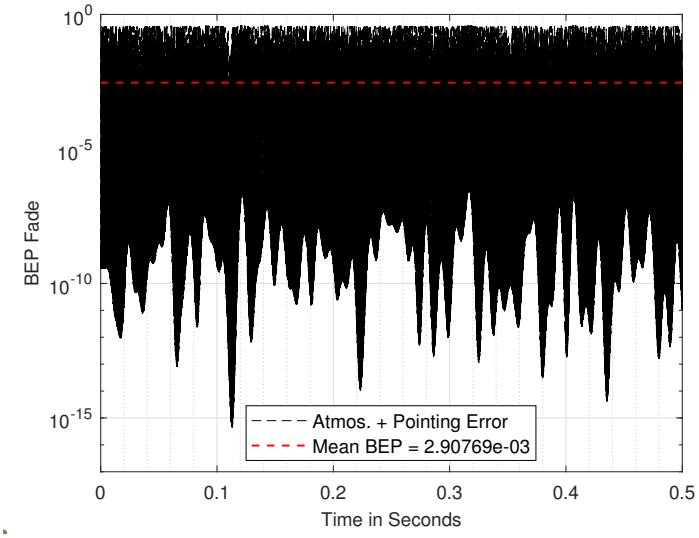

(a) L- 400 km, Wind speed - 10 m/s, ISI - 0.008, Pointing error ($\sigma_{rms} = 20\mu rad$).

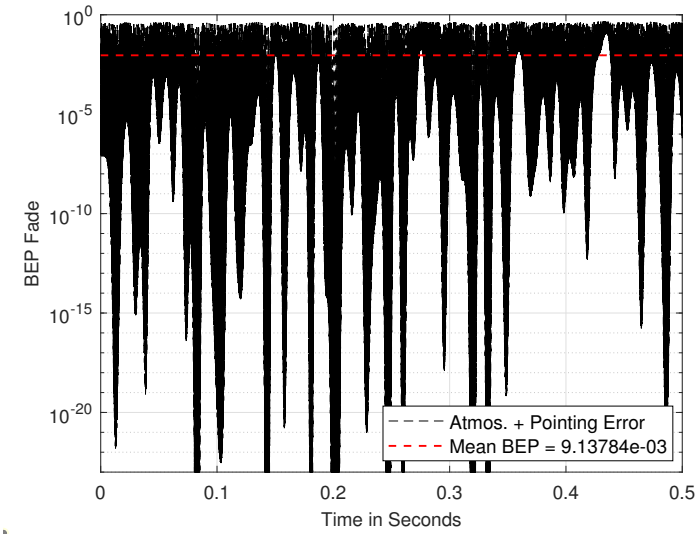

(b) L- 400 km, Wind speed - 30 m/s, ISI - 0.65, Pointing error ($\sigma_{rms} = 20\mu rad$).

Figure 2.10.: Visualization of the fading behavior of bit error probability, illustrating the impacts of atmospheric and pointing errors generated using PvGeT simulation as detailed in 5.1.2.1.

Pointing error can result in deep fades at the receiver, which causes a significant loss of signal availability as depicted in Figure 2.10 (a) and Figure 2.10 (b). In this thesis, we investigate the combined effects of pointing error- and atmospheric turbulence-induced fading. Over time, these occurrences cause the bit error probabilities (BEP) to have a fluctuating distribution. In the context of our communication channel, fading effects contribute to unevenly distributed bit errors across transmitted data, and the amount of BEP varies depending on the channel's state at any given time.

2.9. Inter-HAP Communication System

An inter-HAP optical communication system enables data transmission between two High Altitude Platforms (HAPs). The selection of a receiver with characteristics suitable for the communication channel is critical for maximizing performance. Bit Error Probability (BEP) and power margin are two key metrics used for quantitatively assessing performance. Link budget calculations help estimate possible power margin at a targeted BEP, considering potential losses at the transmitter, within the channel, and at the receiver. This discussion will concentrate on contributors to optimal performance: the receiver, channel parameters, and link margin. The receiver is a vital part of the communication process. It needs to be carefully chosen, considering its sensitivity, noise attributes, and dynamic range. Channel parameters, such as turbulence-induced fading, influence the received signal power and should be factored into link budget calculations. Additionally, channel losses can arise from atmospheric absorption, scattering, and beam spreading. The link margin, defined as the excess of available power over the minimum power required, ensures the reliability of the communication system. A positive link margin signifies the communication system's ability to withstand unexpected channel losses or changes without performance impairment. A range of elements, including transmit power, receiver sensitivity, channel losses, and the modulation scheme, must be considered to secure an adequate link margin. Therefore, the inter-HAP optical communication system's optimal performance can be reached by aptly selecting the receiver, accounting for channel losses in link budget computations, and maintaining a sufficient link margin.

2.9.1. Receiver Front-End (RFE)

The performance of an optical receiver is significantly influenced by its sensitivity, which refers to the minimum input power required to attain a specified Bit Error Probability (BEP) [66, 67, 68, 52]. In typical wireless optical channels, light-emitting diodes and photodiodes serve as transmitters and detectors, respectively. These devices only modulate and detect the intensity of the carrier, not its phase, ensuring that all transmitted signal intensities. Moreover, safety regulations cap the average optical power emitted, thereby constraining signal amplitude. Factors like distortion during signal propagation and the limited response times of optoelectronics also restrict the channel bandwidth. As traditional signal space models and coded modulation techniques designed for electrical channels do not consider signal amplitude constraints, they are not directly applicable to this type of channel. Furthermore, traditional transmission methods like optical fibers, optimized for broadband optical channels, are often inefficient in terms of bandwidth in this setting. As a result, innovative approaches and techniques are necessary to optimize the performance of optical receivers in wireless optical channels.

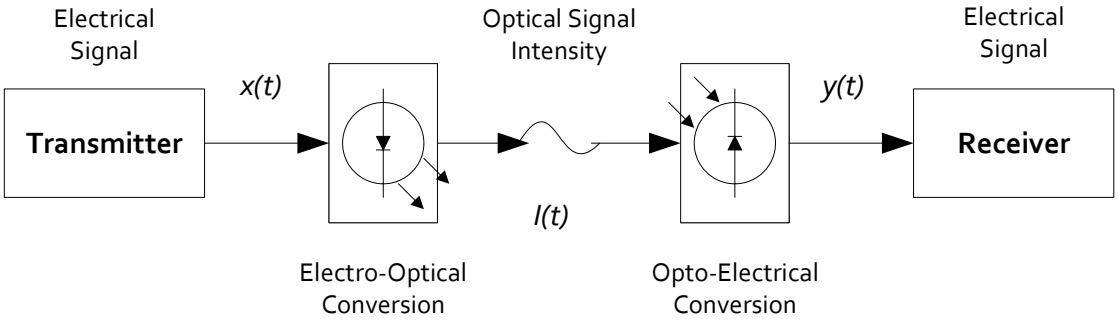

Figure 2.11.: Simplified block diagram illustrating the configuration of an optical intensity direct detection communications system.

In Direct Detection (DD) receivers, a photodiode is employed as a square-law device, producing an electrical signal proportional to the power of the incident signal as depicted in Figure 2.11. This allows the power of the optical signal to be directly measured [67]. The performance of the optical wireless link is largely dictated by the receiver's performance, given constraints such as limited transmitted power, safety requirements, and noisy environments. The optical wireless receiver comprises a photodiode, a preamplifier, and additional signal processing circuits. Applications demanding high sensitivity and broad bandwidth often employ a design with a small aperture or area. This thesis will focus on an intensity modulation and direct detection (IM/DD) system [68] when modeling the inter-High Altitude Platform (HAP) communication channel.

2.9.2. Bit Error Probability (BEP)

In digital communication systems, reliability is expressed as the Bit Error Probability (BEP), also known as the Bit Error Ratio (BER) which is the number of bit errors per unit time. The BEP is a unitless performance measure calculated by dividing the number of bit errors by the total number of transferred bits over a given time interval. It is measured at the receiver's output and is affected by the received signal level and receiver noise level. A lower BEP indicates that the communication system is more reliable. We concentrate on a Receiver Front End (RFE) that receives optical signal power and converts an optically On-Off Keying (OOK) modulated signal to an electrical signal current via direct detection with internal gain Avalanche Photo Detector (APD).

Based on [68, 52], the RFE model used in this study is a typical APD with a shot noise limited slope, Non-Return-to-Zero (NRZ) modulation, an equal probability of zeros and ones, and a sensitivity $\overline{P}_{Q=2}$. The relationship between P_{rx}, the BEP-function, and the Q-factor can be used to describe the binary RFE characteristics that is expressed as:

$$BEP = 0.5 \cdot erfc\left(\frac{Q(\overline{P}_{rx})}{\sqrt{2}}\right) \tag{2.17}$$

$erfc$	complementary error function
$\overline{P}_{rx}$	mean received power (W)
$Q-factor$	qualitative factor of the receiver performance (unitless)

The mean received power can be used to express the **Q-factor** and the **OSNR (Optical Signal-to-noise ratio)** as pure functions given by [66, 68]:

$$Q(\overline{P}_{rx}) = 2\left(\frac{\overline{P}_{rx}}{\overline{P}_{Q=2}}\right)^{n} \tag{2.18}$$

$$OSNR = (Q(\overline{P}_{rx}))^2 = \left[2\left(\frac{\overline{P}_{rx}}{\overline{P}_{Q=2}}\right)^{n}\right]^2 \tag{2.19}$$

$\overline{P}_{Q=2} = 27.75\,nW$	receiver sensitivity to achieve a $\overline{BEP} = 0.023$ [68]
$\overline{BEP}$	mean Bit Error Probability (unitless)
$n = 0.5$	sensitivity slope operating data rate of $R = 1.25\,Gbps$

The sensitivity slope n in a receiver front end represents the rate at which the receiver's sensitivity adjusts in response to changes in input signal power. It measures how effectively the receiver detects weak signals and converts them into usable electrical signals, in optical or wireless communication systems [66].

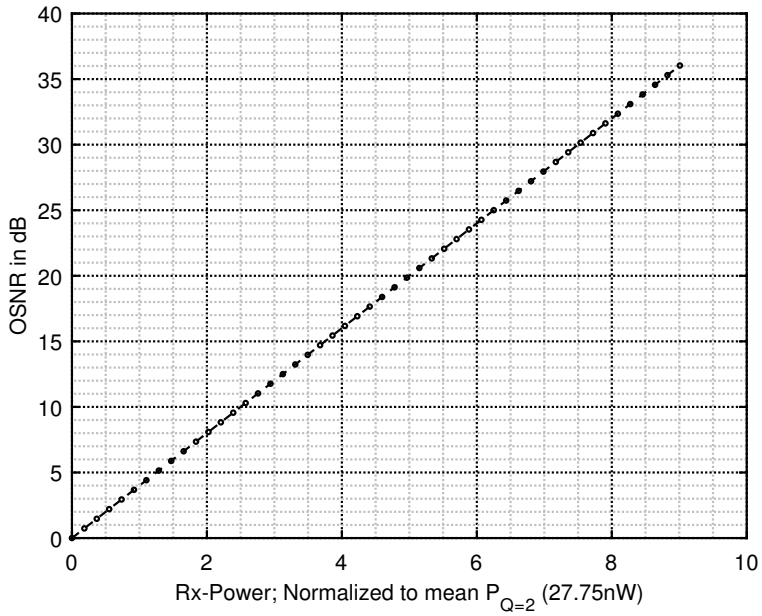

(a) OSNR calculated using Eq. (2.19).

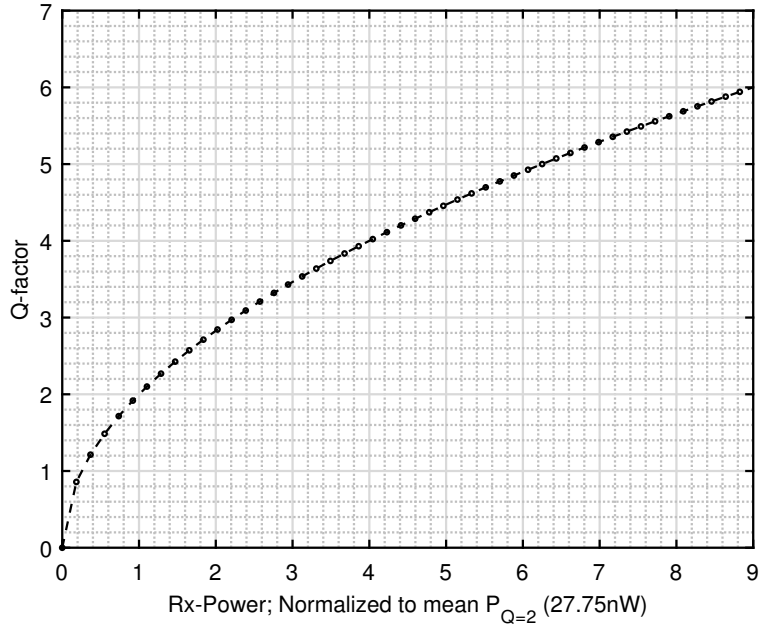

(c) Q-factor calculated using Eq. (2.18)

Figure 2.12.: RFE characterization: A focus on OSNR and Q-factor.

The performance of an optical receiver is commonly assessed through the sensitivity parameter, which signifies the minimum input power needed to reach a specific bit error ratio (typically 10^{-9} in optical communication systems). The values of $\overline{P}_{Q=2}$ (required mean received power for Q=2)) and n are selected and optimized for various types of receiver front ends (RFEs) at a data rate of $1.25Gbps$, as demonstrated in TABLE III of [68]. The characterization of the RFE employed in this study is depicted in Figure 2.12. The signal quality is evaluated using the signal Q-factor, which aids in determining the BEP, as shown in Figure 2.13.

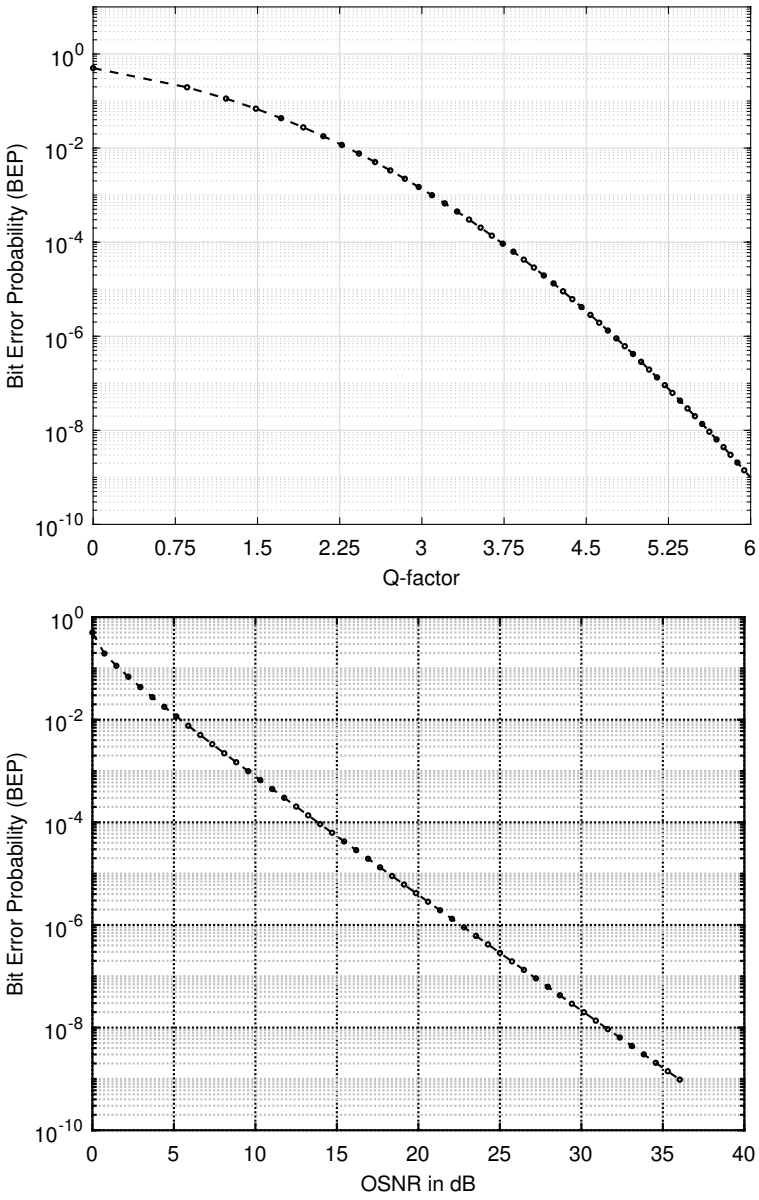

(a) BEP calculated using Eq. (2.17) along the Q-factor.

(b) BEP calculated using Eq. (2.17) along the OSNR.

Figure 2.13.: RFE characterization based on Bit Error Probability (BEP).

2.9.3. Link Budget and Channel Parameters

The link budget, which compares the transmitted power to the required optical power at the receiver while accounting for all power losses in the system, is used to evaluate the performance of an optical communication system. The residual power at the receiver dictates the achievable data transmission rate. Factors such as the modulation format, allowable bit error probability, and various noise sources also influence this power level. Residual power refers to the remaining signal strength at the receiver after transmission losses. This power level impacts the maximum data rate the system can handle, as higher residual power generally supports faster transmission. The modulation format (which defines how data is encoded onto the signal), the bit error probability (tolerable error rate in data), and noise (interference that affects signal clarity) all contribute to how effectively the residual power can be utilized for data transmission.

The link budget for the HAP-to-HAP scenario was calculated in this study to determine link performance at a net data rate of 1.25 Gbps. For four different inter-HAP link distances, link budget calculations were performed, and the mean transmit power was varied to achieve a link margin of 0 dB. Table 2.2 displays the results. Atmospheric losses in the link budget Table 2.2 refers to the signal attenuation caused by atmospheric conditions, such as absorption, scattering, and turbulence, as the signal travels. This loss reduces the signal strength at the receiver, impacting overall link performance.

Parameters	**Symbol (Unit)**	**Value**			
Mean Transmit Power	P_{tx} (mWatt)	44.5	119	205	329
Link Distance	L(Km)	220	339	426	516
Data Rate	R (Gbps)	1.25			
Wavelength	λ (nm)	1550			
Transmitter Divergence, FWHM	θ_{tx} (μrad)	85			
Rx- Aperture Diameter	D_{rx} (m)	0.15			
Atmos. Losses	a_{atmos}(dB)	0.96	1.47	1.85	2.24
Receiver sensitivity for $BER = 1E-9$	S_{rx}(nW)	200			
Link Margin	L_m (dB)	0			

Table 2.2.: Overview of the static link budget for an inter-HAP link scenario (no scintillation loss regarded).

A complete list of channel parameters used in this thesis with reference to this Chapter 2 is presented in Table 2.3.

Channel Parameters	**Unit**	**Description**
H_{hap}	m	HAP height - altitude at which HAPs are placed
G_h	m	Graze height- minimum height of the optical link above the surface of the earth (maximum turbulence regime)
L	m	Inter-HAP link distance
$\sigma_P^2(D_{rx})$ or PSI	unitless	Power scintillation index for a given receiver aperture diameter D_{rx}
D_{rx}	m	receiver aperture diameter
C_n^2	$m^{-2/3}$	Refractive index structure constant
w	m/s	RMS wind speed parameter used in C_n^2-profile
σ_R^2	unitless	Rytov variance
σ_I^2	unitless	Intensity Scintillation Index
v	m/s	Orthogonal wind speed (shall not be confused with RMS wind speed)
τ (or) $HWHMacov$	s	Correlation time of the channel (normalized autocovariance at the Half Width Half Maximum (HWHM))
RTT	s	Round-trip time
t_{TOF}	s	Propagation delay for different link distances/ time-of-flight
ρ	unitless	$\frac{RTT}{\tau}$; ratio of round trip time over correlation time of the channel

Table 2.3.: Comprehensive list of parameters for the inter-HAP FSO channel.

2.10. FSO Channel Reciprocity

Channel reciprocity in a free-space optical (FSO) bidirectional link refers to the correlation between received powers at both link ends [46]. This phenomenon arises as laser beams traverse identical refractive index inhomogeneities and atmospheric turbulence. The potential advantages of this effect for error control in FSO communication systems have been thoroughly investigated through experiments and simulations [47, 69, 70]. In smaller transceivers, the principle of optical reciprocity creates a strong correlation between the power signals at both terminals. This correlation is especially evident in symmetric monostatic link geometry, where the transmitting and receiving beams have the same optical axis and aperture size. Power reciprocity can be achieved

with reasonably sized receiver apertures because the principle of axial intensity reciprocity extends to spatial diameters smaller than the intensity speckle patterns [71, 72, 73].

The Figure 2.14 illustrates an example of strongly correlated power vectors received over a link distance of 900 km. The simulation used a receiver aperture diameter of 20 cm and Power Scintillation Index (PSI) values of 0.981 and 1.126 at terminals A and B respectively. The vectors, with Half Width at Half Maximum (HWHM) autocorrelation values of 2.95 ms at acov-A and 2.91 ms at acov-B, exhibit strong correlation, indicated by a Correlation Coefficient (CCF) of 0.924. Additionally, a lower Normalized Mean Square Error (NMSE) value of 0.18 is observed, further supporting the high degree of correlation.

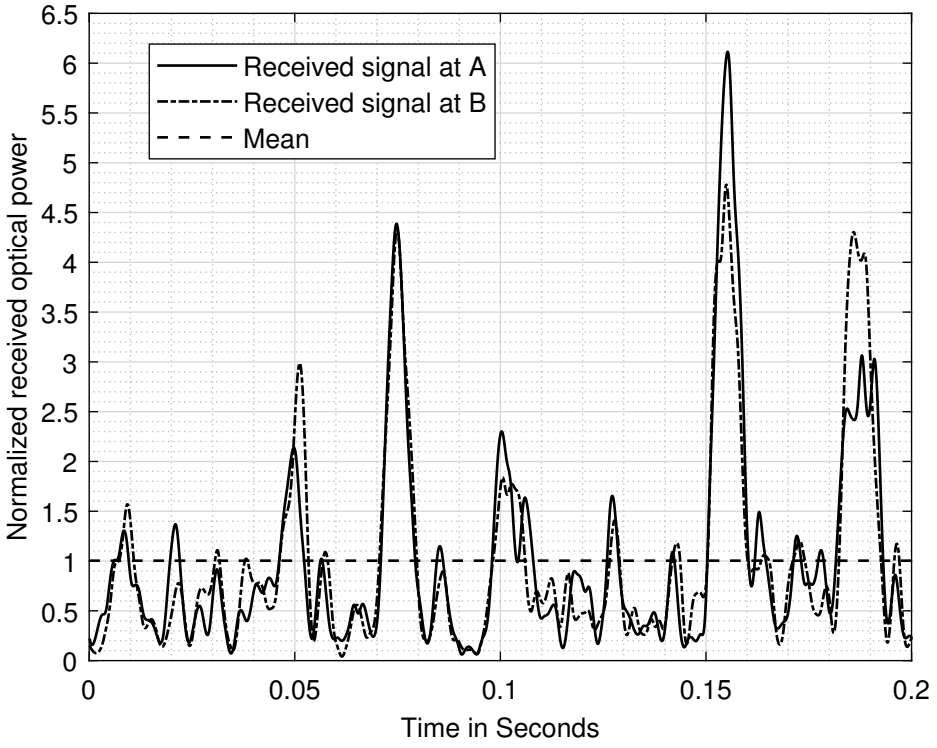

Figure 2.14.: Simulated normalized received power vectors illustrating the strong reciprocity correlation between receivers A and B.

Note: The received power vectors are generated through simulations using PILab, which is thoroughly explained in Section 5.1.1.2.

In this thesis, we have investigated the principle of channel reciprocity in two primary ways. Initially, we conducted reciprocity measurements using a long-distance bidirectional Free-Space Optical (FSO) communication system. This system featured a reciprocal FSO link with a ground-to-ground distance of 62.86*km* - the longest ever recorded, as elaborately covered in Section 6.1. Subsequently, we extrapolated this concept to inter-HAP platforms, using it as reciprocal Channel State Information (CSI) to enhance the performance of HARQ schemes, as discussed in Section 6.3.

2.10.1. Measures of Reciprocity

The measurable parameters that evaluate the symmetry and consistency of bidirectional free-space optical communication are referred to as measures of FSO channel reciprocity. They aid in determining whether reciprocity is present by comparing the transmitted and received signals in both directions of FSO links. Strong correlations between these measures suggest that FSO channels are symmetric and reciprocal in both transmission directions.

CCF (Correlation Coefficient) is an estimate of the correlation between two random sequences or as the deterministic correlation between two deterministic signals. It is defined as follows [74] :

$$CCF = \frac{\sum\{(A_i - \mu_A)(B_i - \mu_B)\}}{\sigma_A \sigma_B} \qquad [unitless] \tag{2.20}$$

$\sum$	Summation over i, where i equals 1 to N
A_i	received optical power over time measured at terminal A
B_i	received optical power over time measured at terminal B
μ_A	mean of received optical power at terminal A
μ_B	mean of received optical power at terminal B
σ_A	standard deviation of received optical power at terminal A
σ_B	standard deviation of received optical power at terminal B

In general, NMSE (Normalized Mean Squared Error) provides an estimate of the overall deviations between predicted and measured values. It is defined as [75]:

$$NMSE = \frac{\sum(A_i - B_i)^2}{\mu_A \mu_B} \qquad [unitless] \tag{2.21}$$

$\sum$	Summation over i, where i equals 1 to N
A_i	received optical power over time measured at terminal A
B_i	received optical power over time measured at terminal B
μ_A	mean of received optical power at terminal A
μ_B	mean of received optical power at terminal B

In this thesis, we utilize parameters such as the Power Scintillation Index (PSI), as outlined in Section 2.5, along with the Correlation Coefficient (CCF), Normalized Mean Squared Error (NMSE), and Half Width Half Maximum autocovariance (HWHM acov.) to evaluate the reciprocity quality

in our measurement and numerical simulation outcomes. HWHM autocovariance is the time interval between the peak of the autocorrelation function and the point where its value falls to half of the maximum. It measures the signal's coherence and pulse width, indicating how quickly the correlation diminishes. A narrower HWHM signifies a sharper, more localized signal peak, while a broader HWHM indicates a more dispersed correlation. A combined consideration of CCF and NMSE serves to assess the quality of reciprocity, since NMSE focuses solely on absolute power fluctuations. Imperfections in the channel state information are suggested by CCF values less than one or NMSE values exceeding zero.

The CCF gauges the quality of power reciprocity by analyzing the received power vectors at both link ends [47, 76]. Inter-HAP links typically feature speckle patches several decimeters in size, allowing for sufficiently large receiver apertures to support high-speed links while keeping the CCF near one [72, 47, 76]. Capitalizing on the effect of channel reciprocity in FSO communication systems offers substantial benefits for error control. By utilizing the correlated information from received power, it's now feasible to enhance error correction mechanisms, thereby improving the overall reliability of FSO links. This concept has stimulated interest in research and development endeavors aimed at enhancing FSO system performance through the application of reciprocity principles.

2.11. Chapter Summary

The channel model, with a focus on inter-HAP FSO links, has been comprehensively presented in this chapter. Details have been provided for the selected scenarios for this thesis. The effects of the atmosphere, in conjunction with the combined effect of static pointing error, have been presented for this link. The scintillation index has been modelled for a weak fluctuation regime, and the channel has been modelled as a lognormal fading channel. The RFE model, employed for the links, has been detailed, and the link budgeting with channel parameters has been presented. Lastly, the principle of channel reciprocity and the measures used to quantify it have been discussed. The error correcting methods for inter-HAP links utilized in this thesis are presented in the following Chapter 3.

3 | Error Control Methods

This chapter aims to provide a comprehensive overview of various error control methods. Section 3.1 introduces the existing error control methods broadly. Section 3.2 presents a detailed exploration of Forward Error Correction (FEC) techniques, specifically focusing on the Reed-Solomon (RS) FEC, along with the rationale for its selection in this thesis. Further, Section 3.3 delivers an in-depth analysis of Automatic Repeat reQuest (ARQ) schemes, a significant part of the error correction protocol, elucidating their basic principles, various types, and performance metrics in detail. Section 3.5 identifies the optimal ARQ scheme for this thesis. Lastly, Section 3.6 provides a summary of the chapter.

3.1. Introduction

In line with [27], Figure 3.1 presents a typical digital communication structure and its constituents, excluding elements such as encryption/decryption, symbol-timing recovery, and scrambling. Encryption is a choice, while symbol-timing recovery and scrambling are ideally included and factored into probabilistic channel models, as detailed in [77] study on channel coding. The information source and sink could be either analog or digital, with the end user being a human, a computer, or any electronic device. The source encoder compresses the information source bit sequence into a more efficient sequence with fewer bits, while the source decoder retrieves the original sequence. The channel encoder safeguards transmitted bits from disruptions like noise, distortion, and interference by altering its input into a redundant sequence. When the received data is affected by noise, distortion, or interference, the channel decoder retrieves the original input to the channel encoder, which is the compressed sequence, from the sequence of the channel output. The modulator modifies the channel encoder output bit stream to match the communication channel's format, while the demodulator recovers the modulator input sequence from the modulator output sequence. The communication channel is the physical medium used for transmitting or storing the modulator's output. This channel may include antennas, amplifiers, and filters at both the transmitter and receiver ends. However, it typically introduces noise and interference from other signals. The channel depicted is the free-space optical inter-HAP channel as defined in Chapter 2.

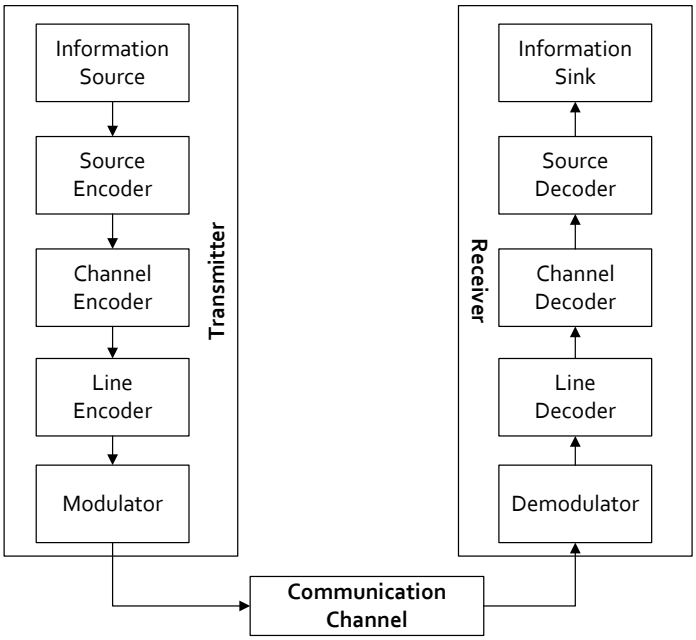

Figure 3.1.: A general overview of digital communication framework.

Figure 3.2 provides a summary of various types of coding. Coding can be divided into four distinct categories [28, 78, 79, 80].

Cryptographic coding facilitates secure communication, *line coding* enhances spectral characteristics for digital data transportation, and *source coding* is primarily used for data compression.

Channel coding, also known as *Error Control Coding (ECC)*, employs error correction codes to enable robust and reliable data transmission. In this thesis, our primary focus is on one of these four coding types - *channel/error control coding*. In general, when data is stored or transmitted, encoding becomes a necessity. The branch of mathematics that investigates the transmission of a digital bit stream over a noisy channel is known as *Coding Theory* [28, 81]. As shown in Figure 3.2, ECC is bifurcated into error detection and error correction [79]. Error detection's function is to identify errors caused by noise or other channel disruptions. In digital communications, this is most frequently implemented using Cyclic Redundancy Check (CRC) [79]. Other kinds of error detection schemes include repetition codes, parity check codes, checksum, and Arithmetic Redundancy Check (ARC) codes [79, 80].

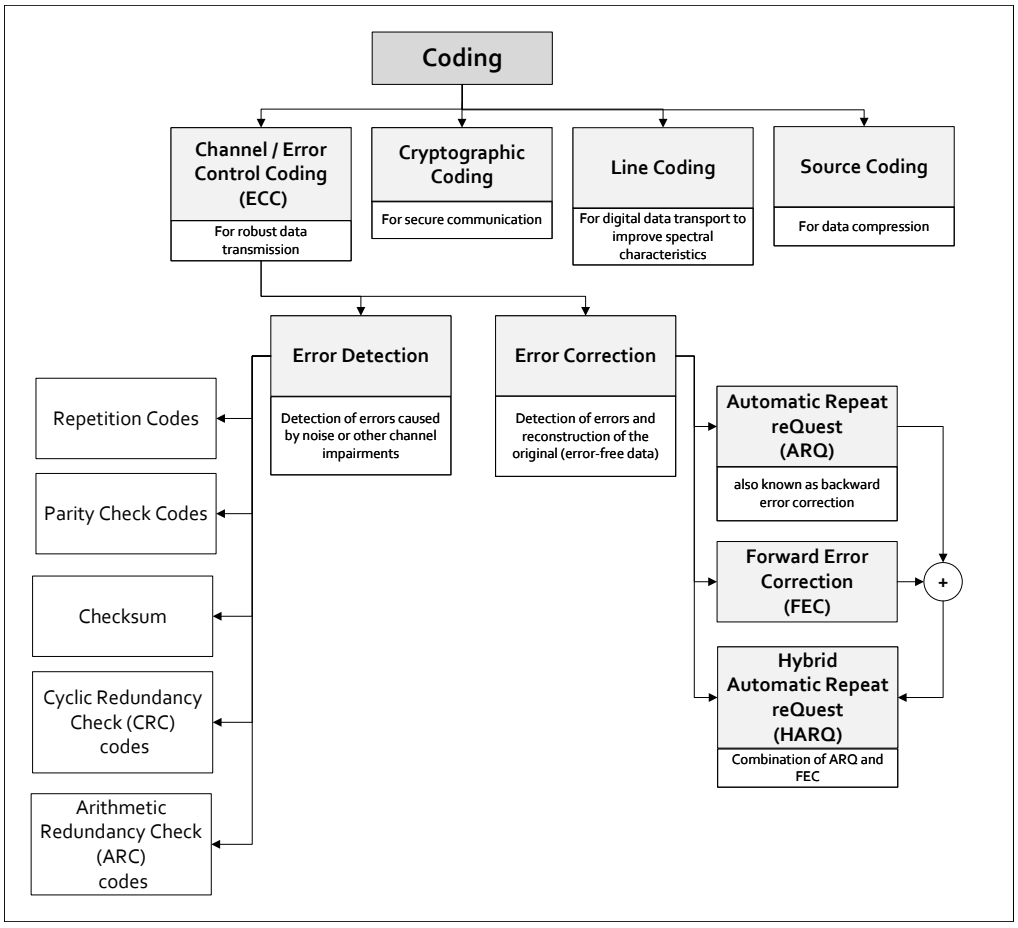

Figure 3.2.: Different types of coding: A comprehensive view.

Cyclic Redundancy Check (CRC), as described by [82], is a widely used error detection code in data communication and other serial data transmission systems. CRC, a type of linear block code derived from cyclic codes, is a powerful yet simple to implement technique [83]. In CRC, redundant bits, known as cyclic redundancy check bits, are added to the end of transmitted data, making the data exactly divisible by a predetermined binary number. At the receiver's end, the received data is divided by the same number. If there's no remainder, the data is assumed to be error-free and accepted. If a remainder is returned, it indicates that the received data is flawed and must be rejected. Error correction's role is to detect errors and reconstruct the original, error-

free data. Both error detection and error correction schemes add redundancy (additional data) to the original data, which receivers can use to check the consistency and accuracy of the received message and recover the original, error-free data.

Error detection and correction (ARQ) form the building blocks of error control mechanisms in communication systems. Data link layer error control is based on Automatic Repeat reQuest (ARQ) protocols [34]. If a packet is incorrectly received or missing, the destination requests the source to retransmit it. The data link layer, the second layer of the seven-layer open systems interconnection (OSI) model [84, 79], interprets the physical layer's bit stream as a sequence of data blocks and forwards them to the network layer. This layer ensures reliable data transfer across two physical links using flow control, error checking, acknowledgments, and re-transmission. These protocols can use error detection or correction codes to protect data from transmission errors and use a feedback channel to request message re-transmission, known as ARQ re-transmission.

Thus, error control techniques are implemented in three distinct ways using Forward Error Correction (FEC), ARQ, and Hybrid Automatic Repeat reQuest (HARQ) schemes. FEC schemes are equipped with properties that enable error correction through a suitably designed decoding algorithm. ARQ schemes pair an error detection method with requests for retransmission of incorrect data. Each received data block is checked using the error detection code, and if the check fails, a retransmission request is made. This process is repeated until error-free data is successfully received. HARQ is a combination of FEC and ARQ, aiming to reduce the number of retransmissions. Minor errors are corrected using FEC, and retransmission requests are only made if FEC decoding fails to recover the original data. Later in this chapter, various FEC, ARQ, and HARQ schemes are detailed, including their concepts, applications, and performance metrics. The chapter's main goal is to establish a common terminology for the FEC, ARQ, and HARQ schemes discussed in this work.

3.2. Reed-Solomon Codes

Forward Error Correction (FEC) is a widely used method for managing losses in real-time communication [27, 28]. FEC techniques allow a receiver to correct errors or losses without additional interaction with the sender, eliminating the need for retransmission of erroneous code words. This error correction is achievable when the codewords contain sufficient redundancy, enabling the receiver to determine the transmitted codeword, even if the received codeword contains errors [85, 86, 77]. FEC has been extensively applied to improve link performance in FSO channels [87, 88, 89]. If the original message appears unmodified in the transmitted data, the error correcting code is termed Systematic. In contrast, error correcting codes that do not include the original message in their output are called Non-Systematic. The portion of the output data stream considered useful is referred to as the Code Rate (or Information Rate). For instance, if the code rate is $r = k/n$, it implies that for every k symbols (such as bits, bytes, words, or packets) of data input, the error correcting code generates n symbols of output, where $n-k$ symbols are redundant. All error correcting codes introduce some overhead, calculated as $n-k$. As shown in Figure 3.3, the two primary types of FECs are Block Codes (systematic) and Convolution Codes (non-systematic)

[77, 79]. Both these types of codes have found extensive use in error control for communication and storage systems [77].

This section will concentrate mainly on the characteristics, applications, and error-correction potential of Reed-Solomon (RS) codes, which have been selected as the primary Forward Error Correction (FEC) for this thesis. Detailed analysis will be given to RS codewords, along with the computation of Symbol Error Probability (SEP) and Packet Error Probability (PEP). The calculated PEP values will subsequently influence the Automatic Repeat reQuest (ARQ) protocols, which will be discussed in detail in subsequent sections.

Designing a channel code often involves a trade-off between energy efficiency and bandwidth efficiency. Lower-rate codes, which have more redundancy, typically correct more errors. As a result, the communication system can operate at a lower transmit power, cover longer distances, withstand more interference, and transmit at a higher data rate. These properties generally make a code more energy efficient. However, lower-rate codes also have significant overhead and therefore consume more bandwidth. Furthermore, decoding complexity increases exponentially with longer code length, and long, low-rate codes impose high computational demands compared to conventional decoders. This decoding complexity is a central challenge of channel coding [90]: while encoding is straightforward, decoding is complex.

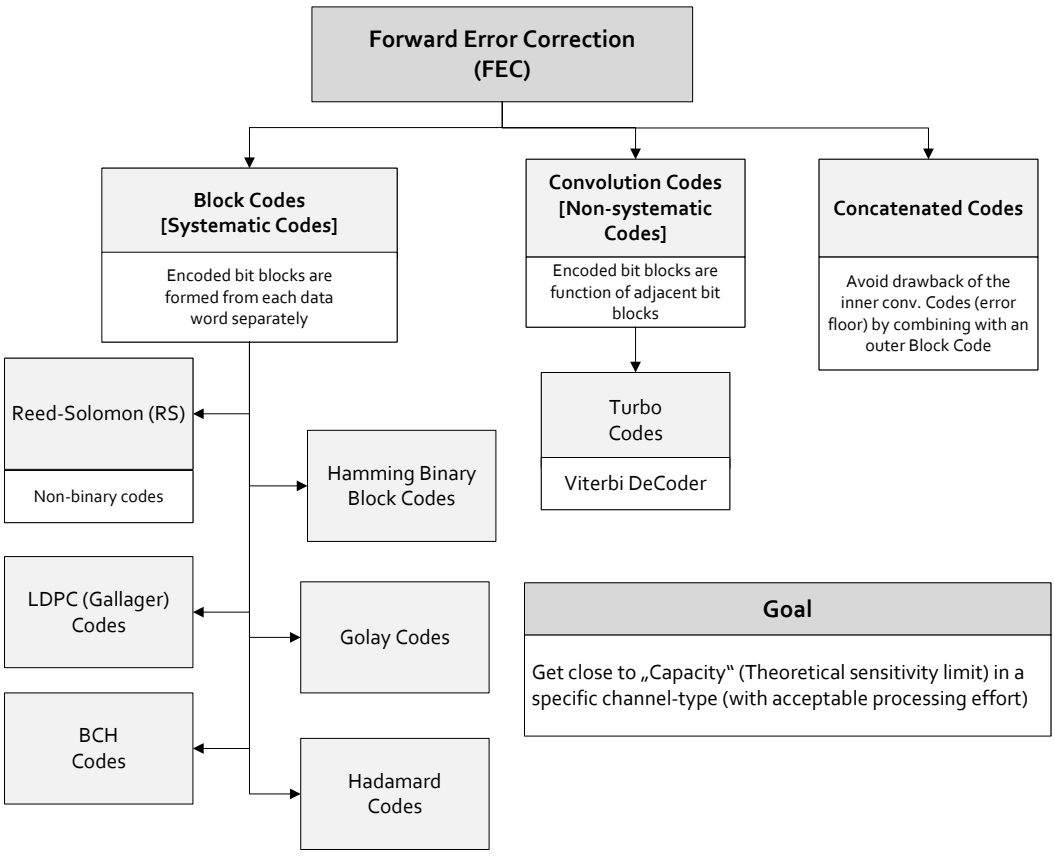

Figure 3.3.: An overview of various FEC types.

The Shannon-Hartley theorem [27] states that for every combination of bandwidth (B), channel type, received signal power (S), and received noise power (N), there exists a theoretical upper limit on the data transmission at a line rate (R). This limit is referred to as the channel capacity or Shannon capacity (C).

$$C = Blog_2\left(1+\frac{S}{N}\right) \qquad [bps] \tag{3.1}$$

- C channel capacity (bps)
- B bandwidth of the channel (Hertz)
- S average received signal power over the bandwidth
- N average power of the noise and interference over the bandwidth (Watt or volts-squared)

Shannon's theorem [27] states that if $R < C$, then the error probability at the receiver can be minimized to an arbitrary extent, making it theoretically possible to transmit nearly error-free data up to the channel capacity C. It's critical to note, however, that if R exceeds C, the error probability at the receiver rises due to the increased rate. This implies that beyond the channel capacity C, no viable data can be transmitted. The theorem also doesn't address the unique case where the rate and capacity are equal (R=C). In real-world conditions, there's no such thing as a perfect error-free channel. Instead, error-free data transmission implies that the bit error probability can be diminished to an arbitrarily small value. The bit error probability, or bit error ratio (BER), typically chosen for benchmarking is commonly around 10^{-9}. If the transmission rate, bandwidth, and noise power are fixed, a lower limit is set on the energy needed to transmit one bit of information. Thus, the Shannon capacity defines the energy efficiency limit of a code [91]. Despite several decades of progress, code designs have yet to approach the theoretical limit (Shannon's capacity).

This thesis concentrates on the application of Reed-Solomon (RS) codes with adaptive or variable code-rates. RS codes are vulnerable to random errors but exhibit high resilience against burst errors, which are continuous sequences of incorrect bits impacting multiple symbols [92]. This makes them ideally suited for channels with inter-HAP fading, which are more prone to burst errors. RS codes are frequently employed for error correction when the raw channel error rate remains moderately low, as they provide substantial error-correction capabilities with minimal redundancy.

RS codes are renowned systematic error-correcting block codes, commonly utilized for Forward Error Correction (FEC) to correct both random and burst errors on non-binary Galois fields, such as GF(256) [92]. These codes, developed by I. Reed and G. Solomon in 1960, are particularly adapt at tackling burst errors [93, 92]. The RS coding process involves encoding and decoding steps. During encoding, the input message is transformed into a longer codeword with additional bits added for error correction redundancy. Decoding involves retrieving the original message from the received codeword by leveraging the embedded redundancy. The performance of RS codes is determined by their error correction capability; longer codewords and lower data rates result in

more correctable errors. RS codes can be coupled with convolution codes and bit interleaving to enhance their performance, particularly useful in mitigating high error rates caused by burst errors [94]. Beyond data storage devices, wireless communications, digital television, and satellite communication networks, RS codes find broad applications in various communication, data storage, and networking systems [92, 94]. They have demonstrated efficacy in minimizing scintillation-induced fading in FSO links [95, 96, 97, 98].

3.2.1. RS Codeword

Reed-Solomon (RS) codes [99, 85, 100, 101] consist of symbols that are represented as sequences of m-bits, where m is any positive integer greater than 2. The structure of the RS code is shown in Figure 3.4.

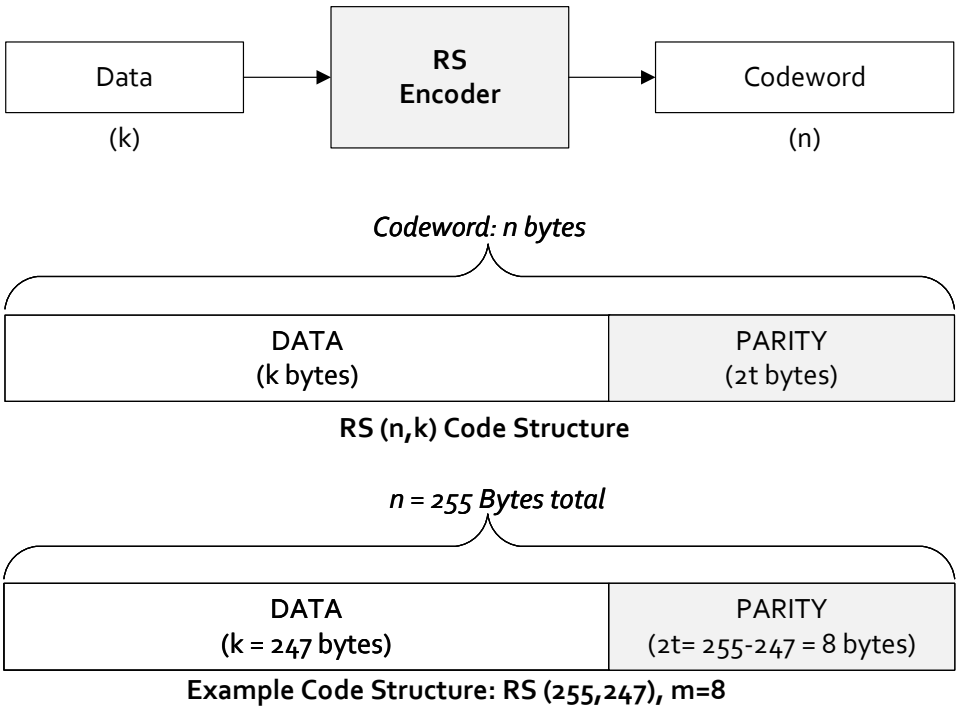

k	uncoded message length (in symbols)
$n = 2^m - 1$	codeword length (in symbols)
m	number of bits per symbol
$r = \frac{k}{n}$	code rate (unitless)
t	number of correctable errors (in symbols)
$2t = n - k$	parity length (in symbols)

Figure 3.4.: A basic overview of RS codeword.

RS (n,k) codes operate on m-bit symbols and are valid for all possible values of n and k.

$$0 < k < n < 2^m + 2 \tag{3.2}$$

k uncoded message length (symbols)
n codeword length (symbols)

For the most typical RS (n,k) code,

$$(n,k) = (2^m - 1, 2^m - 1 - 2t) \tag{3.3}$$

t symbol error correcting capability of RS code
$2t = n - k$ parity length (symbols)

In an extended RS code (that enhances the traditional Reed-Solomon code by adding a parity symbol, allowing for better error correction capabilities [85]), the greatest possible value for n can be,

$$n = 2^m \; or \; n = 2^m + 1 \tag{3.4}$$

RS codes maximize the code minimum distance for any linear code with identical encoder input and output block lengths, as stated in [85]. For non-binary codes, the distance between two codewords is defined, similarly to Hamming distance[1] [77], as the number of symbols where the sequences are different. For RS codes, the code minimum distance is determined by

$$d_{min} = (n - k) + 1 = 2t + 1 \tag{3.5}$$

The ability of the code to correct is determined by any mix of t or fewer errors, where the value of t is specified by

$$t = \left\lfloor \frac{d_{min} - 1}{2} \right\rfloor = \left\lfloor \frac{n - k}{2} \right\rfloor \tag{3.6}$$

As per Eq. (3.6), in the context of RS codes, correcting t symbol errors requires at most $2t$ parity symbols. This implies that the decoder has $n - k$ redundant symbols at its disposal, which is

[1] The Hamming distance measures the dissimilarity between two codewords by calculating the number of positions where their corresponding bits differ.

double the total correctable errors. Each error utilizes one redundant symbol to identify the error location and another to determine its correct value. The erasure-correcting capability, denoted as ρ, refers to a code's ability to recover original data symbols when some symbols are erased during transmission is given by

$$\rho = d_{min} - 1 = n - k \tag{3.7}$$

The capability for simultaneous error-correction and erasure-correction is provided as follows:

$$2\alpha + \gamma < d_{min} < n - k \tag{3.8}$$

α number of symbol-error patterns that can be corrected

γ number of symbol erasure patterns that can be corrected

The code rate is defined by the ratio of the total encoded data symbols to the overall count of code symbols in the encoded block. In the case of RS codes, the code rate can be formulated as,

$$r = \frac{k}{n} \qquad [unitless] \tag{3.9}$$

The code rate, r, satisfies $0 < r \leq 1$, where a rate approaching 1 means fewer repair symbols are generated. According to [85], the ideal code rate is around 0.6 to 0.7 for a Gaussian channel, 0.5 for a Rician-fading channel, and 0.3 for a Rayleigh-fading channel. Coding gain, which measures the difference in signal-to-noise ratio (SNR) needed for uncoded and coded systems to achieve the same bit error ratio (BER), degrades at both high and low code rates [79]. At high code rates, error performance worsens due to minimal coding. At lower rates, while coding improves error correction, increased redundancy reduces the energy per channel symbol, leading to more demodulation errors. This trade-off causes performance degradation at very low code rates despite increased redundancy. The structure of the RS code is shown in Figure 3.4, using the RS (255,247) code with 8-bit symbols. The code rate is 0.968 (247/255), with a codeword length of 255 bytes, 247 message bytes, and 8 parity bytes ($2t$), allowing correction of up to 4 symbol errors (t). Increasing parity bytes enhances error correction but requires more computation. According to [85], RS codes excel at correcting burst errors. The (255, 247) RS decoder can correct any 4-symbol errors, regardless of whether the symbol is fully or partially corrupted. This makes RS codes highly effective for managing burst noise, especially in inter-HAP FSO fading channels.

3.2.2. Symbol and Packet Error Probability

As stated earlier, Reed-Solomon (RS) codes are effective in addressing burst errors, defined as a sequence of consecutive errors impacting multiple symbols. These codes are also efficient on channels with memory, where the likelihood of an error is dependent on previously transmitted symbols. The use of RS code is particularly beneficial when a single bit of random error in the channel escalates into an 8-bits burst error after 8b/10b decoding. 8b/10b line decoding converts a 10-bit encoded data stream back into its original 8-bit binary format. This process is part of the 8b/10b encoding-decoding scheme used in digital communication systems, especially for serial data transmission. The encoding facilitates error detection, ensures reliable transmission, and maintains a balanced number of 1s and 0s (DC balance), which is crucial for signal integrity over long distances [79, 80].

For an RS (n, k) code, the optimal compatibility with 8b/10b is realized when m equals 8. Assuming that the channel bit error ratio, calculated using Eq. (2.17) from the RFE model detailed in Section 2.9.2, is represented as BEP, the Symbol Error Probability (SEP) can be determined accordingly. The equations below illustrate the SEP of an RS code in terms of the BEP [99]:

$$SEP = 1 - (1 - BEP)^{m+2} \qquad [unitless] \tag{3.10}$$

BEP	Bit Error Ratio/ Probability calculated using Eq. (2.17)
$m+2$	m represents symbol length (in bits) and $+2$ bits for the 10b coding.

The decoded Packet Error Probability (PEP) of an RS code indicates the chance that the decoder will output a flawed packet. This probability can be expressed in relation to the channel SEP, signifying the chance of a single symbol being received incorrectly. The following equations give the PEP of an RS code in terms of the SEP:

$$PEP = \sum_{i=t+1}^{n} \binom{n}{i} SEP^{i}(1 - SEP)^{n-i} \qquad [unitless] \tag{3.11}$$

$t = (n-k)/2$	error correcting capability of the RS code (symbols)
$n = 2^m - 1$	codeword length (symbols)
m	symbol length (bits)

The Figure 3.5 displays the error probability corresponding to varying mean received optical power. The Packet Error Probability (PEP) values are computed using Eq. (3.11), adjusting the number of uncoded message symbols (k), while maintaining a constant codeword length (n) of 255. We determine this value of n=255 ($2^m - 1$) with $m = 8$, which represents the number of bits per symbol.

The RS (255,255) showcases the uncoded PEP. As the value of k increases, implying lower code-rates ($r = k/n$), we observe an improvement in PEP values at the same received power, signifying reduced packet error. However, further improvements in PEP are not seen with an increase in received power. This highlights the maximum achievable performance of the RS code.

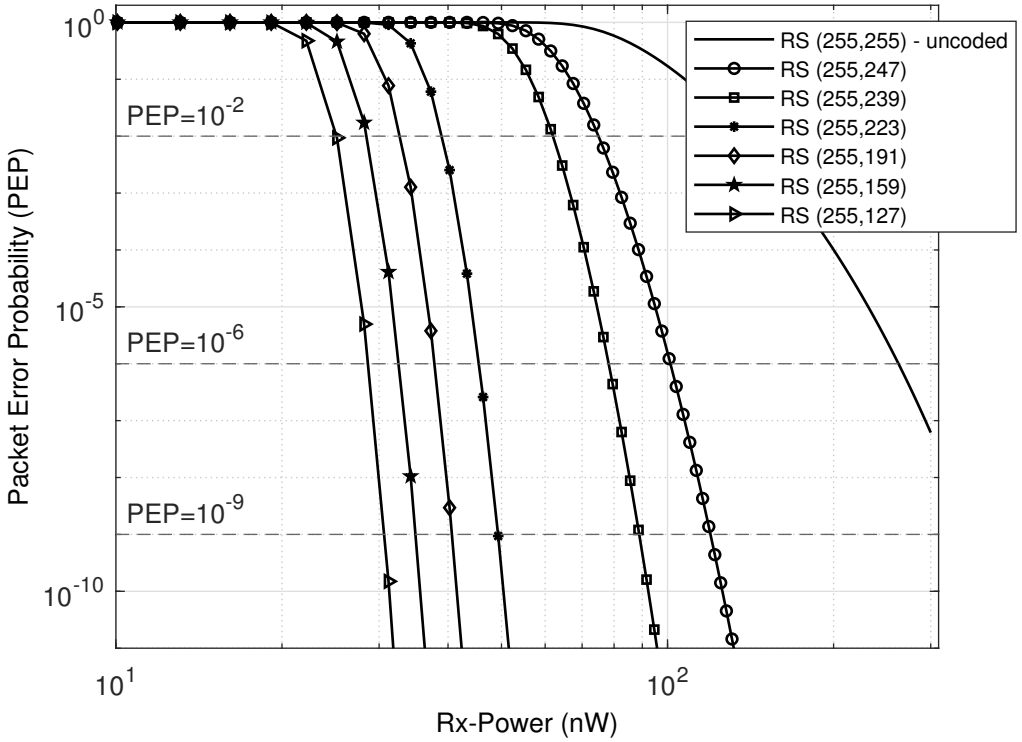

Figure 3.5.: RS packet error probability for different mean received power.

3.3. ARQ Schemes

Automatic Repeat Request (ARQ) is a pivotal strategy that guarantees the reliability of data transmission by identifying and rectifying errors during communication [102, 29, 78, 34]. This technique forms the basis for peer-to-peer protocols, ensuring accurate data delivery despite possible transmission errors. Error control methodologies are primarily split into two categories based on their complexity, detailed in the classification section. One way to tackle transmission errors is by integrating Forward Error Correction (FEC) schemes [81, 79, 77]. An FEC system applies error-correcting codes to data. When errors are identified at the receiving end, it attempts to locate and correct them. Even if complete error correction is not attainable, the data is still passed on to the upper layer. In contrast, when a feedback channel exists between the receiver and transmitter, ARQ schemes are employed to address transmission errors [78, 79]. Typically, an ARQ system uses robust error-detection codes, commonly CRC (Cyclic Redundancy Check) codes [78, 79]. These codes are attached to data packets and sent. Upon reception, these codes are used to verify for errors. If errors are detected, a retransmission request is initiated. For instance, the receiver sends a negative acknowledgment (NACK) or no acknowledgment over the feedback channel when errors

are identified, prompting the transmitter to resend the data. This process continues until error-free data transmission is accomplished. When a packet is received error-free, the receiver sends an acknowledgment (ACK) signal to the transmitter. Various retransmission strategies and schemes are tailored to match specific applications.

ARQ schemes are generally divided into two types [102, 34]: Stop-and-Wait ARQ (SW-ARQ) and window-based ARQ. In SW-ARQ, the transmitter sends a single frame and awaits the receiver's acknowledgment (ACK) before sending the next frame. If the ACK is not received, the frame is retransmitted. Despite its simplicity, SW-ARQ is not the most efficient due to its wait-for-acknowledgment nature. Conversely, window-based ARQ permits the transmitter to send multiple frames without awaiting individual acknowledgments, with the window size determining the number of frames that can be sent before acknowledgment. If an ACK is not received for any frame, all frames within the window are resent. Window-based ARQ is further sub-categorized into Go-Back-N (GBN) ARQ and Selective Repeat (SR) ARQ. GBN ARQ retransmits the entire window of frames if any frame within the window is not acknowledged, while in SR ARQ, only unacknowledged frames are resent. Hybrid ARQ (HARQ) schemes, which combine ARQ with FEC, enhance reliability. FEC introduces redundant bits into the data, enabling error correction at the receiver without the need for retransmission.

The selection of an ARQ scheme is contingent upon the particular requirements of the application. Despite SW-ARQ being the simplest to put into operation, it tends to be the least efficient specifically for longer Bandwidth Delay Product (BDP, see Section 3.4.3), longer distances, and channels with higher data rates. Window-based ARQ, while more efficient, requires a more complex implementation. HARQ, the most efficient ARQ scheme, presents the most significant implementation challenges. The selection of the most appropriate ARQ approach is dictated by the unique requirements of each communication scenario.

3.3.1. Stop and Wait ARQ

Stop and Wait ARQ (SW-ARQ) is a basic ARQ protocol where the transmitter sends a single frame and waits for an acknowledgment (ACK) from the receiver before transmitting the next frame [34]. If the ACK is not received, the frame is retransmitted. The simplicity of SW ARQ and its lack of need for frame numbering are its primary advantages. However, its efficiency is compromised as the transmitter can only send the next frame after receiving the ACK for the previous frame, leading to reduced efficiency at channels with longer Bandwidth Delay Product (BDP).

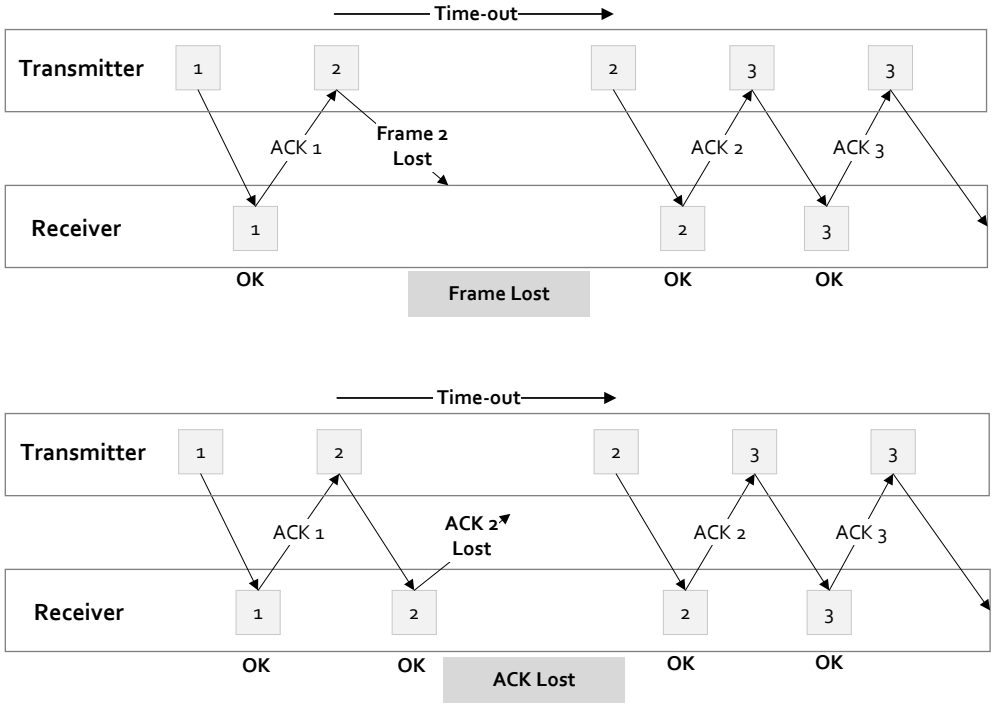

Figure 3.6.: SW-ARQ scheme: A working sequence example.

The sequence of events in SW-ARQ, as illustrated in Figure 3.6, is as follows:

1. The transmitter sends frame 1.
2. The receiver successfully receives frame 1 and sends an ACK.
3. Upon receiving the ACK, the transmitter sends frame 2.
4. The receiver successfully receives frame 2 and sends an ACK.
5. Upon receiving the ACK, the transmitter sends frame 3.
6. If a frame is lost or corrupted, the receiver will withhold the ACK, prompting the transmitter to start a timeout and retransmit the affected frame.

SW-ARQ's main advantage is its simplicity. It requires only two buffers: one for the currently transmitted frame and one for the currently received frame. Furthermore, the fact that there is theoretically only one frame in transit eliminates the necessity for frame numbering. Despite its simplicity, the efficiency of SW-ARQ is compromised as the transmitter can only send the next frame after receiving the ACK for the previous frame. This can result in lengthy delays. In certain specific scenarios, FEC systems can be more efficient compared to SW-ARQ because they can correct errors without requiring retransmission. This enables the transmitter to send additional frames without the need to wait for ACKs [79, 35].

3.3.2. Go Back-N ARQ

Go-Back-N (GBN) ARQ is a sliding window protocol that enables the transmitter to send several frames without awaiting an acknowledgment for each frame [34, 79]. The window size represents the number of frames that can be in transit at any given moment. In GBN-ARQ, if a frame is lost or corrupted, the receiver discards all subsequent frames. The transmitter then resends the lost frame and all frames that followed it. The primary advantage of GBN-ARQ is its efficiency compared to SW-ARQ, as the transmitter doesn't need to wait for an acknowledgment for each frame. This can enhance the communication system's throughput. However, GBN-ARQ can be inefficient if there are numerous lost or corrupted frames, as the transmitter must resend all frames following the lost or corrupted frame.

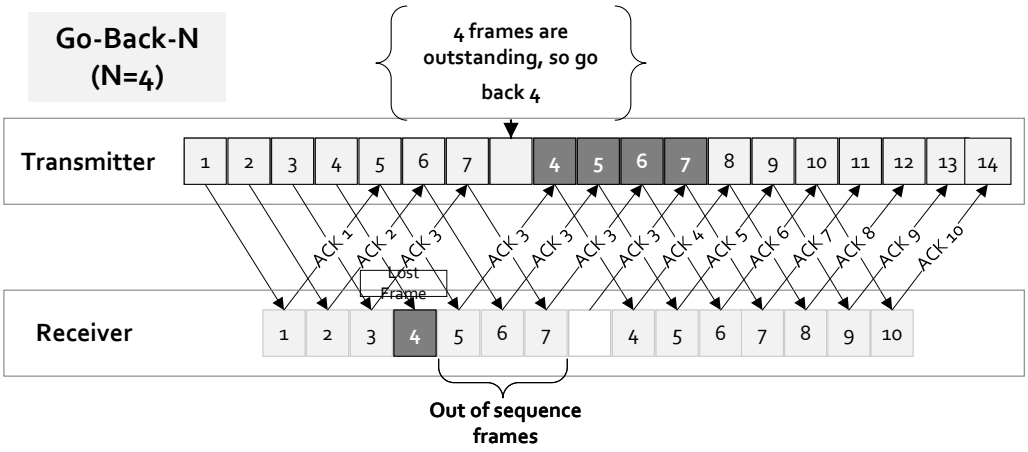

Figure 3.7.: Go Back-N ARQ scheme: A working sequence example.

The sequence of a Go-Back-N ARQ (GBN-ARQ) scheme, as illustrated in Figure 3.7, is as follows:

1. The transmitter sends Frame 1 through Frame 4 (window size, N=4) to the receiver.

2. Frames 1 to 3 are correctly received, and their corresponding ACKs are sent to the transmitter. Meanwhile, the transmitter continues to send frames into the channel. In this scheme, frames are pipelined[2] to keep the channel busy.

3. The term GBN-ARQ originates from the action taken when an error occurs. As shown in Figure 3.7, if Frame 4 encounters errors, the receiver discards Frame 4 and all subsequent out-of-sequence frames (5, 6, and 7).

4. The transmitter only receives repeated ACK 3 frames upon the loss of Frame 4.

[2] A procedure in which the processing of a new task has started before the completion of a previous task.

5. Eventually, the transmitter reaches the maximum number of outstanding frames and is compelled to go back N frames, where N=4 (window size), and start retransmitting all frames from Frame 4.

In this scenario, the transmitter retransmitted frames 4, 5, 6, 7 even though frames 5, 6, and 7 were received correctly. Due to the transmitter's lack of knowledge regarding which frame was lost, GBN-ARQ utilizes Cumulative Acknowledgment (CACK) and Selective Acknowledgment (SACK). CACK and SACK are advanced variants of Go-Back-N. In CACK-based ARQ, multiple unacknowledged packets exist, but ACKs indicate the highest numbered packet received in order, with retransmissions triggered by timeouts or duplicate CACKs. CACKs address lost ACKs on the reverse channel. However, SACK-based ARQ is superior as it not only performs CACK functions but also identifies recently received non-consecutive packets, enabling the sender to pinpoint packet losses and selectively retransmit only those packets.

3.3.3. Selective Repeat ARQ

Selective Repeat (SR) ARQ is an enhancement over Go-Back-N (GBN) ARQ. In SR-ARQ, the receiver can accept frames out of order, and the transmitter only retransmits frames that the receiver has not acknowledged [103, 102, 79]. This makes SR-ARQ more efficient than GBN-ARQ, especially in channels with high error rates. The key difference between SR-ARQ and GBN-ARQ lies in their handling of lost frames. In GBN-ARQ, if a frame is lost, the transmitter retransmits the entire window of frames, which can be inefficient if the lost frame is at the end of the window. In contrast, SR-ARQ only retransmits the lost frame, reducing unnecessary retransmissions and enhancing efficiency. Implementing SR-ARQ requires the receiver to have a buffer to store out-of-order frames and the transmitter to have a timer for each sent frame. If the timer expires, the frame is retransmitted. Although SR-ARQ is the most efficient of the three ARQ schemes discussed, it is also the most complex.

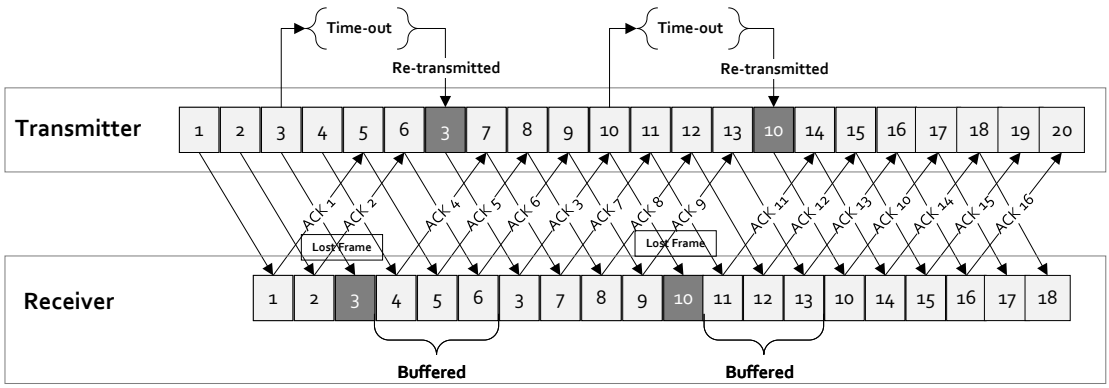

Figure 3.8.: SR ARQ scheme: A working sequence example.

An example of the SR-ARQ protocol is shown in Figure 3.8. The receiver acknowledges all correctly received frames, regardless of their order. The receiver buffers out-of-order frames until all frames with lower sequence numbers have been received. Then, the receiver delivers the frames to the upper layer in order. In the example, frames 3 and 10 are lost at the receiver. The transmitter, unaware of this, continues to send new frames. When the timeout for frame 3 expires, the transmitter retransmits frame 3, and the same happens for frame 10. The receiver buffers frames 2, 4, 5, 6, 7, 8, 9, and 11. When frame 3 is received, the receiver delivers frame 4 and and the following frames to the upper layer. When frame 10 is received, the receiver delivers frame 11 and the following frames to the upper layer. The receiver must have a sufficiently large buffer to store all out-of-order frames. If the buffer is not large enough, some frames may be lost.

3.3.4. Hybrid ARQ Schemes

Hybrid Automatic Repeat Request (HARQ) is a communication protocol that combines Forward Error Correction (FEC) and automatic repeat request (ARQ) techniques to enhance communication reliability, particularly in noisy wireless channels [104, 29, 105, 30]. The limitations of ARQ and FEC systems can be mitigated by combining these error control strategies in a hybrid ARQ. HARQ encompasses three primary types [33]: Type I, Type II, and Type III.

Type I HARQ [104, 29, 105] employs a cyclic redundancy check (CRC) to detect transmission errors. Upon error detection, the receiver requests retransmission, and this process continues until successful decoding or reaching the maximum retransmission limit. An extension of Type I, known as Chase Combining, preserves incorrect packets to combine then with later retransmissions, improving the received signal-to-noise ratio without requiring additional coding gain.

Type II HARQ [30, 106, 107, 108], also referred to as full incremental redundancy (IR), sends a new set of coded bits with each retransmission to introduce diversity. Unlike Chase Combining, the receiver combines these new bits with previous attempts, resulting in higher coding gain but a lower code rate with each retransmission.

Type III HARQ [109, 33], or partial incremental redundancy, includes extra redundancy bits in retransmissions to lower the coding rate. This approach maintains the self-decoding capability during retransmissions, enabling chase combining with earlier packets to enhance diversity gain.

Each type of HARQ serves a distinct function to maximize reliability and throughput in wireless communication systems. This thesis in Chapter 4 introduces a novel concept of an adaptive code rate-based HARQ system in the context of addressing atmospheric turbulence and pointing errors that occur in inter-High Altitude Platform (HAP) Free-Space Optical (FSO) channels.

3.4. ARQ Performance Metrics

In the previous sections, we have discussed the fundamental working concept of ARQ schemes. In this section, we will explore the performance metrics associated with these ARQ schemes and the

important parameters related to them. The primary objective of an ARQ scheme is to ensure the reliable transmission of information frames by allowing for repeated transmissions until correct decoding is achieved. However, this reliability comes at the cost of increased delays, primarily due to round-trip time. In some cases, multiple retransmissions may be necessary for successful frame decoding. One crucial performance metric is the delay, which represents the average time required for the ARQ scheme to transmit a frame correctly. To strike a balance between reliability and delay, a maximum retransmission limit can be established. It is important to note that in practice, there are additional factors that contribute to the overall delay. These factors have been discussed in references such as [32, 79].

3.4.1. ARQ Delay

ARQ delay refers to the average time required for an ARQ scheme to complete its operations after successfully decoding a frame [34]. This delay encompasses various components, including the propagation delay (t_{prop}) and the processing delay (t_{proc}) at the receiver's end. The propagation delay accounts for the time it takes for a signal to travel one way between the sender and receiver, while the processing delay arises from tasks such as demodulation, decoding, and error detection performed by the receiver. These delays are of great significance as they directly impact the overall time required for reliable transmission and reception of data in a communication system. Understanding the ARQ delay is crucial for assessing the performance of ARQ protocols and evaluating their efficiency. The propagation delay (t_{prop}) is inherent to the physical distance between the sender and receiver and cannot be avoided. On the other hand, the processing delay is influenced by the complexity of the receiver's hardware and software. Optimizing this processing delay can lead to more efficient communication systems. In summary, in addition to the inherent (re-transmission) ARQ delay, the propagation delay and processing delay play significant roles in determining the total time taken for data to travel from the sender to the receiver in a communication system. References such as [34, 79] provide further insights into these considerations.

In this thesis, we consider t_{proc} to be insignificant. Additionally, we utilize the forward channel for transmitting information, while the backward channel is assumed to be error-free and solely used for sending acknowledgments (ACKs).

3.4.2. Transmission Time

The transmission time of a packet, denoted as t_{packet}, represents the duration required for a packet to be sent from the transmitter until the final bit exits the transmitting node. In the context of data frame transmission, each transmission takes place within a predefined time slot, and these transmissions are subject to the application of ARQ protocols. The calculation for the transmission time of a packet is as follows:

$$t_{packet} = \frac{n_{total}}{R_{net}} \qquad [seconds] \tag{3.12}$$

t_{packet} transmission time (in seconds)
n_{total} total number of bits in the information packet (bits)
R_{net} net data rate after 8b/10b line coding (bps)

3.4.3. Bandwidth Delay Product

The Bandwidth Delay Product (BDP) is a measure of the amount of data that can be in transit within a network at a specific time. It is determined by two main factors: the available network bandwidth and the network's latency. The BDP is calculated by multiplying the net data rate by the ARQ delay. The formula provided below can be used to calculate the bandwidth delay product [34]:

$$BDP = 2(t_{prop} + t_{proc}) \cdot R_{net} \qquad [bits] \tag{3.13}$$

In this thesis, we assume that the processing time t_{proc} to be insignificant (zero) results in

$$BDP = 2(t_{prop} + 0) \cdot R_{net} \qquad [bits]$$

$$BDP = t_{RTT} \cdot R_{net} \qquad [bits] \tag{3.14}$$

R_{net} net data rate after 8b/10b line coding (bps)
t_{prop} propagation time/ delay (seconds)
t_{RTT} round-trip time (seconds)

3.4.4. Throughput/ Transmission Efficiency

In accordance with the definition provided by [102], throughput/transmission efficiency or efficiency is conventionally defined as the ratio of the average number of successfully received information bits during a given time period to the total number of bits that could theoretically be transmitted during the same time frame. However, in the context of this thesis, the term Transmission Efficiency (TE) takes on a distinct meaning. TE is the payload transport throughput of the system, normalized by the maximum channel bit rate (prior to 8b/10b encoding) during the transmission phase. TE is a dimensionless metric with a range between 0 and 1. This particular definition of TE permits a more precise evaluation of the system's performance in terms of its efficient utilization of available channel capacity for the transmission of valuable data. By standardizing throughput relative to the maximum channel bit rate, TE establishes a standardized metric that enables comparisons across a variety of systems and situations. TE emerges as a valuable metric for assessing

transmission efficiency in the context of this thesis. Transmission efficiency in the context of ARQ protocols refers to the ratio of successfully transmitted data bits to the total number of transmitted data bits, taking into account retransmissions due to channel errors. It reveals how effectively these ARQ protocols utilize the available channel capacity. These protocols' transmission efficiency, as described in [34], can be estimated as follows:

ARQ Protocol	**Throughput/ Transmission Efficiency**
Stop and Wait	$TE = (1-PEP)\frac{1-\frac{n_{overhead}}{n_{packet}}}{1+\frac{n_{ack}}{n_{packet}}+\frac{2(t_{prop}+t_{proc})R_{net}}{n_{packet}}}$ In this thesis, t_{proc} is insignificant (zero) and $2t_{prop} = t_{RTT}$ results in $TE = (1-PEP)\frac{1-\frac{n_{overhead}}{n_{packet}}}{1+\frac{n_{ack}}{n_{packet}}+\frac{t_{RTT}\cdot R_{net}}{n_{packet}}}$ (3.15)
Go-Back-N	$TE = (1-PEP)\frac{1-\frac{n_{overhead}}{n_{packet}}}{1+(W_s-1)PEP}$ (3.16)
Selective Repeat	$TE = (1-PEP)\left(1-\frac{n_{overhead}}{n_{packet}}\right)$ (3.17)

Table 3.1.: Summary of transmission efficiency: ARQ protocols.

TE	Transmission efficiency (unitless)
PEP	Packet Error Probability (unitless)
n_{packet}	number of bits in the information packet (bits)
$n_{overhead}$	number of overhead bits in the information packet (bits)
n_{ack}	Number of bytes in an ACK/NACK packet (bits)
W_s	window size (measured in packets)
t_{RTT}	round-trip time (seconds)
R_{net}	net data rate after 8b/10b line coding (bps)

3.4.5. Coding Gain

The *coding gain*, as defined in [85], is the decrease in E_b/N_0 that can be obtained by using a code for a particular Bit Error Probability (BEP). The general equation for the coding gain G, measured in dB, is:

$$G\,[dB] = \left(\frac{E_b}{N_0}\right)_{uncoded}[dB] - \left(\frac{E_b}{N_0}\right)_{coded}[dB] \tag{3.18}$$

$\left(\frac{E_b}{N_0}\right)_{uncoded}$	required E_b/N_0 uncoded (dB)
$\left(\frac{E_b}{N_0}\right)_{coded}$	required E_b/N_0 coded (dB)
E_b	energy per information bit
N_0	noise spectral density at the receiver
G	coding gain (dB)

This thesis presents performance results in terms of coding gain, which denotes the decrease in mean optical received power ($\overline{P}_{rx}$) in nW, achievable with our adaptive Forward Error Correction (FEC) code-rate Hybrid Automatic Repeat reQuest (HARQ) scheme to attain a particular Transmission Efficiency (TE). These results are detailed in Section 6.3.3. The modified version of Eq. (3.18) to our case, is given by:

$$Coding \quad Gain\,[dB] = \left(\overline{P}_{rx}\right)_{uncoded} - \left(\overline{P}_{rx}\right)_{coded} \tag{3.19}$$

$\left(\overline{P}_{rx}\right)_{uncoded}$	required mean received power uncoded (nW)
$\left(\overline{P}_{rx}\right)_{coded}$	required mean received power coded (nW)

The “uncoded” refers to the mean received power ($\overline{P}_{rx}$) required for an ARQ scheme without FEC coding to achieve a particular TE. On the other hand, the “coded refers to the $\overline{P}_{rx}$ with a HARQ scheme that includes both ARQ and Reed-Solomon coding to achieve a particular TE.

3.4.6. ARQ Parameters

ARQ Parameters	Unit	Description
n_{total}	$bits$	Total number of bytes in the information packet
n_{packet}	$bits$	Number of bytes in the information packet or total number of code symbols in the encoded block.
$n_{overhead}$	$bits$	Number of overhead bytes in a packet includes header and CRC
n_{ack}	$bits$	Number of bytes in an ACK/NACK packet
t_{packet}	$seconds$	Transmission time of a packet
t_{prop}	$seconds$	Propagation time
t_{RTT}	$seconds$	Round-trip time
t_{proc}	$seconds$	Processing time
W_s	$packets$	Window size
R_{net}	bps	Net data rate
L	m	Link distance
PEP	unitless	Packet Error Probability (PEP) or probability that a packet transmission has errors.
TE	unitless	Transmission efficiency

Table 3.2.: List of ARQ parameters.

3.5. Optimal ARQ Selection for FSO Inter-HAP Links

In Free Space Optical (FSO) communication systems, ARQ schemes are commonly employed to address channel impairments like fading and blockage, especially at higher data rates. Numerous studies have explored the integration of ARQ in FSO links to enhance communication reliability, including [110, 3, 111, 112, 113, 9, 114]. It is important to note that not all FSO applications can be addressed by a single ARQ scheme. Instead, the selection of an ARQ scheme should consider the bit error probability (BEP) and fading statistics of the FSO Inter-HAP channel, tailored to the specific atmospheric channel and scenario. This study's simulations aim to evaluate the performance of different ARQ schemes under various fading conditions by analyzing the characteristics of Packet Error Probability (PEP). The objective is to identify suitable ARQ schemes that minimize the effects of fading and maximize transmission reliability in FSO inter-HAP fading channels, focusing on the PEP characteristics. This comparative study assesses the ARQ schemes described in Section 3.3, using PEP as an input parameter that aligns with the PEP range of a typical inter-HAP FSO fading channel, accounting for atmospheric turbulence and pointing error as presented in Sec-

tion Section 2.4 and Section Section 2.4 respectively. The results of this investigation will guide the selection and implementation of ARQ schemes, ensuring optimal adaptation to the distinct fading properties of the channel. The ultimate goal is to enhance FSO inter-HAP communication performance and reliability in challenging atmospheric conditions. These findings will contribute to the development of reliable and effective ARQ schemes for FSO inter-HAP fading channels.

3.5.1. Assumed ARQ Parameters

The assumed parameters for this evaluation are summarized in Table 3.3. In this analysis, we assume a propagation time of $t_{prop} = 2ms$ which corresponds to a typical inter-HAP link distance of $L = 600km$, considering the speed of light as $3 \times 10^8 m/s$. Also, a processing time of $t_{proc} = 0$. Furthermore, we consider a net channel data rate of $R_{net} = 1Gbps$, representing a high-speed optical link. The total packet length is $n_{total} = 255bytes$, with an overhead of $n_{overhead} = 8bytes$, resulting in a code-rate of 0.96, as calculated using Eq. (3.9). Additionally, we assume that the acknowledge packet size, n_{ack}, is the same length as the total packet length. Additionally, the BDP, as described in 3.4.3, is calculated using Eq. (3.14) by multiplying the channel's data rate by twice the sum of the propagation delay and the processing time, taking into account both the forward and backward channels. For our analysis, the PEP is calculated using Eq. (3.11). The input BEP required to calculate PEP is determined using Eq. (2.17), considering the RFE model described in Section 2.9.2.

ARQ Parameters	**Value (unit)**	**Description**
n_{total}	255 ($bytes$)	Total number of bits in the information packet
n_{packet}	247 ($bytes$)	Number of bits in the information packet or total number of code symbols in the encoded block.
$n_{overhead}$	8 ($bytes$)	Number of overhead bits in a packet includes header and CRC
n_{ack}	255 ($bytes$)	Number of bits in an ACK packet
R_{net}	1 ($Gbps$)	Net data rate
L	600 (km)	Link distance
t_{prop}	2 (ms)	Propagation time
t_{proc}	0	Processing time
W_s	2048 ($packets$)	Window size

Table 3.3.: Detailed list of assumed parameters for ARQ simulation in optimal ARQ selection.

3.5.2. Evaluating ARQ Schemes: A Quantitative Comparison

In this section, we present a quantitative comparison of the transmission efficiencies of selected ARQ schemes to highlight their performance differences. We assume symmetrical channels, resulting in the same Packet Error Probability (PEP) values for both the forward and backward channels. To simplify the analysis, we consider a unidirectional flow of information with the ACK signal transmitted over the back channel. Several important parameters heavily influence the system's performance, including total packet length, Bandwidth Delay Product (BDP), and PEP. The ARQ parameters defined in Table 3.3 are used to evaluate transmission efficiency across different ARQ schemes. These parameters control the allocation of channel bit rate for payload transport, thus affecting transmission efficiency.

Figure 3.9 illustrates the transmission efficiencies of three ARQ schemes across various parameter metrics. In Figure 3.9 (a), we compare the TE of SW-ARQ for different net data rates at a link distance of 600 km. The performance of SW-ARQ declines as the data rate increases, and it becomes negligible for higher data rates such as 500 Mbps and 1 Gbps. Furthermore, we observe a decrease in TE for larger BDP ($2(t_{prop}+t_{proc})\times R_{net}$) values, which is attributed to the requirement of a successful ACK before transmitting the next packet. This decrease is particularly prominent at higher data rates. In Figure 3.9 (b), we analyze the TE of GBN-ARQ for different window sizes (W_s). As the ARQ window size (W_s) increases, the performance of GBN-ARQ deteriorates. This degradation is attributed to the average wasted time of (W_s-1) PEP, as described in Eq. (3.16). However, selecting smaller window sizes (e.g., 2, 8, and 64) to achieve a desired range of PEP (ranging from 10^{-6} to 10^{-2}) results in an underutilization of the channel. As shown in Figure 3.9 (c), SR-ARQ performs best within the desired range of PEP values.

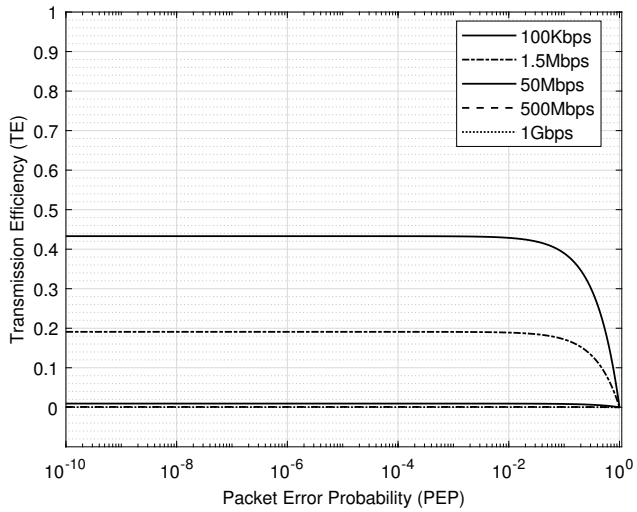

(a) TE of the Stop-and-Wait ARQ (SW-ARQ) scheme is evaluated for a link distance (L) of 600 km and net data rates of 100 Kbps, 1.5 Mbps, 50 Mbps, 500 Mbps, and 1 Gbps.

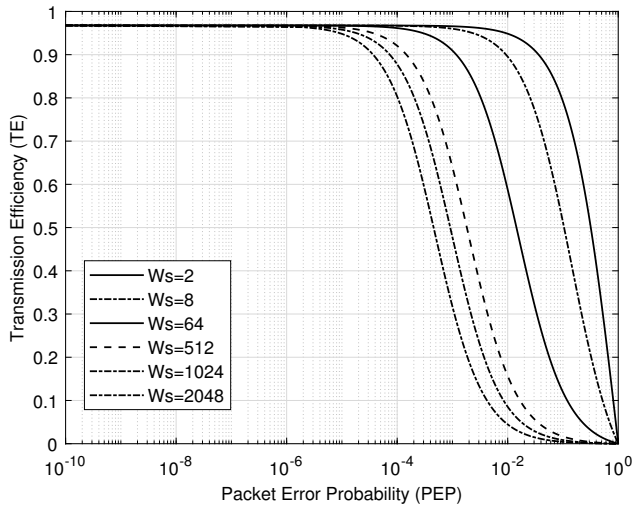

(b) TE of the Go-Back-N ARQ (GBN-ARQ) scheme is examined for a link distance (L) of 600 km and a net data rate of 1 Gbps. This evaluation takes into account six different ARQ window sizes (W_s).

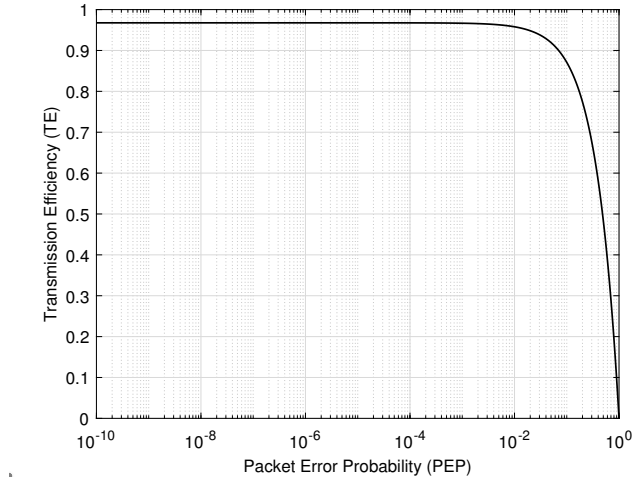

(c) TE of the Selective Repeat ARQ (SR-ARQ) scheme is assessed for a link distance (L) of 600 km and a net data rate of 1 Gbps.

Figure 3.9.: Quantitative evaluation of the Transmission Efficiency (TE) of ARQ schemes.

To summarize, these findings highlight the importance of carefully considering various factors and trade-offs when selecting an optimal ARQ scheme. SW-ARQ may exhibit reduced efficiency in scenarios with high BDP, GBN-ARQ and SR-ARQ can result in channel underutilization when using small window sizes, and SR-ARQ performs well within a specific range of PEP. It is worth noting that SR-ARQ requires buffering of up to Ws frames at both the transmitter and receiver,

while GBN-ARQ only requires buffering of up to Ws at the transmitter. Higher data rates necessitate larger window sizes. In this study, our system configuration adopts a standardized code length of 255 bytes for all transmissions (referred to as n_{total}, representing the total number of bits in the information packet). This code length is equivalent to 2040 bits when using 8-bit symbols. Additionally, we assume a net data rate of 1 Gbps (denoted as R_{net}). Consequently, on average, a data frame is transmitted every 2.04 μs. Upon successful receipt of a frame, the receiver promptly sends an error-free acknowledgment (ACK) signal at intervals of 2.04 μs.

Figure 3.10 illustrates a comprehensive performance comparison of three distinct ARQ protocols. The aim is to determine the maximum achievable transmission efficiency while taking into account the PEP range of a typical inter-HAP FSO fading channel, which considers atmospheric turbulence and pointing error. The assumed values for this analytical comparison are presented in Table 3.3. Additionally, a window size (W_s) of 2048 is selected for GBN-ARQ. The results show that SW-ARQ exhibits negligible performance, remaining at zero throughout the entire range of PEP values. Conversely, GBN-ARQ demonstrates optimal performance up to a PEP of 10^{-5}, but its effectiveness declines beyond this threshold, reaching a minimum at approximately 10^{-2}. Interestingly, SR-ARQ surpasses the other two schemes for PEP values up to 10^{-2}. However, its performance also begins to deteriorate beyond this point. Consequently, considering its superior performance within the desired range of PEP, SR-ARQ is recommended as the optimal choice for FSO inter-HAP scenarios. By comprehending the trade-off between PEP and transmission efficiency, informed decisions can be made to maximize performance in similar scenarios involving long links and high scintillation indexes.

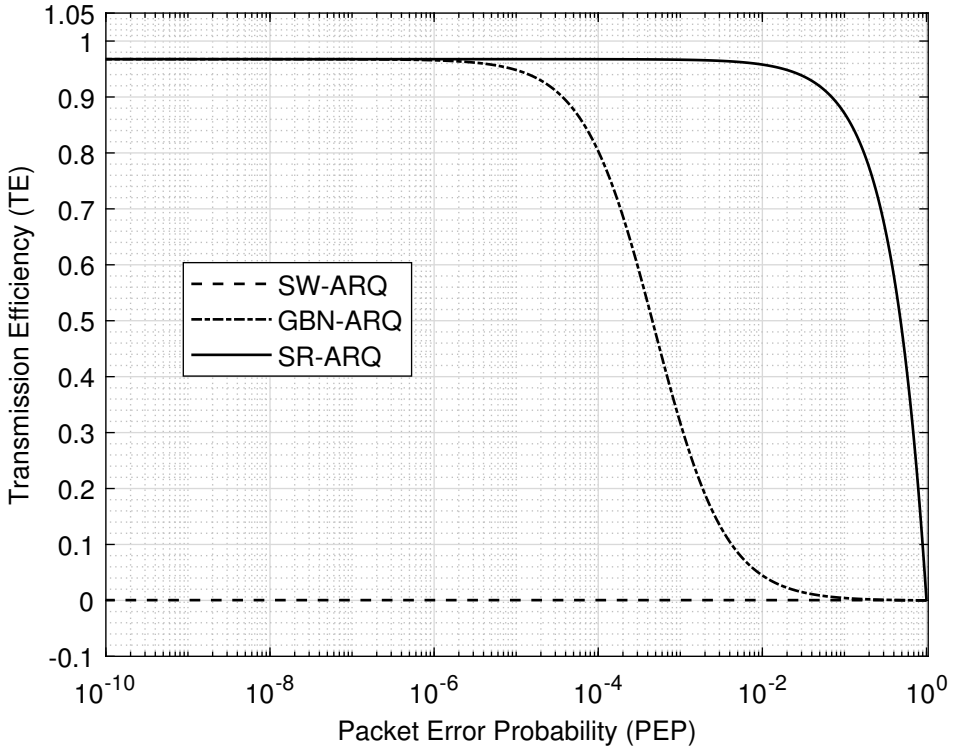

Figure 3.10.: Numerical comparative analysis of the Transmission Efficiency (TE) among various ARQ schemes.

In these scenarios, SW-ARQ shows poor performance and is not recommended for this thesis. GBN-ARQ is unsuitable for higher data rates due to its larger window size requirement and significant performance deterioration at PEP values of 10^{-5}. Thus, SR-ARQ emerges as the preferred choice for further exploration, especially for FSO inter-HAP fading channels. It is the most efficient of the three ARQ schemes, avoiding transmission gaps and retransmitting only incorrectly received frames [79, 35], although it does require more buffers at both ends. Additionally, hybrid ARQ schemes combine features from different ARQ methods, such as using SR-ARQ primarily but switching to GBN-ARQ when the receiver buffer is exceeded. A study on the throughput efficiency of these schemes found that SR-ARQ performs best in high error rate channels, while GBN-ARQ is more effective in low error rate conditions [79].

3.6. Chapter Summary

This chapter offered a comprehensive overview of Forward Error Correction (FEC) schemes, particularly emphasizing the Reed-Solomon (RS) scheme. An in-depth examination of the RS scheme was conducted, along with the rationale for its selection. The chapter further provided a detailed exploration of various fundamental Automatic Repeat reQuest (ARQ) schemes, explaining their operational principles and applications. A concise overview of Hybrid ARQ (HARQ) types was also included. Building on ARQ basics, the chapter elaborated on performance metrics necessary for evaluating these schemes. The main objective of this chapter was to determine the optimal ARQ scheme for this thesis through a meticulous comparison and evaluation of different ARQ schemes. The research indicated that Selective Repeat ARQ (SR-ARQ) performs most efficiently in high-error-rate channels, hence its selection for this thesis. Conversely, Sliding Window ARQ (SW-ARQ) and Go-Back-N ARQ (GBN-ARQ) were disregarded due to their inadequate performance, rendering them unsuitable for our inter-High Altitude Platform (HAP) Free Space Optics (FSO) channel.

4 Adaptive Code-Rate Hybrid ARQ with CSI-Based Selection

This chapter presents a comprehensive proposal for implementing efficient error control across different Channel State Information (CSI) types. The reasoning behind this approach is outlined in Section 4.1, offering a solid foundation for its inception. A concise summary of the various types of CSI, focusing on the methods employed in this thesis and the utilization of reciprocal CSI, can be found in Section 4.2. The principle of code-rate selection is comprehensively elaborated in Section 4.4. Moreover, Section 4.5 clarifies the system concept and its association with the Hybrid Automatic Repeat Request (HARQ) schemes. Concluding the chapter, Section 4.6 encapsulates the main points discussed, providing a recap of the essential details.

4.1. Motivation

This chapter aims to introduce the concept of adaptive Forward Error Correction (FEC) code-rate selection in Hybrid Automatic Repeat Request (HARQ) protocols, considering different types of Channel State Information (CSI). Incorporating CSI within HARQ in Free Space Optical (FSO) communication systems offers numerous advantages, leveraging the long coherence time of the FSO channel. By incorporating CSI, adaptive retransmission strategies become possible, enabling optimized link adaptation. This adaptability allows for improved efficiency in retransmissions and error correction techniques, resulting in enhanced reliability and data rates. Previous studies have explored FSO system performance without explicit reliance on CSI, but the benefits of integrating CSI into HARQ are evident [115, 116, 117]. CSI provides valuable information for efficient resource allocation, error correction, and adaptive retransmissions, significantly improving the performance of FSO communication systems.

In this thesis, a novel approach is proposed to handle various types of CSI. The goal is to adjust the FEC code-rate based on the specific CSI type. This approach involves selecting the best code-rate according to the CSI type. To maximize transmission efficiency for each CSI type, an adaptive code-rate selection look-up table is suggested. This technique is integrated into the Selective Repeat (SR) ARQ mechanism.

4.2. Channel State Information (CSI)

Channel State Information (CSI) is an essential element in wireless communications, providing insights into the characteristics of a communication link. This information allows the transmitter to modify transmissions based on the current channel conditions, ensuring reliable communication with high data rates. CSI can be estimated at the receiver and then relayed to the transmitter, a process known as channel state information at the transmitter (CSIT). However, the rapid variations in the channel can make obtaining accurate CSIT challenging [115, 116, 39, 117]. In Free Space Optics (FSO) links, CSI estimation can be achieved by measuring the received optical power. This measurement allows the transmitter to adapt the transmission power and modulation scheme accordingly [115, 117]. CSI significantly enhances the performance of wireless communication systems by enabling efficient resource allocation, error correction, and adaptive retransmissions.

As depicted in Figure 4.1, CSI can be classified into two main types [118, 119]: Instantaneous CSI and Statistical CSI. Instantaneous CSI, also known as short-term CSI, provides information about the current state of the channel. In contrast, Statistical CSI offers a statistical characterization of the channel, including factors such as fading distribution, average channel gain, line-of-sight component, and spatial correlation. Both types of CSI can be utilized for transmission optimization, with their practical use depending on the speed at which the channel conditions change. In fast fading channels, Statistical CSI is more feasible, while in slow fading systems, Instantaneous CSI can be accurately estimated and used for transmission adaptation over a certain period. While CSI plays a valuable role in enhancing the performance of wireless communication systems, it is important to consider the challenges associated with obtaining CSI in different communication

systems. The rapid variations in the channel and the need for accurate estimation pose difficulties in acquiring reliable CSI. However, by addressing these challenges, the benefits of incorporating CSI into wireless communication systems can be realized [120].

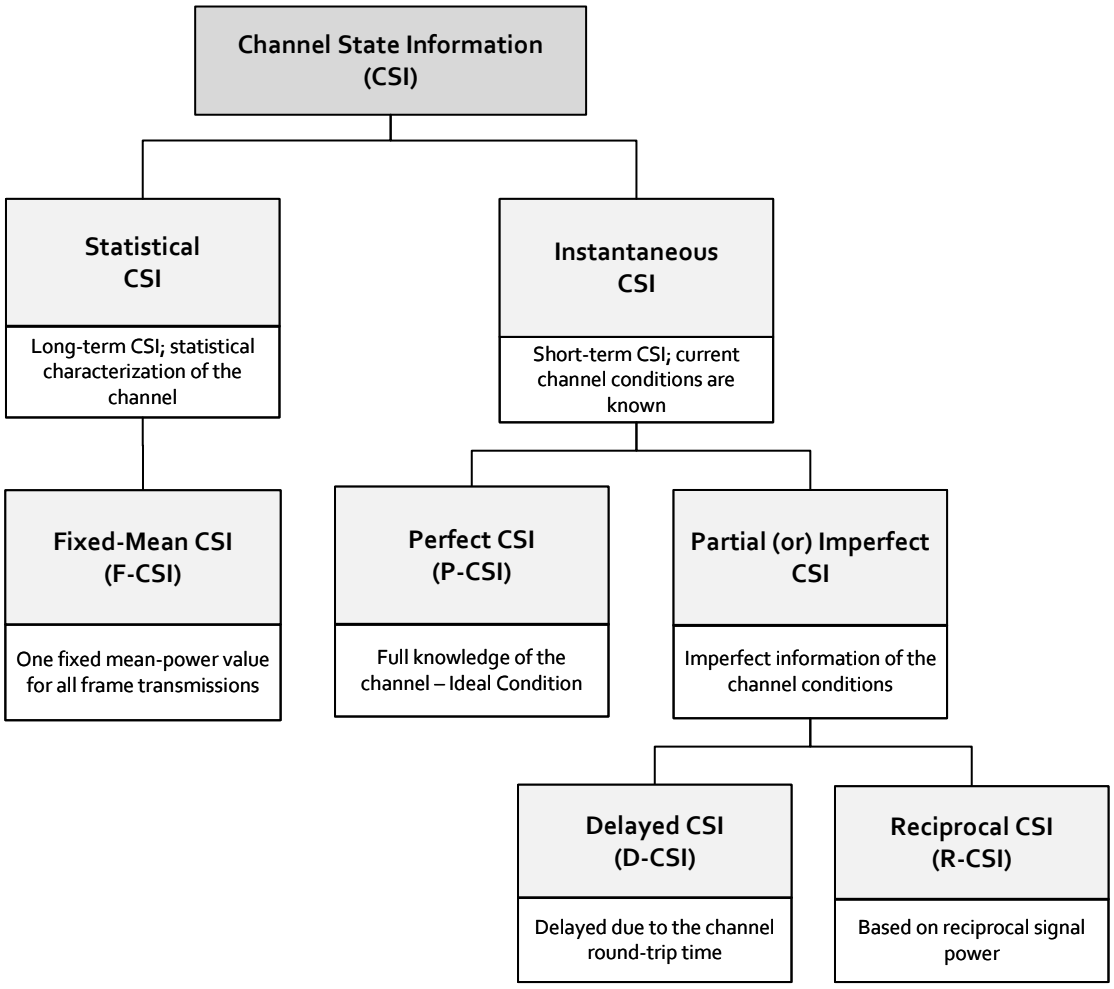

Figure 4.1.: CSI types: A comprehensive overview.

Instantaneous Channel State Information (CSI) is typically divided into two categories [120]: perfect CSI and partial or imperfect CSI. Perfect CSI, also known as P-CSI, embodies the transmitter's full awareness of the channel. However, achieving this comprehensive knowledge is often impractical in real-world scenarios. Without perfect CSI, research suggests that Hybrid Automatic Repeat Request (HARQ) schemes primarily rely on feedback from the receiver, typically in the form of acknowledgments (ACKs) or negative acknowledgments (NACKs) [121, 106, 122, 11]. To optimize the performance of HARQ, supplementary CSI can be supplied to the transmitter via feedback channels or by applying the channel reciprocity principle in Free Space Optics (FSO) systems [37, 40, 41]. However, it is noteworthy that the provisioning of CSI at the transmitter frequently encounters delays due to channel propagation time, which is usually in the scale of milliseconds and equivalent to the channel coherence time.

Channel State Information (CSI) Type	Delay with reference to Round-Trip Time (RTT)	Feedback from receiver	CSI value
Perfect CSI (P-CSI)	no delay	no	variable
Delayed CSI (D-CSI)	one RTT delay	yes	variable
Reciprocal CSI (R-CSI)	half-RTT delay	no	variable
Fixed-Mean CSI (F-CSI)	no delay	no	fixed

Table 4.1.: Overview of CSI classification in thesis scope.

This thesis presents a detailed examination of various Channel State Information (CSI) types in Table 4.1. The table outlines the different CSI types used in this research to optimize the Forward Error Correction (FEC) code-rate, along with the associated delay in relation to the round trip time (RTT), the requirement for receiver feedback, and whether the CSI value is variable or fixed. The first CSI type, **Perfect CSI (P-CSI)**, describes an ideal scenario where the transmitter has full knowledge of the channel without any RTT delay or feedback requirement. However, the P-CSI value is not static and fluctuates with changing channel conditions.

Delayed CSI (D-CSI) involves feedback information that is available at the transmitter after being delayed by one RTT between the receiver and transmitter, a strategy designed to enhance system performance. The one RTT delay occurs because the receiver decodes the information received from the transmitter and estimates the channel quality based on this reception. The estimated channel quality, known as delayed-CSI, is then sent back to the transmitter. This round-trip process, which includes the forward and backward propagation delays, results in the one RTT delay. For example, with a link distance of 300 km, the D-CSI information is accessible to the transmitter after a 2ms delay. Like P-CSI, D-CSI values also vary with channel conditions. The effectiveness of D-CSI is contingent upon the age of the CSI relative to the channel correlation time and the pace of FSO channel changes[123, 119].

Reciprocal CSI (R-CSI) relies on channel reciprocity and offers information about received power. It captures the correlation of signal power at both ends of a bidirectional laser propagation link in the turbulent atmosphere of Free Space Optics (FSO) channels [47, 41], as discussed in Section 2.10. R-CSI information is available at the transmitter after half a RTT, which corresponds to propagation time. The half RTT delay is a result of the transmitter sending information to the receiver and vice versa, taking into account the highly correlated/reciprocal nature of the channel. As a result, the information received at the transmitter side can already be regarded as the channel state, inherently has the channel quality. R-CSI's key advantage is its ability to obviate the need

for a reliable backward channel, as the transmitter maintains constant awareness of the R-CSI on the receiver's side. This simplification reduces the overhead and complexity by negating the need to establish and sustain a faultless backward channel. The benefits of R-CSI performance are more pronounced in adaptive code-rate HARQ protocols. Utilizing R-CSI enhances code rate adaptation and transmission efficiency, enabling adjustments based on channel conditions, which in turn influence both reliability and data rates. In challenging communication environments, especially when extended channel delays inhibit timely feedback, reciprocal CSI can substantially elevate HARQ performance.

Fixed-mean CSI (F-CSI) is a statistical CSI type that utilizes a constant CSI value for all frame transmissions, based on the mean received power [39]. F-CSI is the only type where the information remains steady and is instantly available at the transmitter, with no delay. More details about the novel approach for code-rate selection based on these CSI types can be found in Section 4.4.

Predicted CSI focuses on enhancing the quality and precision of imperfect instantaneous CSI through channel estimation in wireless communication systems [118, 124, 125]. Various channel estimation techniques, like maximum-likelihood (ML) estimation, least-square (LS) estimation, and minimum mean square error (MMSE) estimation, are used to obtain accurate predicted CSI [126, 127]. However, this thesis does not employ predicted CSI, but suggests it as a potential future enhancement.

4.3. HARQ Parameters and Assumptions

The HARQ simulations conducted in this thesis are predicated on a set of assumptions designed to simplify the analysis process and concentrate on the efficacy of the HARQ methods. These assumptions include a faultless feedback channel and a single propagation-time delay for the transmission of ACK and Channel State Information (CSI) data from the receiver to the transmitter, without any corruption or delay. It's generally accepted that undetected errors are nearly negligible, and successful decoding implies a minimal error probability. To facilitate a steady data flow, the transmitter is always ready to transmit available data. The transmission times for ACK and CSI frames are assumed to be 2.04 μs. With a net data rate of 1 Gbps, data transmission occurs in bursts of 2048 frames, each with a fixed codeword length of 255 bytes. The redundancy length (n-k) bytes is adjusted to modify the transmission rates.

These assumptions enable a detailed evaluation of HARQ schemes' performance and efficiency. However, it's crucial to recognize that these assumptions may not always reflect real-world conditions. For instance, a completely error-free feedback channel may not be feasible in practice, and the assumption of unlimited retransmissions might not align with systems with limited resources. Despite these limitations, the simulations offer crucial insights into the HARQ scheme's performance across various scenarios, guiding the development and implementation of HARQ for practical inter-High Altitude Platform (HAP) Free Space Optics (FSO) links.

The HARQ simulation parameters used in this thesis are detailed in Table 4.2. The performance evaluation of communication systems in inter-HAP FSO links heavily depends on these HARQ

simulation parameters. They play a significant role in shaping the comprehensive assessment of the system's effectiveness. These parameters cover essential assumptions and configurations that determine data transmission effectiveness and reliability in these specific situations. A detailed definition of simulation parameters is critical for a thorough understanding of how HARQ schemes operate.

Parameter	Value (Unit)	Symbol
Total encoded frame length	255 ($bytes$)	n_{total}
Total number of codeword symbols in the encoded block.	variable ($bytes$)	n_{packet}
Overhead	variable ($bytes$)	$n_{overhead}$
Window size	2048 ($frames$)	W_s
Net data rate	1 ($Gbps$)	R_{net}
Channel data rate	1.25 ($Gbps$)	R
Transmission time	2.04 (μs)	t_{packet}
Inter-HAP Link distance	150 - 900 (km)	L
Round trip time	1-6 (ms)	t_{RTT}

Table 4.2.: HARQ simulation: key parameter assumptions

4.4. Adaptive Code-Rate Selection

Selecting the appropriate code rate is vital for optimizing system throughput [79]. This thesis explores **eight** distinct FEC (Reed-Solomon (RS)) code rates, spanning from zero redundancy (meaning no RS coding) to the highest level of redundancy for packet encoding. The fluctuating CSI at the transmitter forms the basis for adaptive code-rate operation. The RS FEC code-rate (r) is adjusted in accordance with a look-up table illustrated in Table 4.3. This table correlates the CSI ($P_{rx}(t)$) with the code rate (r).

The block diagram illustrating the code-rate selection is shown in Figure 4.2, derived in terms of analytical calculations. The output of the inter-HAP FSO channel, which is the series of received power (often representing the mean received power), serves as the input to the RFE model in Section 2.9.1. This model is used to calculate the channel bit error ratio (referred to as bit error probability in this thesis), using Eq. (2.17). The resulting bit error probability enables the calculation of the channel's symbol error probability, according to Eq. (3.10), for a symbol size of 10

bits (m= 8bits + 2bits for 8b/10b channel coding). This calculated symbol error probability is then used as an input for the Reed-Solomon decoder to ascertain the Packet Error Probability (PEP), using Eq. (3.11). The resulting PEP aids in determining the transmission efficiency of the Selective Repeat ARQ scheme, utilizing Eq. (3.17).

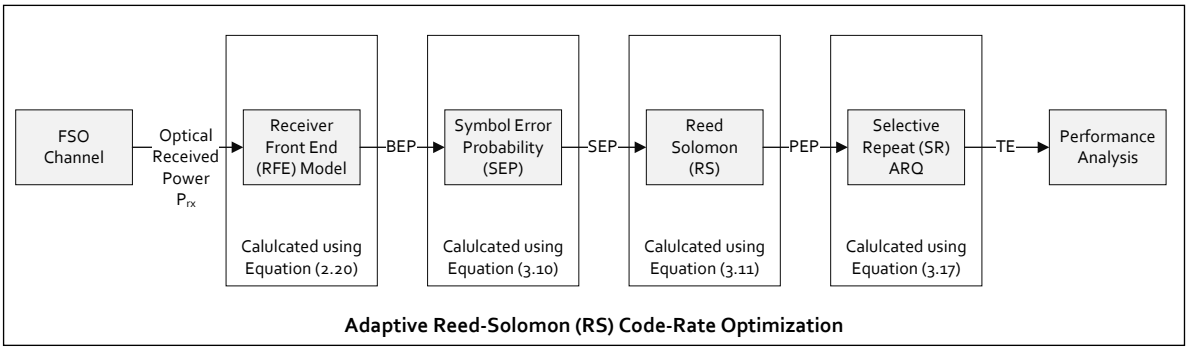

Figure 4.2.: Adaptive RS code-rate optimization: A block diagram view.

This efficiency calculation reveals the maximum achievable transmission efficiency for various Reed-Solomon FEC code rates, as illustrated in Figure 4.3. This figure presents a non-fading channel and the analytically computed transmission efficiency. Furthermore, the transmission efficiency for perfect CSI (P-CSI) can be perceived as the combined maximum efficiencies of all fixed code rates. The Figure 4.3 illustrates that the transmission efficiency attains a steady maximum value, even as the mean received power rises. This depicts the highest achievable transmission efficiency (TE) for this specific HARQ (RS + SR-ARQ) at a given RS code-rate. Therefore, the objective is to select the maximum range of mean received power for each CSI value, which corresponds to this peak achievable TE. This is portrayed in Figure 4.4, which presents the code-rate optimization plot. The plot reveals the maximum TE for each code-rate, based on specific selected mean receiver power values.

Referring to Figure 4.4, we select eight distinct mean receive powers, each corresponding to the maximum transmission efficiency (TE) for eight different code-rates. These power values are chosen based on the RFE model in Section 2.9.1, where the powers $PQ2 = 27.75nW$ and $PQ6 = 242.1nW$ denote the mean received powers necessary to achieve a bit error ratio (BER) of 10^{-2} and 10^{-6} respectively. Other power values are selected within this range to determine the maximum TE for each code-rate. It's clear that the peak TE is reached for each of these power values and then decreases. These eight power range values are subsequently selected for the CSIs, as shown in Table 4.3. The P_{rx} in nW column displays a range for this mean received power for its respective code rate (r).

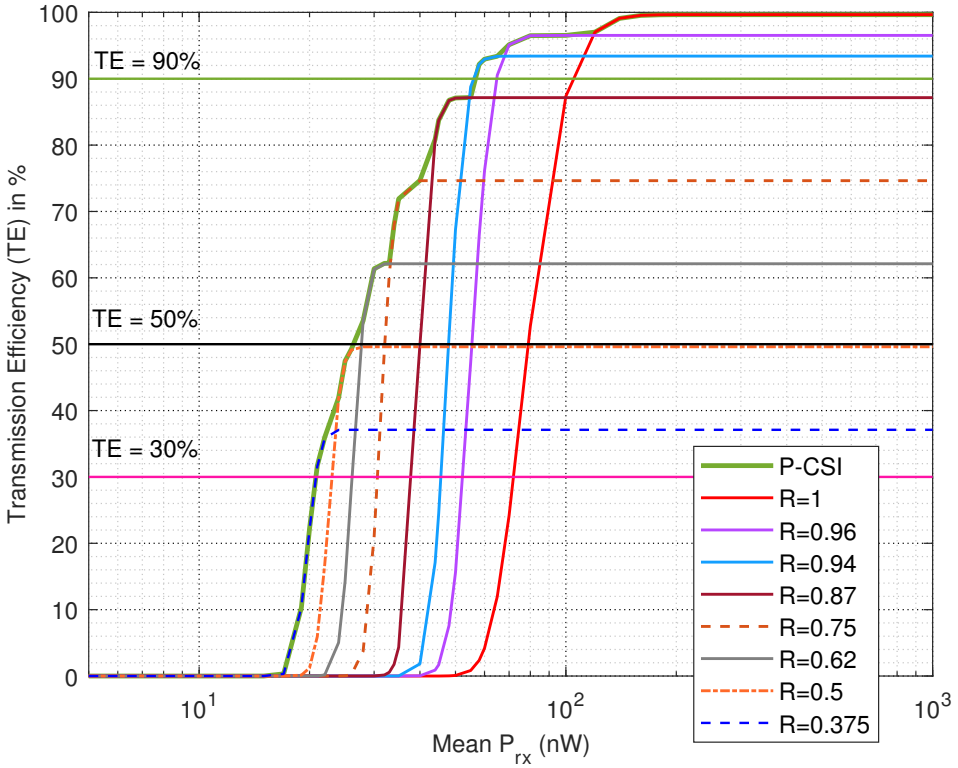

Figure 4.3.: Comparative analysis of adaptive rate HARQ performance in non-fading channels.

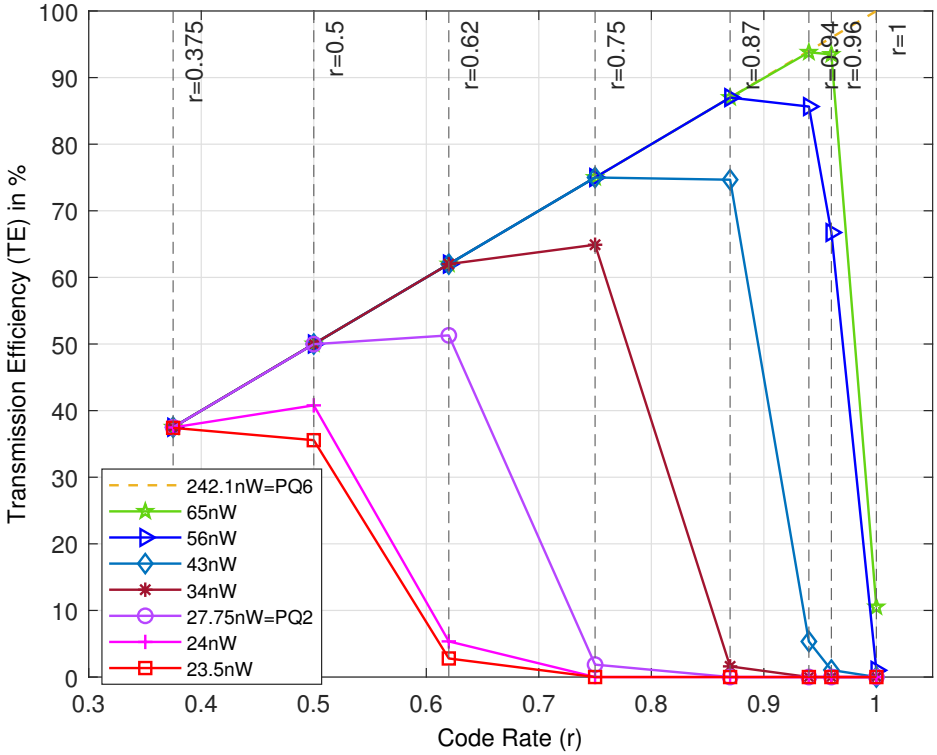

Figure 4.4.: Comparative analysis of Maximum TE for different RS code-rates based on mean received power.

We choose identical power range values for three distinct CSIs: P-CSI, D-CSI, and R-CSI, and a separate range for the F-CSI. It's crucial to highlight that the performance is influenced by the parameters of the CSIs outlined in Table 4.1, despite these three CSIs having the same power values. For F-CSI, the threshold values of P_{rx} in the look-up table were adjusted in simulations to account for the temporal behavior (short surges vs. extended fades) of the received power from the FSO channel. The RS FEC code-rate (r) is adjusted based on a look-up table, as depicted in Table 4.3, which converts the CSI ($P_{rx}(t)$) into the code rate (r). It's worth noting that the HARQ parameters employed for these simulations are derived from Table 4.2.

RS-FEC (n,k)	**RS-FEC Code Rate** (r)	$P_{rx}(nW)$ **for P-CSI, D-CSI and R-CSI**	$P_{rx}(nW)$ **for F-CSI**
(255,255)	1	117 to ∞	500 to ∞
(255,247)	0.96	65.5 to 117	300 to 500
(255,239)	0.94	56.5 to 65.5	117 to 300
(255,223)	0.87	43 to 56.5	65.5 to 117
(255,191)	0.75	33.6 to 43	56.5 to 65.5
(255,159)	0.62	27.6 to 33.6	27.6 to 56.5
(255,127)	0.5	23.65 to 27.6	23.65 to 27.6
(255,95)	0.375	0 to 23.65	0 to 23.65

Table 4.3.: Lookup table for RS code-rate selection based on various CSIs.

4.5. System Concept

Figure 4.5 illustrates the system design of an adaptive Hybrid Automatic Repeat Request (HARQ) with a flexible Reed-Solomon (RS) code rate. The transmitter comprises an RS-FEC encoder, ARQ control, a packet buffer for retransmissions, and an adaptive code rate controller. The receiver includes an RS decoder, an ARQ controller, a frame sink, and a channel-state estimator that operates on an inter-HAP fading channel, as detailed in Chapter 2. During simulations, it's assumed that errors occur solely in the forward channel, with the backward channel being error-free. This assumption facilitates a focused study of the adaptive HARQ's impact on the forward channel. The adaptive code rate controller adjusts the RS-FEC code rate based on the Channel State Information (CSI) for each transmission and retransmission. If an ACK is not received, the corresponding packet is retrieved from the buffer, encoded at the current code rate, and retransmitted.

Adaptive code-rate transmission, which is dependent on CSI, necessitates feedback from the receiver about the current channel conditions. This feedback is delivered through acknowledgment frames containing instantaneous power information, which allows the transmitter to adjust the

Forward Error Correction (FEC) code rate for the subsequent frame transmission. The proposed system, as shown in Figure 4.5, includes a mechanism to alter the Reed-Solomon (RS) FEC code rate based on the CSI communicated to the transmitter. As explored in Section 4.2, this thesis examines various CSI modes, such as perfect CSI (P-CSI), reciprocal CSI (R-CSI), delayed CSI (D-CSI), and fixed mean CSI (F-CSI). These modes represent different strategies for channel state estimation and transmission to the transmitter. The primary objective is to evaluate the performance of the adaptive HARQ scheme under diverse channel conditions, offering insights into the efficacy and efficiency of adapting the code rate based on the received CSI, thereby optimizing the transmission process in various channel environments.

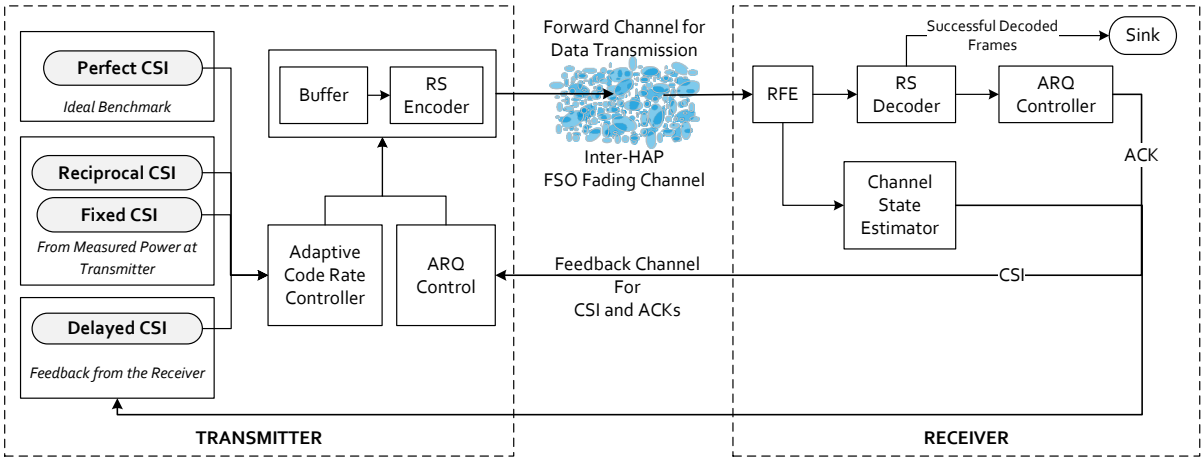

Figure 4.5.: HARQ system design: Utilizing CSI modes for adaptive reed-solomon code rate selection.

In conclusion, the proposed system achieves adaptive code-rate transmission using CSI, enabling the transmitter to dynamically adapt to channel conditions by selecting the optimal FEC code rate for each frame transmission. The various CSI modes are used to determine the optimal code rate, and frames are transmitted using the selected code rate over the fading FSO channel. The ARQ control block manages retransmissions, and the adaptive rate controller module modifies the RS encoding based on the received CSI to ensure error-free data transmission.

4.6. Chapter Summary

In this chapter, an innovative approach has been unveiled, which capitalizes on various types of Channel State Information (CSI) to adjust the Reed-Solomon Forward Error Correction (FEC) code-rate. This adjustment significantly improves the performance analysis of the Hybrid Automatic Repeat Request (HARQ) schemes. Four distinct types of CSI, specifically perfect CSI (P-CSI), reciprocal CSI (R-CSI), delayed CSI (D-CSI), and fixed mean CSI (F-CSI), have been selected for this thesis. With these CSIs as the basis, adaptation of the Reed-Solomon (RS) FEC code-rate was achieved, in alignment with the Selective Repeat ARQ. The Reed-Solomon FEC

code-rate was chosen, influenced by the types of CSI. A unique range of mean power values was associated with each CSI value. Through rigorous analysis of RS code rates, along with Selective Repeat ARQ and RFE modeling, the optimal power selection was identified. Finally, a detailed explanation of this approach's system concept was provided. The upcoming Chapter 5 will provide an in-depth presentation of the simulation model for both the channel and the HARQ schemes.

5 Simulation Model

This chapter presents the simulation environment utilized for generating received power vectors for inter-HAP FSO links, as well as for conducting event-based HARQ simulations. The simulation approach, which employs PILab (Propagation and Imaging Lab) [128, 129] and PVGeT (Power Vector Generation Tool) [38] to simulate power vectors in both conventional and reciprocal channels, is elaborated in Section 5.1.1 and Section 5.1.2. Moreover, Section 5.2 offers a more detailed discussion on the event-based simulation environment and its principles that facilitate the simulation of the SR HARQ technique. Lastly, the integration of the channel and ARQ simulations is outlined in Section 5.3, while Section 5.4 provides a summary of the chapter.

5.1. FSO Channel Simulation

The simulation model is essential for evaluating and optimizing the performance of inter-HAP FSO communication systems. This section details the development of a MATLAB-based simulation model using PVGeT (Power Vector Generation Tool) and PILab (Propagation and Imaging Lab), which generates realistic power vectors for both conventional and reciprocal FSO channels. By integrating these tools, we can accurately simulate FSO communication scenarios. This model is valuable for assessing inter-HAP FSO link performance, analyzing various parameters, exploring Hybrid Automatic Repeat Request (HARQ) techniques, and improving link reliability and efficiency. In Chapter 6, we will further discuss the application of this simulation model and analyze the results.

5.1.1. PILab Simulation

The Propagation and Imaging Lab (PILab) is a software tool that utilizes the Matlab programming language to simulate scenarios of FSO communication. These simulations incorporate atmospheric propagation models [128, 129]. The study utilizes phase screens that are laterally shifted based on the orthogonal wind to model the spatial and temporal dynamics of atmospheric turbulence, resulting in temporal fluctuations in the received power signals. This section focuses on simulating inter-HAP FSO channels with reciprocal characteristics, as well as incorporating wind-induced beam displacement by shifting each phase screen by a predetermined number of pixels (1mm each).

$$N_x = \frac{d * v_x}{c * \delta_x}, N_y = \frac{d * v_y}{c * \delta_y} \tag{5.1}$$

N_x and N_y	number of pixels to shift along the directions x and y
v_x and v_y	wind speeds projected to the directions x and y
δ_x and δ_y	resolutions along x and y of the image
c	speed of light in the vacuum (m/s)
d	distance of a phase screen from the transmitter (m)

To simulate reciprocal channels, a two-step process was employed:

1. In the first step, a reciprocal channel was created by using the same phase screens for both the forward and return paths, ensuring that the order is reversed. This means that the first phase screen used for the forward direction becomes the last one for the return path, the second phase screen used for the forward direction becomes the second-to-last for the backward direction, and so on for all phase screens.

2. In the second step, the phase screens of the return path were flipped to simulate each transmitter's perspective of the scene. Additionally, the simulation accounted for wind-induced

phase screen shifting, which was opposite for the backward path compared to the forward direction.

The objective of the simulation is to replicate the same phase screens for the return channel, keeping the propagating 2D array unchanged. However, as the beam propagates, its size may exceed that of the generated phase screens. This can lead to self-interference patterns and image aliasing issues as energy reflects from the edges. To mitigate this, a damper is implemented to prevent the diffracted field from extending beyond the phase screens. Furthermore, a Gaussian beam of the appropriate size is used as the field source at the transmitter plane. This is followed by a lens element in the simulator to create a non-collimated beam that mimics the diffraction behavior of a spherical wave. This method is based on Martin and Flatté's point source simulation technique, as described in [130].

5.1.1.1. Conventional Channel Simulation

This section presents the fading vectors simulated using PILab for a non-reciprocal conventional scenario. The simulations utilized precise parameters, including an 85µrad divergence angle, a wavelength of 1550nm, and a receiver telescope diameter (D_{rx}) of 15cm. These carefully selected parameters were based on the link budget shown in Table 2.2. PILab was employed to accurately emulate the impact of atmospheric turbulence on the inter-HAP FSO communication channel.

Two distinct scenarios, labeled A and B, were examined in the study, with distances of 300 km and 600 km, respectively. In scenario A, the HAP heights (H_{hap}) were set at 19.76 km, while in scenario B, the platforms were positioned at 25.04 km. Both scenarios had an identical graze height (G_h) of 18 km. By using these scenarios, we were able to analyze the FSO communication system's performance under varying atmospheric conditions. Through simulations that manipulated different distances and H_{hap} heights, we gained valuable insights into the effects of these parameters on the fading characteristics of the conventional channel. The analysis considered both the combined effect of atmospheric conditions and the channel's temporal characteristics. Table 5.1 provides comprehensive information about the investigated scenarios, including specific parameters and conditions.

Scenario	**Link Distance L (km)**	**HAP Height H_{hap} (km)**	**Graze Height G_h (km)**	**Orthogonal Wind Speed v (m/s)**	**Channel Correlation Time τ (ms)**	**Power Scintillation Index PSI (unitless)**
A.1	300	19.76	18	10	10.95	0.42
A.2				50	2.7	0.39
B.1	600	25.04		10	13.75	0.87
B.2				50	2.75	0.97

Table 5.1.: Inter-HAP scenarios: Conventional channel simulations using PILab.

Note: The slight variations in PSI values (0.42/0.39 and 0.87/0.97) for the same link distances are statistical variations arising from differences in the length of received power vectors. However, the fading strengths remain similar.

Scenarios A and B, which are further subdivided into A.1, A.2, B.1, and B.2 as shown in Table 5.1, are analyzed based on the stratospheric orthogonal wind speed (v) that influences the channel's correlation time (τ). These wind speeds fall within the expected range according to previous research. The scenarios consider the combined effects of atmospheric turbulence and different PSI strengths (ranging from 0.4 to 0.9) with varying channel correlation lengths resulting from orthogonal wind speeds. The methodology described in Section 2.4 is used to calculate the optical turbulence along the inter-HAP link path for scenarios A (300 km) and B (600 km).

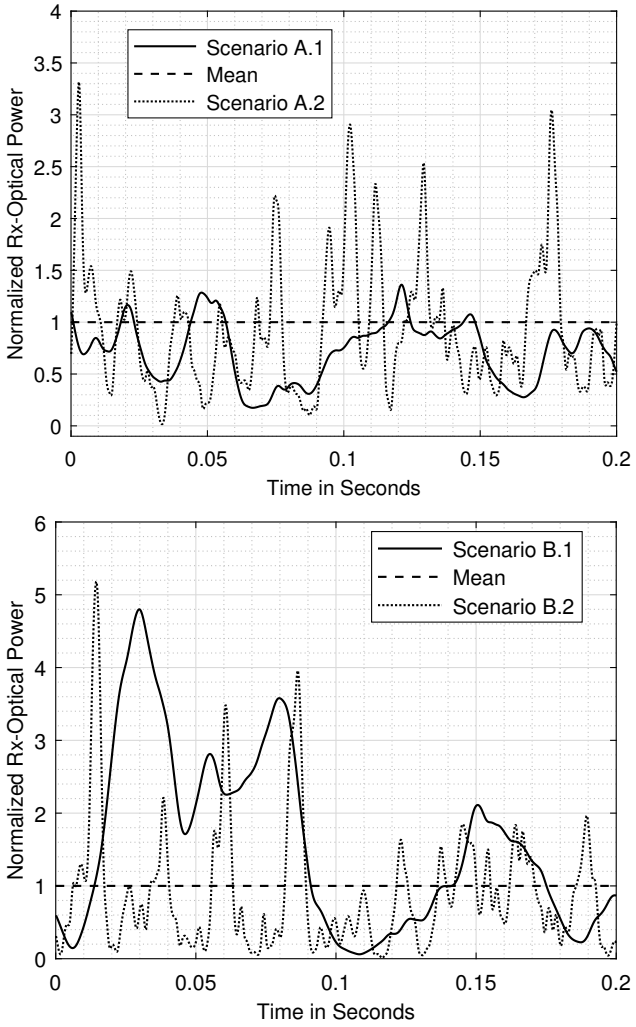

(a) Solid line represents $\sigma_P^2 = 0.42$ and $\tau_{A.1} = 10.95ms$ and dotted line represents $\sigma_P^2 = 0.39$ and $\tau_{A.2} = 2.7ms$.

(b) Solid line represents $\sigma_P^2 = 0.87$ and $\tau_{B.1} = 13.75ms$ and dotted line represents $\sigma_P^2 = 0.97$ and $\tau_{B.2} = 2.75ms$.

Figure 5.1.: Time series representation of scenario A and B simulated vectors in PILab for a conventional channel.

Figures (a) and (b) in Figure 5.1 display simulated fading vectors generated using PILab, showcasing the temporal behavior and fading characteristics of the inter-HAP scenarios. Each scenario (A and B) considers two orthogonal wind speeds (10 m/s and 50 m/s), leading to varying correlation times for the same fading channel. These simulations offer valuable insights into the impact of atmospheric turbulence and wind speeds on the fading behavior of the FSO communication system in inter-HAP scenarios.

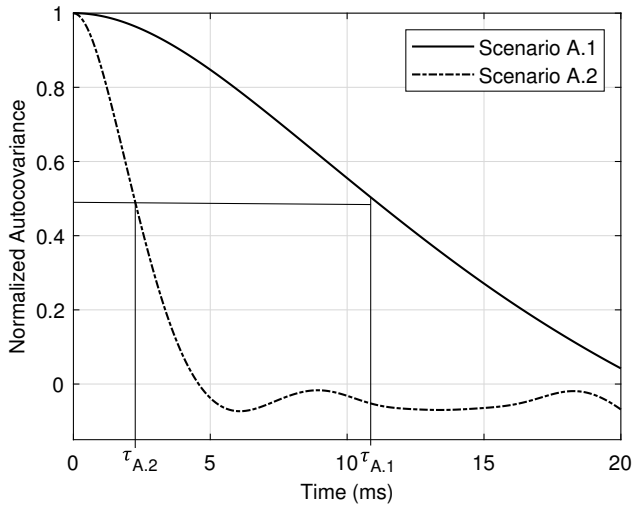

(a) Scenario A.1 and Scenario A.2 with correlation time $\tau_{A.1} = 10.95ms$ and $\tau_{A.2} = 2.7ms$ respectively.

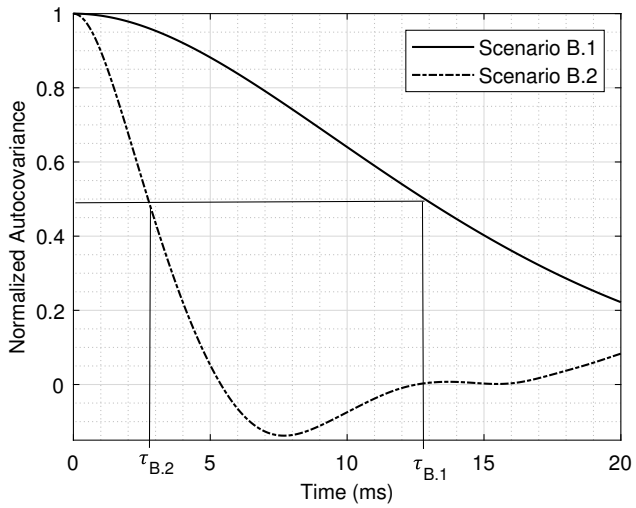

(b) Scenario B.1 and Scenario B.2 with correlation time $\tau_{B.1} = 13.75ms$ and $\tau_{B.2} = 2.75ms$ respectively.

Figure 5.2.: Autocovariance representation of scenario A and B simulated vectors in PILab for a conventional channel.

Figures (a) and (b) in Figure 5.2 depict the autocovariance of the simulated vectors generated by PILab. The correlation time is calculated using the normalized autocovariance at the Half Width Half Maximum (HWHM). The evaluation of HARQ with CSI performance is conducted using the simulated vectors discussed in Section 6.3.

5.1.1.2. Reciprocal Channel Simulation

The fading vectors simulated in PILab for a reciprocal scenario are presented in the following section. Table 2.1 provides a summary of different bi-directional inter-HAP scenarios, including eight link distances (L) and HAPs at various heights (H_{hap}). In all scenarios, a single graze height (G_h) was assumed to represent the minimum height of the optical link above Earth's surface, where turbulence is most significant. By running scenarios with different HAP heights and link distances, the impact of various atmospheric and geometric parameters was studied. The table also includes the propagation delay, t_{TOF}, which represents the time-of-flight (ToF) for different link distances.

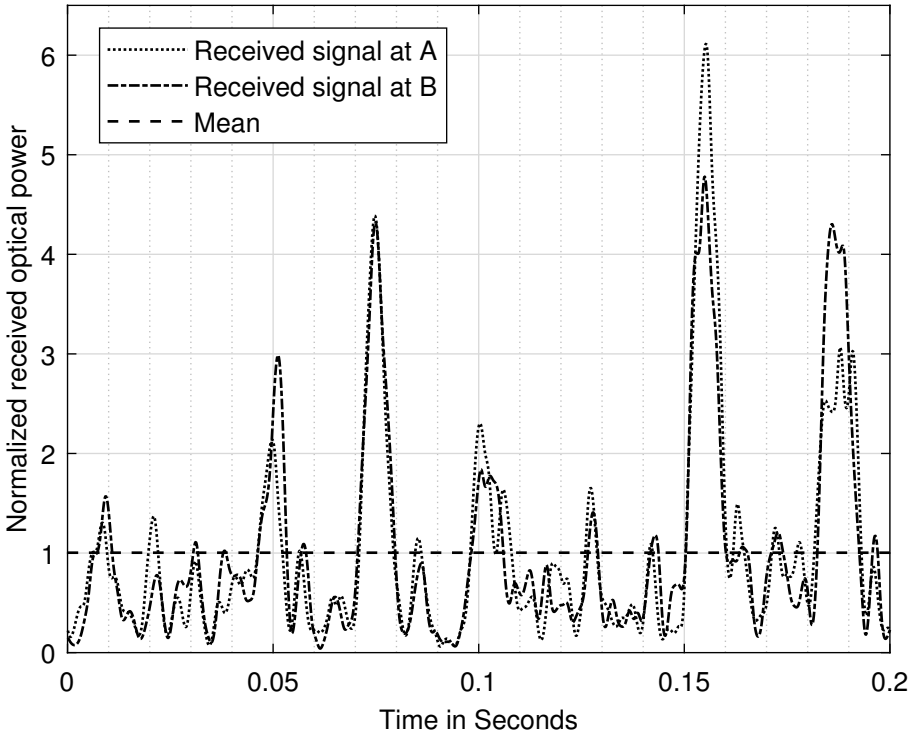

Figure 5.3.: Timeseries of first 200 ms of simulated normalized received power vectors.

Note: Parameters of the PILab simulated vector based on the scenario outlined in Table 2.1: $L = 900km$ for $D_{rx} = 20cm$. $CCF = 0.924$, $NMSE = 0.18$, $PSI - A = 0.981$, $PSI - B = 1.126$, $HWHMacov - A = 2.95ms$, $HWHMacov - B = 2.91ms$.

The received optical powers at terminals A and B, corresponding to the optical powers received at HAPs A and B, are shown in Figure 5.3. These measurements were taken using a receiver aperture with a diameter of $D_{rx} = 20cm$. Figure 5.4 compares the estimated probability density function (PDF) based on the lognormal distribution to the simulation results. For PSI values around 1, there is acceptable agreement between the analytical and simulated results. However, due to the limited continuous vector length caused by the finite size of the phase screens shifted by the orthogonal wind speed, the simulated values' PDF may contain outliers.

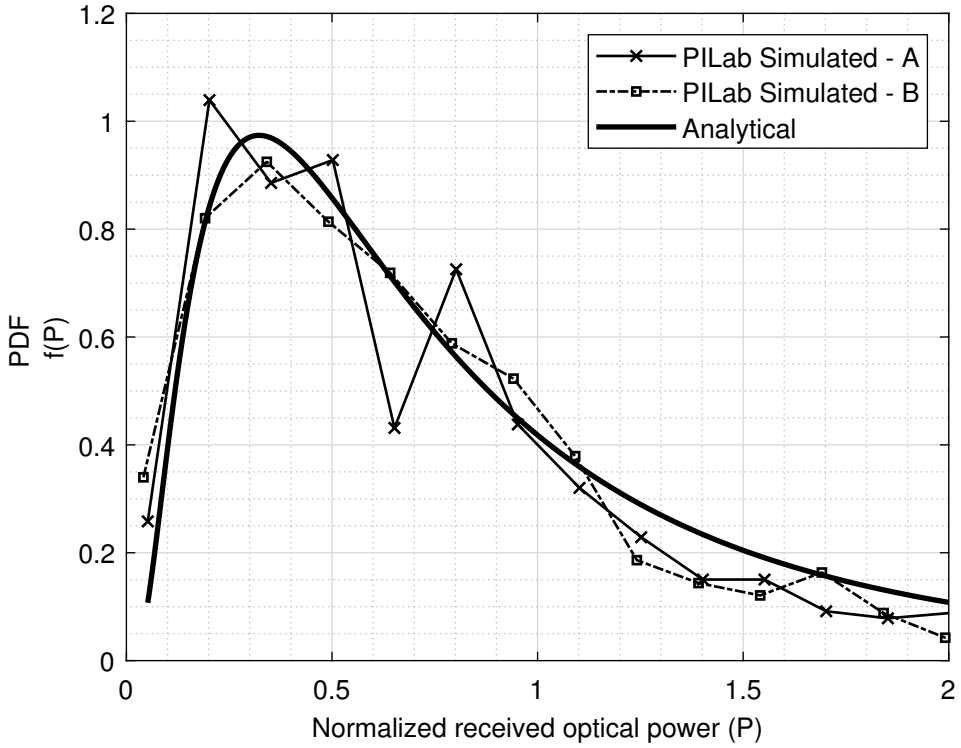

Figure 5.4.: The PDFs of the received powers from one PILab simulation run and an analytical (lognormal) distribution are compared.

Figure 5.5 (a) displays different scintillation indices for various link distances and an orthogonal wind speed of 50 m/s. The Intensity Scintillation Index (ISI) represents a point receiver. The analyzed β_0^2 indicates an increase in Rytov variance along the link distance, along with the simulated ISI and PSI (for $D_{rx} = 20cm$). The scintillation index generally increases with the link distance (L) and turbulence strength, as shown in Figure 5.5 (a). Moreover, there are noticeable differences in scintillation index values between ISI and PSI.

Figure 5.5 (b) illustrates the correlation between the width of intensity speckles and the link distance. In the context of a collimated beam, the speckle width (ρ_c) is directly proportional to the dimension of the initial Fresnel zone, expressed as $\rho_c \sim \sqrt{\lambda L}$. This value ($\rho_c$) also represents the maximum extent of the receiver aperture that can function as a point receiver. Notably, when the aperture size exceeds ρ_c, aperture averaging occurs, resulting in a reduction in scintillation effects. This concept is discussed in [4]. The graph also demonstrates the analytical (ρ_c) and simulated (ρ_i) increase in speckle size for different link distances. The simulation and analytical results support the hypothesis that increasing link distance is associated with larger speckle dimensions.

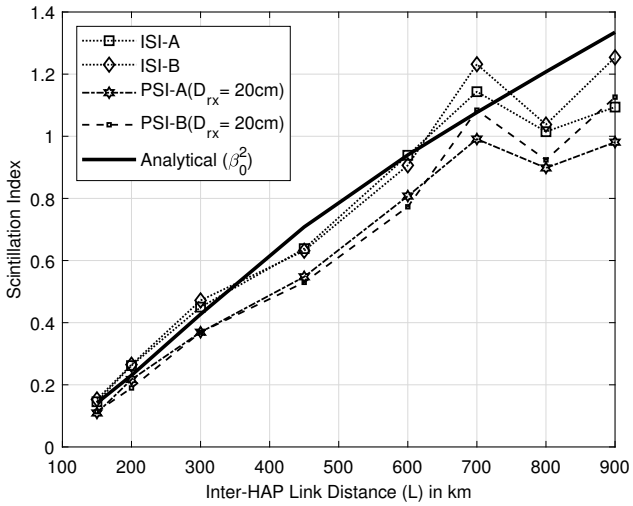

(a) Summary of scintillation indices for different inter-HAP link distances for orthogonal wind speed (v) of 50 m/s.

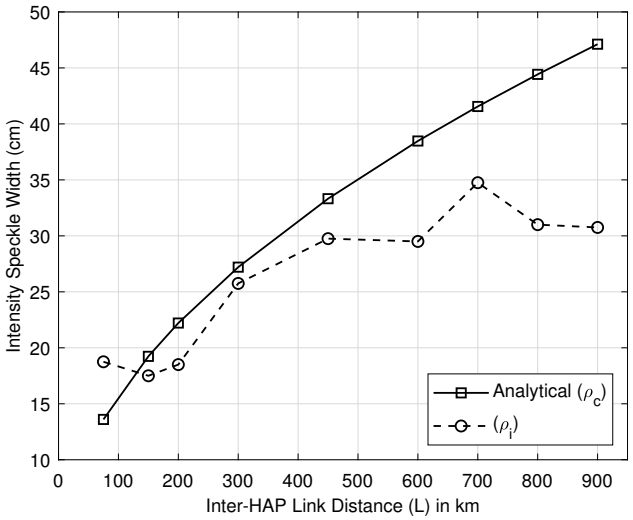

(b) Comparison of intensity speckle width (simulated and analytical) for different inter-HAP link distances.

Figure 5.5.: ISI and intensity speckle comparison of PILab-based simulations of reciprocal scenarios.

Figure 5.6 demonstrates the use of Correlation Coefficient (CCF) and Normalized Mean Squared Error (NMSE) as performance metrics to evaluate reciprocity in inter-HAP FSO links. The figure presents results for two orthogonal wind speeds, 10 m/s and 50 m/s, across different inter-HAP link distances. Both CCF and NMSE are utilized to assess reciprocity quality, and they exhibit an interesting trend where NMSE increases with longer link distances, indicating a decline in reciprocity.

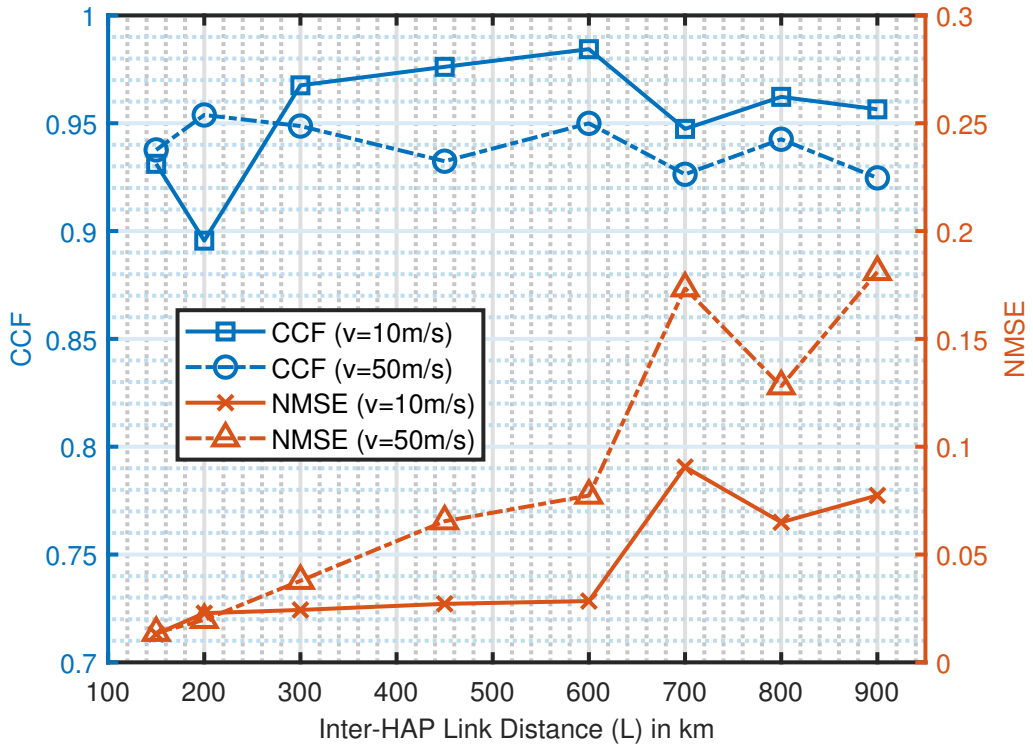

Figure 5.6.: Variation of CCF and NMSE with orthogonal wind speed and link distance.

.

While CCF shows minor variations along the link distance (L), it is expected that a more significant reduction in reciprocity, resulting from changes in the Index of Refraction (IRT) structure during extended Time of Flight (ToF), will be observed for longer distances. The increase in NMSE with increasing link distance suggests a larger absolute power divergence between the two directions. Changes in the IRT structure can also contribute to inadequate reciprocity in channel state information. Therefore, it is crucial to combine both CCF and NMSE to achieve a comprehensive assessment of reciprocity in inter-HAP FSO links.

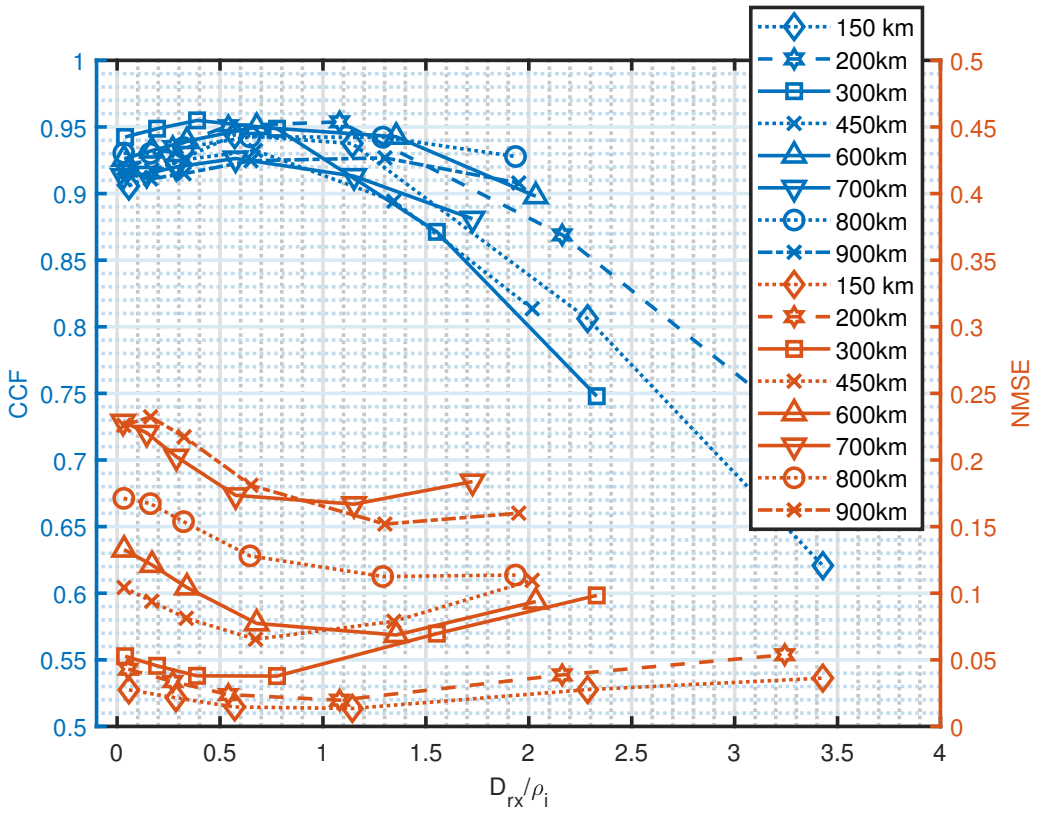

Figure 5.7.: Variation of CCF and NMSE with (D_{rx}/ρ_i) for different link distances.

Note: Receiver aperture diameter (D_{rx}) normalized to simulated speckle size (ρ_i) is displayed on the horizontal axis. An orthogonal wind speed of 50 m/s is considered.

Figure 5.7 depicts the relationship between CCF and NMSE at various inter-HAP link distances. The plot in Figure 5.7 shows them plotted against the parameter D_{rx}/ρ_i. As D_{rx}/ρ_i increases, the reciprocal quality declines, evident from the increased NMSE and lower CCF. The lower CCF is a result of the smaller receiver aperture's heightened sensitivity to orthogonal wind speed at $D_{rx}/\rho_i = 0$. Due to aperture averaging effects, where a larger speckle size corresponds to a longer link distance, the CCF decreases as D_{rx}/ρ_i increases. Conversely, the rising NMSE with increasing D_{rx}/ρ_i indicates a decrease in reciprocity quality caused by differences in absolute received power levels between the HAPs. Furthermore, the values of CCF and NMSE confirm that reciprocity quality decreases with increasing link distance (L), which is associated with structural changes in Index of Refraction (IRT) during prolonged Time of Flights (ToFs). Therefore, it is important to consider both CCF and NMSE values when evaluating the channel reciprocity quality.

Section 6.3 focuses on evaluating and analyzing the performance of HARQ schemes for power vectors generated by PILab in inter-HAP scenarios. The evaluation aims to assess the effectiveness and efficiency of HARQ with adaptive code-rate based on channel state information. Reciprocity observed in the reciprocal channel simulations is applied in the form of reciprocal CSI.

5.1.2. PVGeT Simulation

PVGeT (Power Vector Generation Tool) is a simulation program that accurately models atmospheric turbulence and pointing jitter in free-space optical communication systems [38]. It generates lognormal and beta-distributed time series of received power based on measured or analytical parameters. The PVGeT simulation methodology can simulate various atmospherically affected link scenarios, including optical satellite uplinks and downlinks, aircraft downlinks, ground-to-ground links, and optical connections between high-altitude platforms.

In this thesis, PVGeT is used to generate power vectors for inter-HAP optical links and assess the performance of hybrid ARQ schemes. In addition to PILab simulations, PVGeT was utilized to simulate the effects of beta-distributed pointing errors, in addition to the lognormal-distributed atmospheric turbulence effects. Furthermore, PVGeT was exclusively employed for simulating the conventional channel, while the PILab tool simulated both the conventional and reciprocal channels. The accuracy of the simulation model can be validated, and fading mitigation strategies can be evaluated by comparing the simulated power vectors with actual measurement results [38]. This section also presents a conventional channel scenario where PVGeT generates power vectors for inter-HAP optical links that combine atmospheric turbulence and static pointing jitter.

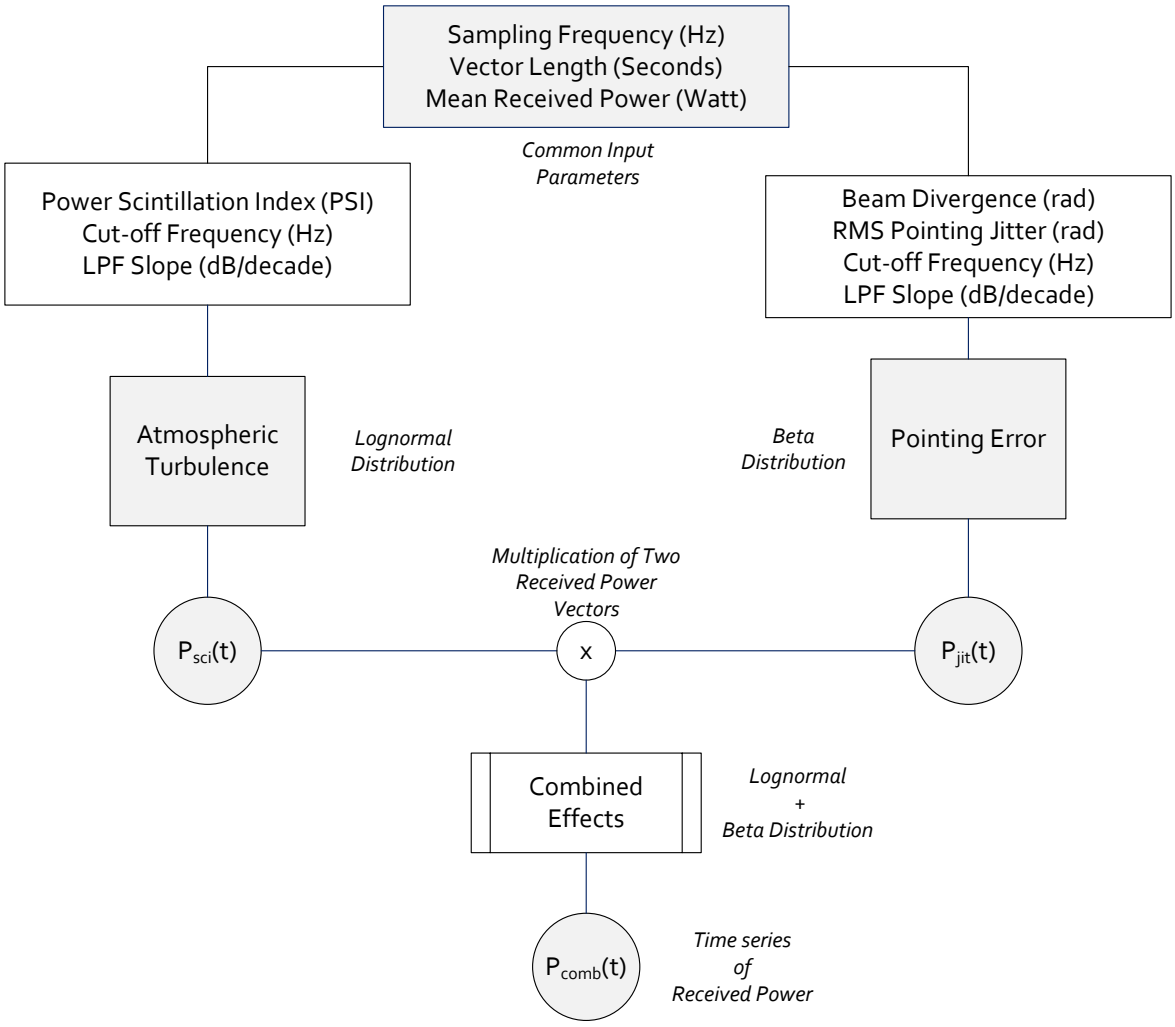

Figure 5.8.: Flow Diagram of PVGeT.

PVGeT employs a simulation algorithm that incorporates Gujar's method [131] to generate random signals with predetermined probability density and power density spectra. The algorithm consists of several stages aimed at manipulating the spectral properties and achieving the desired skewness of the signals. Figure 5.8 illustrates the flow diagram of the PVGeT algorithm. The lognormal scintillation vector is created by generating random values from a normal distribution with a mean of zero and a predetermined standard deviation. These values are then filtered using a Butterworth low-pass filter with a specific cutoff frequency and slope. The resulting variable is scaled to match the intended mean and standard deviation based on the desired power scintillation index. This procedure generates a vector of received power with a lognormal distribution.

At the receiver, a Gaussian beam configuration is assumed, along with Gaussian-distributed angular jitter in both orthogonal beam angles, to generate the pointing jitter fading vector. To represent the angles of the pointing jitter, a pair of uncorrelated Gaussian-distributed random variables is generated first. These variables are then subjected to Butterworth low-pass filters with predetermined cutoff frequencies and slopes. The resulting variables are re-normalized before being con-

verted from orthogonal-angular to radial Rayleigh distribution, yielding the radial-angular beam wander error. The received power vector is calculated by combining fading caused by pointing errors, which is further influenced by the Gaussian beam shape and radial pointing error. In simulated FSO links, the algorithm integrates autonomous random variables for lognormal scintillation and beta-distributed pointing-jitter fading to produce the combined received power vector that accounts for atmospheric turbulence and pointing jitter. PvGeT applications and detailed analysis are explained and published in [38].

5.1.2.1. Conventional Channel Simulation

In this section, we introduce the fading vectors produced by PvGeT for a conventional (non-reciprocal) scenario. These fading vectors were simulated to represent inter-HAP FSO link scenarios. The inter-HAP bi-directional channel was set to a link distance of 400 km, with both HAPs positioned at an altitude (H_{hap}) of 22 km, resulting in a graze height (G_h) of 18.87 km. Based on the two C_n^2-profiles discussed in Section 2.4, we defined two scenarios: the Best and Worst case. The intensity of irradiance fluctuations was measured using the Power Scintillation Index (PSI). Additional details on the defined scenarios can be found in Table 5.2.

C_n^2 **Case**	**Link Distance** L **(km)**	**HAP Height** H_{hap} **(km)**	**Graze Height** G_h **(km)**	**Power Scintillation Index (PSI)**
Best	400	22	18.87	0.008
Worst				0.65

Table 5.2.: Inter-HAP scenarios: Conventional channel simulations using PvGeT.

The PvGeT methodology was employed to accurately simulate the impact of atmospheric turbulence and pointing errors on the inter-HAP channel. The resulting time series of received power exhibits scintillation characteristics, with fades and surges reflecting the turbulent atmosphere's effects. The probability density function (PDF) of the optical receiver power was generated using a log-normal distribution for moderate turbulence, as depicted in Figure 5.9. This PDF offers valuable insights into the behavior of the inter-HAP channel under different turbulence and pointing error conditions. By analyzing the PDF, we can understand the frequency of power levels, which helps us assess the likelihood of various bit error probabilities (BEPs). This understanding aids in choosing suitable HARQ schemes and parameters for different scenarios. Section 6.2 explores the evaluation and analysis of Hybrid Automatic Repeat Request (HARQ) protocols for the power vectors generated by PvGeT in the inter-HAP scenario. The evaluation aims to determine the effectiveness and efficiency of HARQ in mitigating errors and optimizing data transmission reliability in the inter-HAP communication system. The efficiency of HARQ schemes is assessed in this thesis by evaluating the performance of inter-HAP FSO communication using conventional (non-reciprocal) links with PvGeT-generated power vectors for various scenarios.

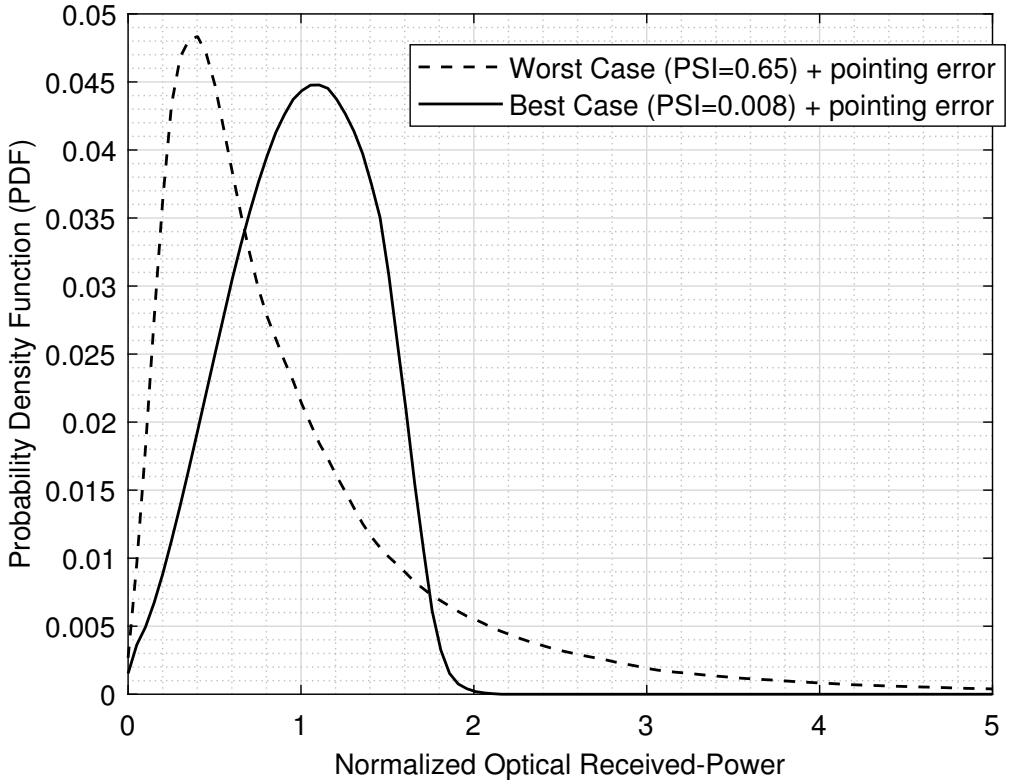

Figure 5.9.: PDF analysis of optical power received in inter-HAP scenarios generated by PvGeT.

Note: Best Case Scenario: PSI is 0.008, and in the Worst Case, PSI is 0.65. Both situations account for the impacts of pointing error ($\sigma_{rms} = 20\mu rad$) as explained in Section 2.8.

5.2. SR-ARQ Simulation Concept

OMNeT++ (Objective Modular Network Testbed in C++) is a network simulation framework that allows for flexible and efficient modeling of complex networks. It employs a component model architecture, enabling developers to create models using high-level languages NED (NEtwork Description). C++ modules are written and assembled into complex parts and models [132, 133]. Besides communication networks, OMNeT++ finds wide application in various fields. It offers simplicity, strong GUI support, and serves as a valuable resource for researchers and developers. In this thesis, OMNeT++ is used to simulate error control techniques, such as ARQ and HARQ, and evaluate their effectiveness in mitigating inter-HAP FSO channel impairments. The simulation incorporates the concept of adaptive code-rate FEC HARQ system, which adjusts the FEC code rate based on channel state information.

In order to conduct comprehensive investigations, we developed an SR-ARQ mechanism from scratch utilizing the event-based OMNET++ simulation library environment. We then assessed the transmission efficiency resulting from the ARQ implementation. This section includes detailed flow diagrams of this process. Here, hap1 signifies the transmitter, while hap2 denotes the receiver. Both hap1 and hap2 maintain a bi-directional link with an error-free back channel. As outlined in

previous discussions, the PEP serves as the channel input. The SR-ARQ, along with code-rate adaptation, operates with various CSI types based on these PEP inputs. We present the simulations using the SDL (Specification and Description Language), a graphical language that's beneficial for describing social simulation models, from Figure 5.10 to Figure 5.14. The terms associated with the SDL are presented as follows:

ACK	Acknowledgment
ASN	Acknowledgement sequence number
B	Window base
N	Window size
i	For loop variable
RSN	Received packet sequence number
SN	Sequence number
T_{t_0}	Timeout
T_s	Transmission time
CSI	Channel state information

In Figure 5.10, the initiation phase of hap1 is shown, occurring only once at the start. In this phase, base and sequence numbers for the initial frame are assigned. When the hap event begins, the first frame is generated and sent to hap2, with a duplicate saved for potential re-transmission. A sequence number timer is initiated for each frame transmission, and this process repeats for each transmission. This phase serves as the starting point and occurs once before moving to the next stages: transmit, blocked, or re-transmit.

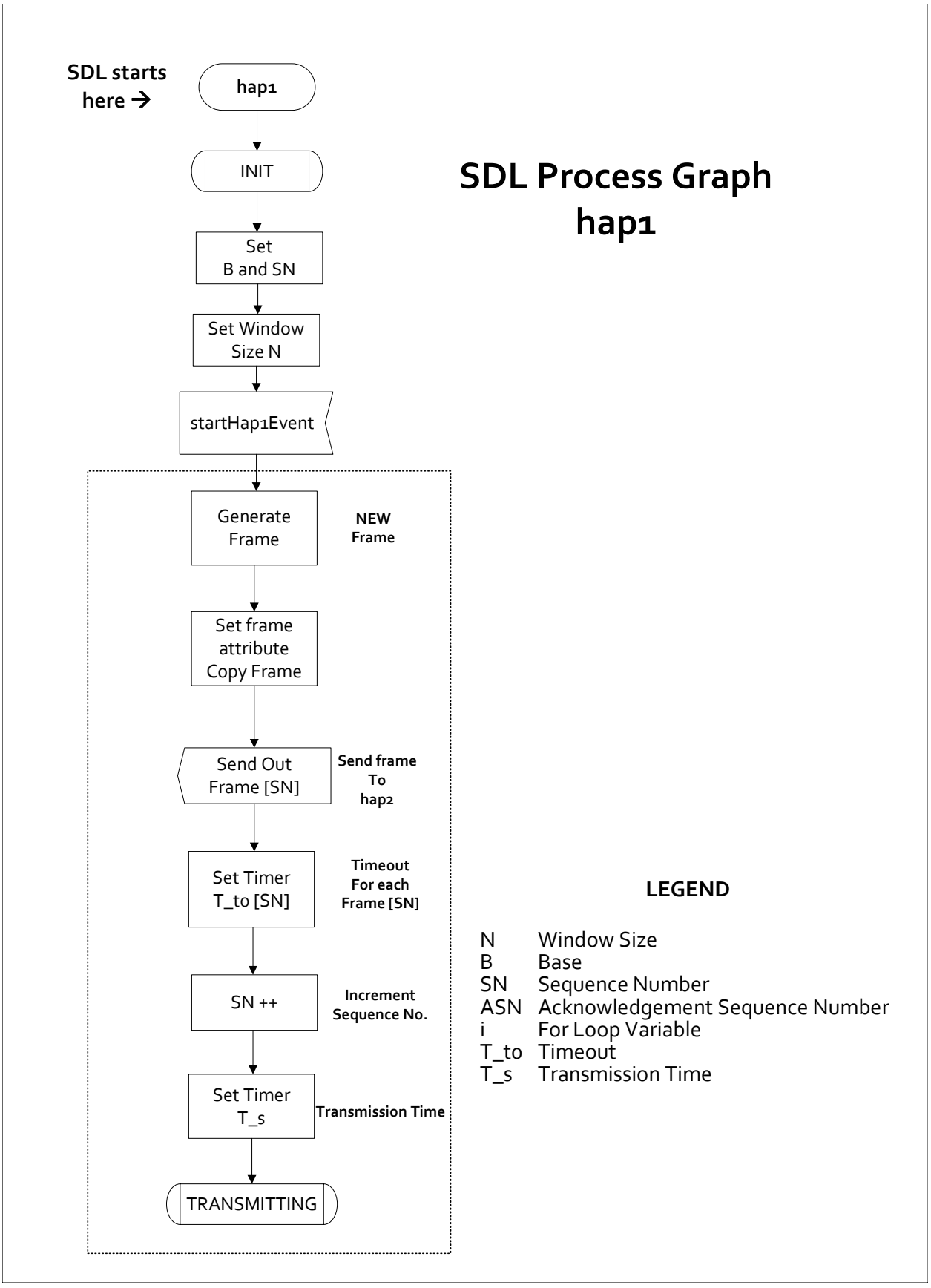

Figure 5.10.: SDL: hap1 start stage

The transmission stage, as illustrated in Figure 5.11, encompasses three distinct events: transmission, acknowledgment reception, and timeout expiration. A new frame is generated every 2.04 microseconds, consistent with the assumptions in Section 4.3. A replica is created, sent out with an incremented SN, and a timeout is set for each frame. Notably, the window size is verified prior to each frame transmission. Upon receiving an ACK from hap2, the ASN is extracted and the corresponding timeout is eliminated. The window base (B) is shifted to facilitate the transmission of the next frame within this window. In the event of a timeout in hap1, the SN is extracted from this timeout and forwarded to the re-transmission stage as shown in Figure 5.12.

In the retransmission stage, the system checks the size of the retransmission window to ensure it stays within the allowed limit for unacknowledged frames. This step helps regulate flow control and prevents overwhelming the receiver with too many frames at once. After confirming the window size, the system resends the frame to hap2 to recover any lost or corrupted data. This process ensures that only frames within the valid window are retransmitted, optimizing efficiency and maintaining reliable data delivery. If an ACK is received, hap1 processes the ACK, deletes the corresponding timeout for that frame, and checks the window base (B). The base is adjusted if necessary, and the system stays in the re-transmission stage. The base is updated only if the received ASN (Acknowledgment Sequence Number) equals the current base value plus one (ASN = B + 1). If true, the base shifts to ASN + 1, and the re-transmission process continues. If the check fails (ASN $\neq$ B + 1), the base remains unchanged, indicating the ACK was received out of order, and no base adjustment occurs.

As shown in Figure 5.12, the re-transmission stage involves three key events: frame timeout, frame re-transmission, and ACK reception. The blocked stage, depicted in Figure 5.13, is a phase where no frame transmission occurs. This stage checks certain conditions and then transitions to either the re-transmit or transmit stage. It includes three main events: a transmission event, timeout expiration, and ACK reception. If a transmission is attempted, an error occurs since transmissions aren't allowed in this stage. When a timeout expires, the required information is gathered, and the process moves to the re-transmit stage to resend the specific frame. If an ACK is received from hap2, the ASN information is extracted, the corresponding timer is canceled, the window base (B) is updated, and the process proceeds to the transmit stage.

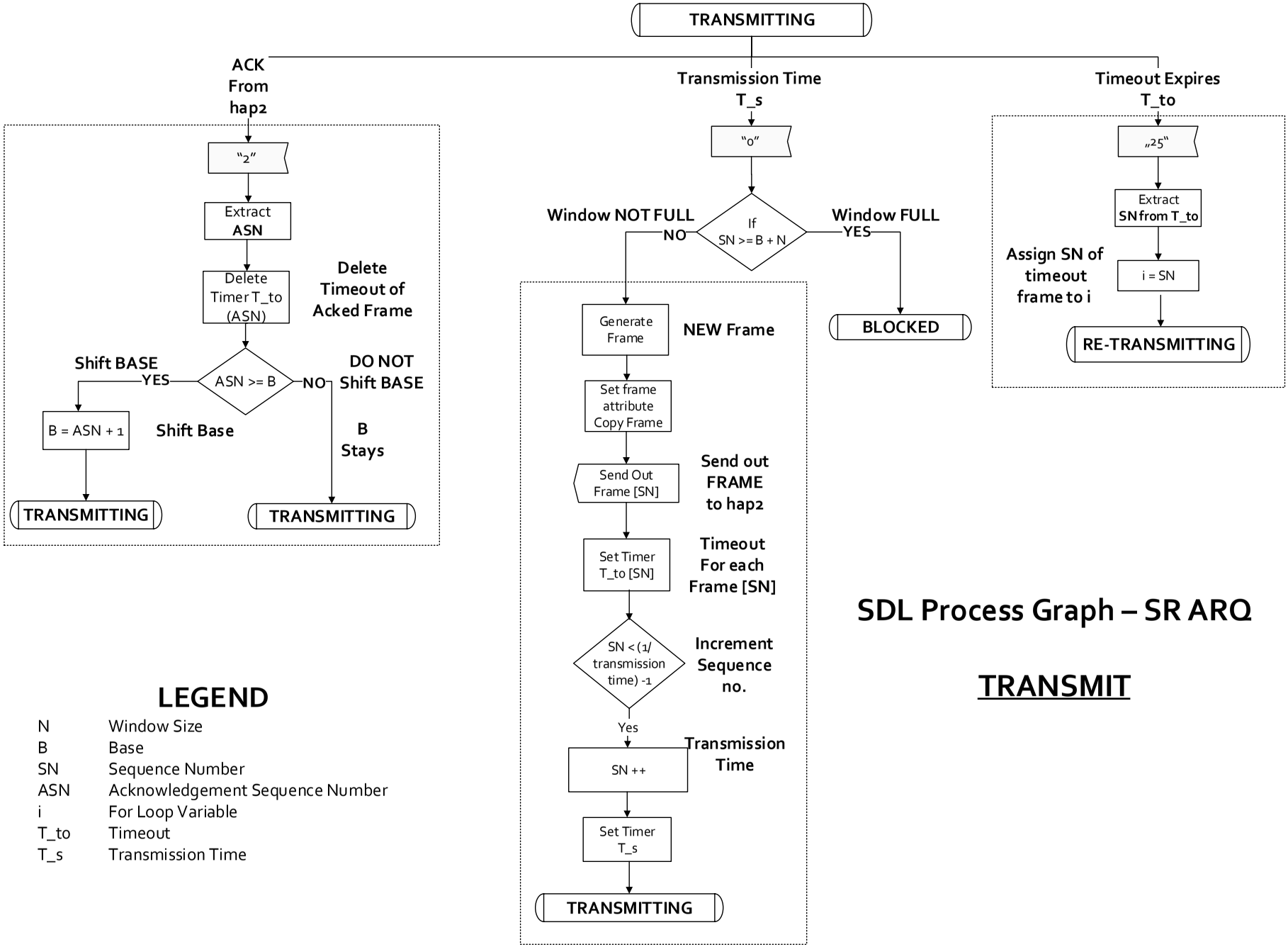

Figure 5.11.: SDL: hap1 transmit stage

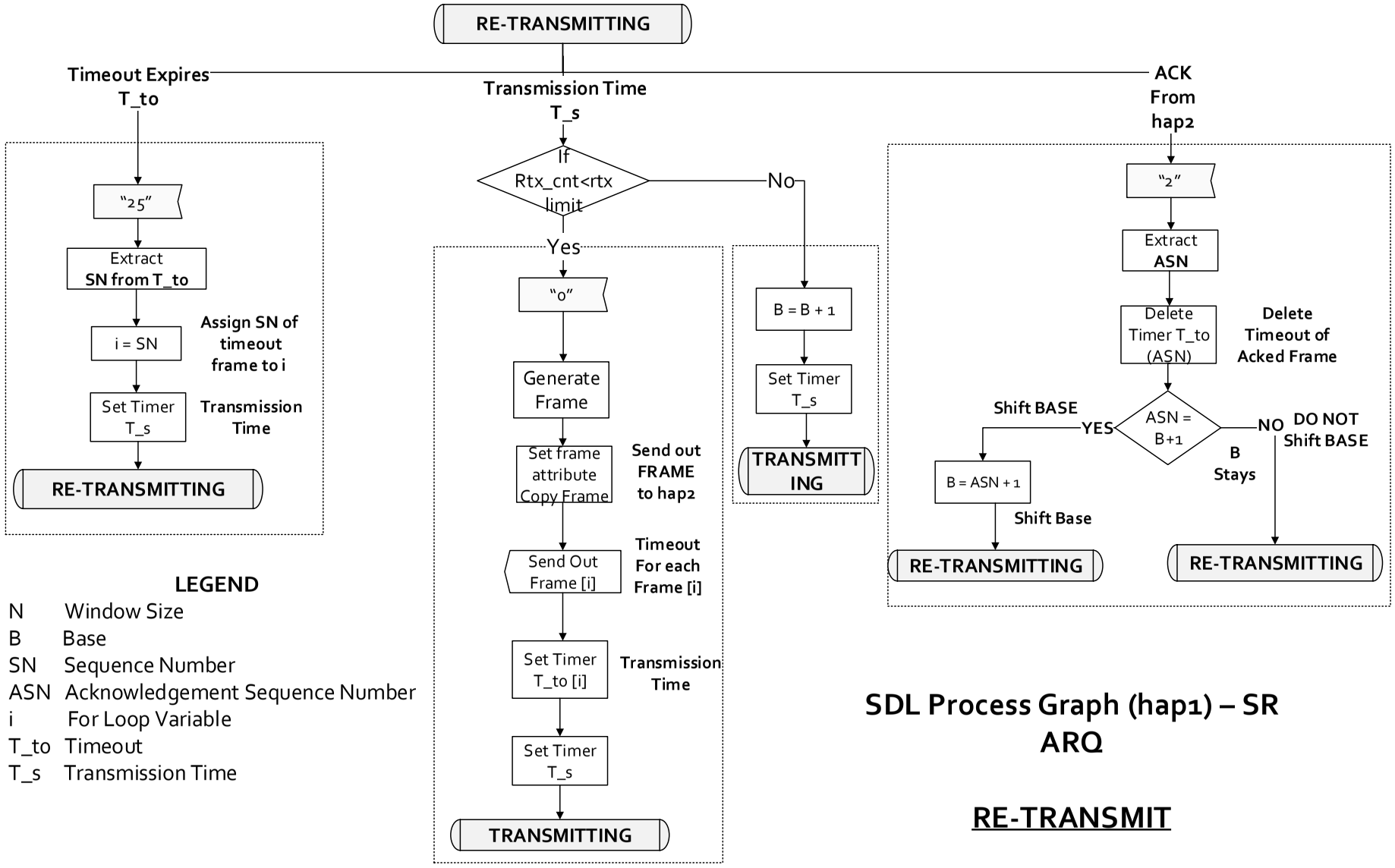

Figure 5.12.: SDL: hap1 re-transmit stage

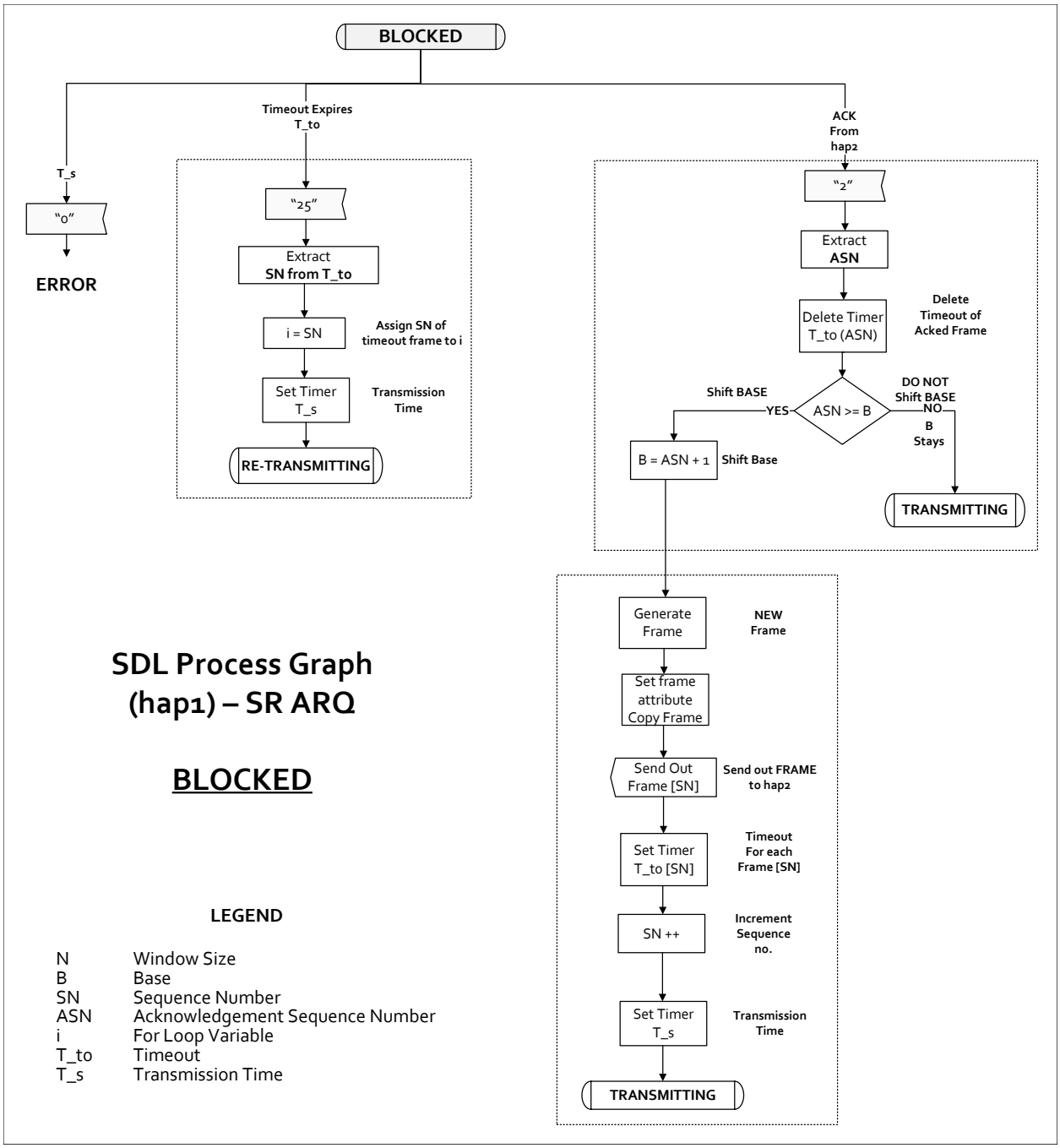

Figure 5.13.: SDL: hap1 blocked stage

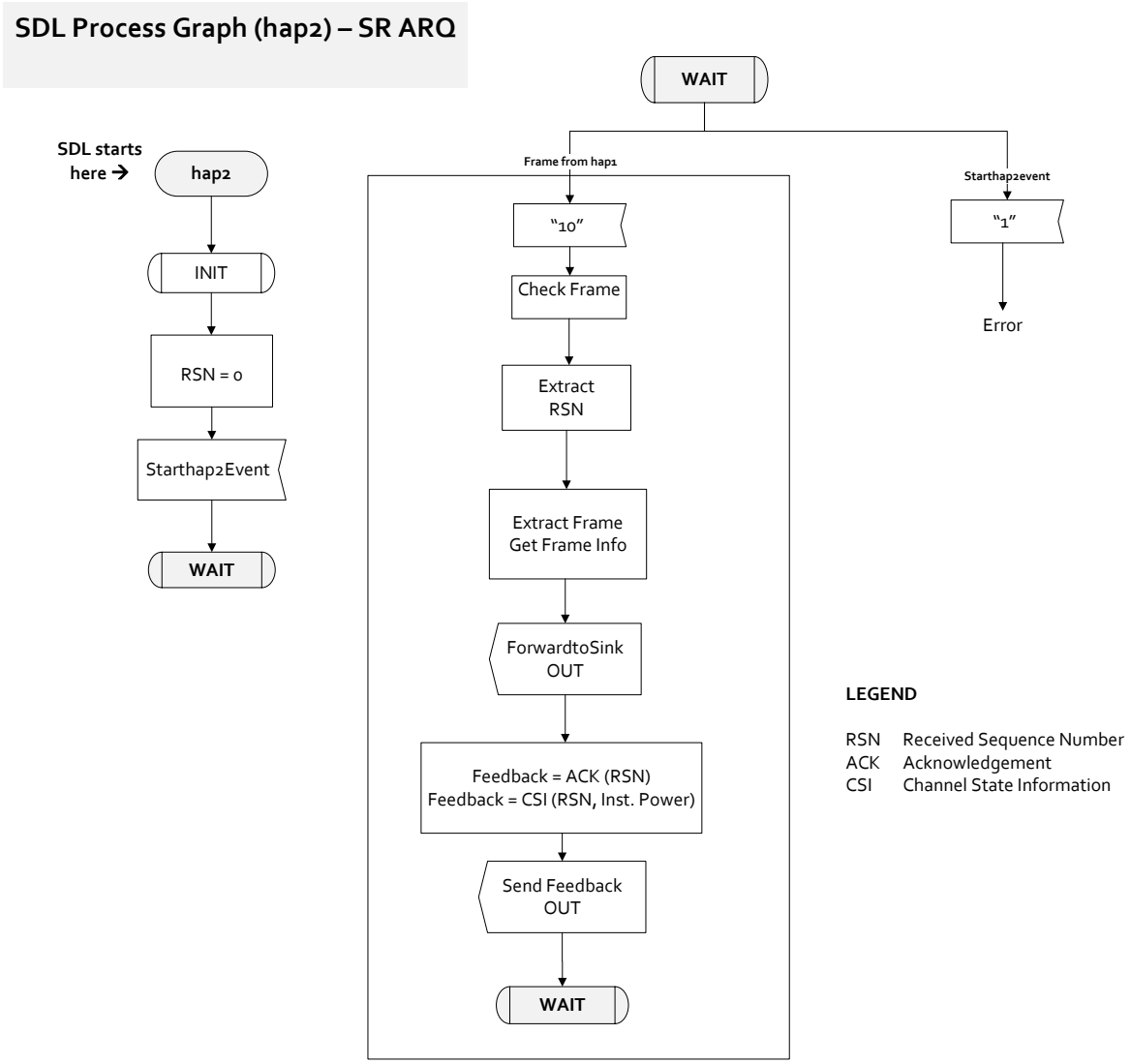

Figure 5.14.: SDL: hap2 wait stage

In hap2, the RSN begins with a value of zero and proceeds to a waiting stage, anticipating the frame from hap1. Once the frames arrive, the RSN and frame information are extracted for each frame. These frames are then forwarded to the sink. Subsequently, in the feedback channel, the corresponding ACK, replete with the RSN and CSI information, is dispatched. The system concept and the rationale for sending different CSIs and adapting the code rate were elaborated upon in Section 4.5.

5.3. Combining Channel and ARQ Simulation

The block diagram visualization of the combined FSO channel simulation and event-based ARQ simulation concept is represented in Figure 5.15. The FSO simulation, as described in Section 5.1,

was executed for both conventional and reciprocal inter-HAP channels, considering multiple scenarios that incorporate atmospheric effects, various scintillation strengths, pointing error impacts, and variable channel speeds. The output of this simulation is the time series of received power vectors. This time series serves as the input for the REF model detailed in Section 2.9.1, which calculates the Bit Error Probability (BEP) of the specific channel. The BEP is then used in conjunction with the Reed-Solomon code to compute the Packet Error Probability (PEP). The resulting PEP time series is then utilized as the input for the ARQ event simulation. The frame loses are generated using the cumulative binomial distribution function [134]. The ARQ simulation module, depicted in Figure 5.15, represents the event-based simulation in OMNeT++ for both HARQ (SR+RS) with and without adaptive-rate mechanisms. The HARQ and adaptive-rate simulation system described in Section 4.5 is implemented within the ARQ simulation.

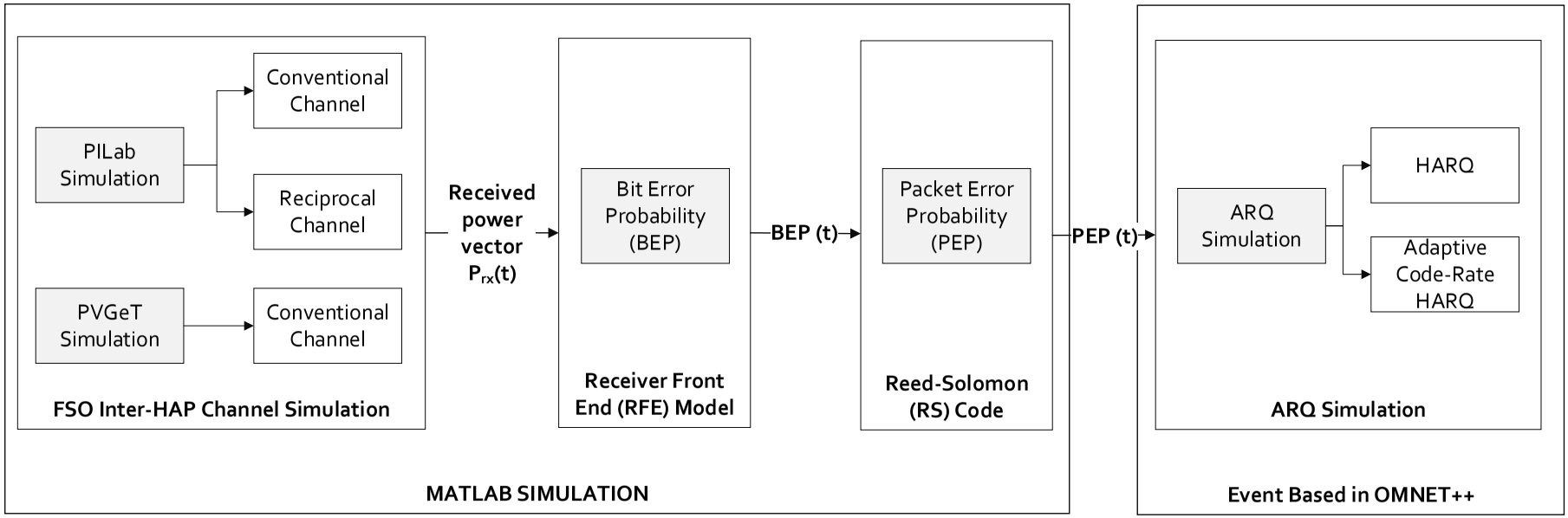

Figure 5.15.: Block diagram of the combination of FSO and ARQ simulation model.

5.4. Chapter Summary

A detailed presentation of the simulation models used to generate the inter-HAP channel and the event-based selective repeat HARQ model in OMNET++ was provided in this chapter. Channel simulations were conducted for a variety of scenarios involving both conventional and reciprocal FSO channels. PvGeT and PILab were the two methods employed for these channel simulations. Both methods were found to be beneficial and more accurate in modeling inter-HAP FSO channels. The event-based SR-ARQ simulation was integrated with the channel simulation to analyze the performance of HARQ protocols for inter-HAP FSO links, details of which can be found in Section 6.2 and Section 6.3.

6 Performance Evaluation

This chapter starts with the measurement and analysis of reciprocity, as elaborated in Section 6.1. Subsequently, it ventures into the assessment of ARQ and HARQ protocol performance in FSO communication systems for inter-HAP links, as detailed in Section 6.2 and Section 6.2. Simulations using OMNeT++ were conducted to evaluate transmission efficiency under various conditions including atmospheric turbulence, pointing errors, and multiple types of CSI. These studies underscore the significance of accurate and timely CSI for achieving optimal code rate adaptation and enhancing system performance. Finally, a summary of this chapter is provided in Section 6.4.

6.1. Evaluation of FSO Reciprocity Measurements

To assess the performance of a long-range bidirectional FSO communication system, we focused on a groundbreaking ground-ground reciprocal FSO link of 62.86 km. Using PILab, a Matlab-based tool, we conducted experimental observations and numerical simulations across various FSO scenarios. We measured correlated received powers for different aperture sizes and times of day, highlighting the variation in channel reciprocity for 5 cm and 2 cm apertures under varying turbulence. Additionally, we examined the inherent channel state information (CSI) provided by reciprocity in inter-HAP FSO links, which operate over long distances at lower stratospheric altitudes. Larger intensity speckles, relative to receiver apertures, amplify the reciprocity effect due to increased distances and symmetric turbulence, peaking at the link's midpoint. This study highlights the benefits of FSO channel reciprocity in improving the reliability and efficiency of long-distance bidirectional links, supporting the feasibility of power-in-bucket (PIB[1] - the average power that enters a receiver aperture) reciprocity as intrinsic CSI in inter-HAP FSO links.

6.1.1. Experiment Setup

The propagation path is illustrated in Figure 6.1. The term h_A signifies the location of terminal-A at the Augsburg hotel tower, while h_B marks the location of terminal-B at the German weather service on Hohenpeissenberg Mountain. An instance of the terminal setup, specifically terminal-B, is showcased in Figure 6.2. This link, stretching over 62.86 km, encountered fading due to atmospheric turbulence. On July 29, 2016, between 18:30 and 22:00 (UTC+2), the transceivers conducted 16 power measurement sequences while situated at corresponding altitudes of 596.51m (h_A) and 949.59m (h_B) above sea level.

[1] PIB refers to the laser light that is actually captured by the receiver.

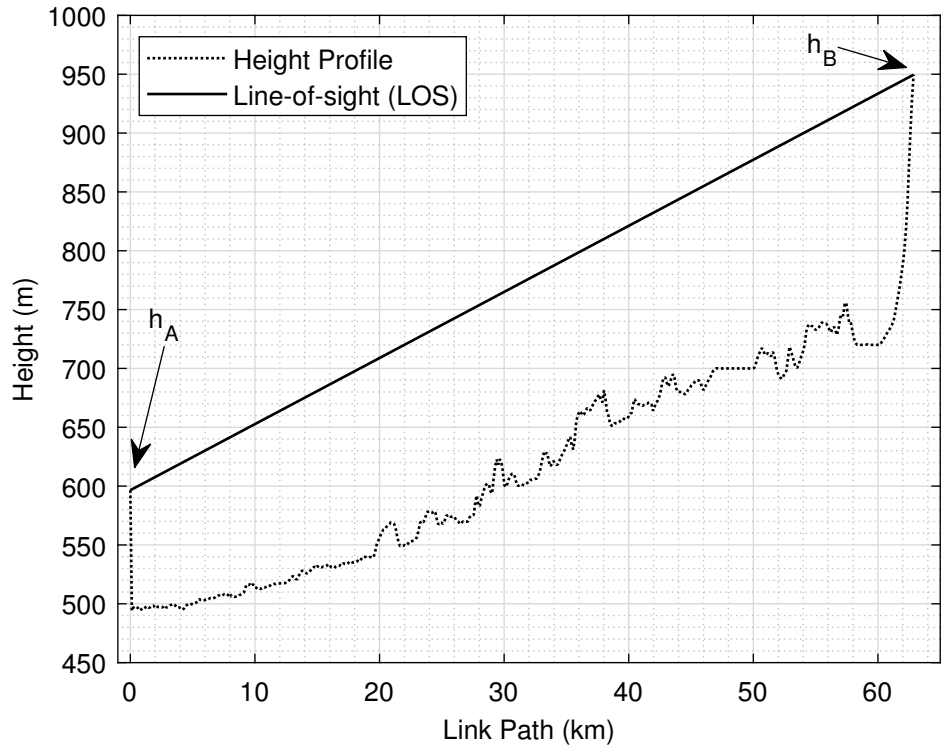

Figure 6.1.: Diagram illustrating the propagation path for reciprocity measurement.

Figure 6.2.: Bi-directional FSO transceiver terminal.

The power of the transmitted beam from the laser transmitters was adjusted to range between 2 W and 3 W, employing continuous-wave Gaussian beams. These beams featured an unmodulated wavelength of 1590 nm and a divergence of 506 μrad in the full-angle $1/e^2$ intensity profile. The beam was aimed at the center of the receiver apertures, with sizes of either 5 cm or 2 cm. Upon reception, the beam was collimated through an optical detector with adjustable gain and a 16-bit AD converter, utilizing a focal length of 300 mm. The received signals were captured at terminals A and B, each for 100 seconds at a 10 kHz sampling rate. Post-processing measures were imple-

mented to correct offsets from electronic and ambient light sources. The layout of the measurement setup is displayed in Figure 6.3.

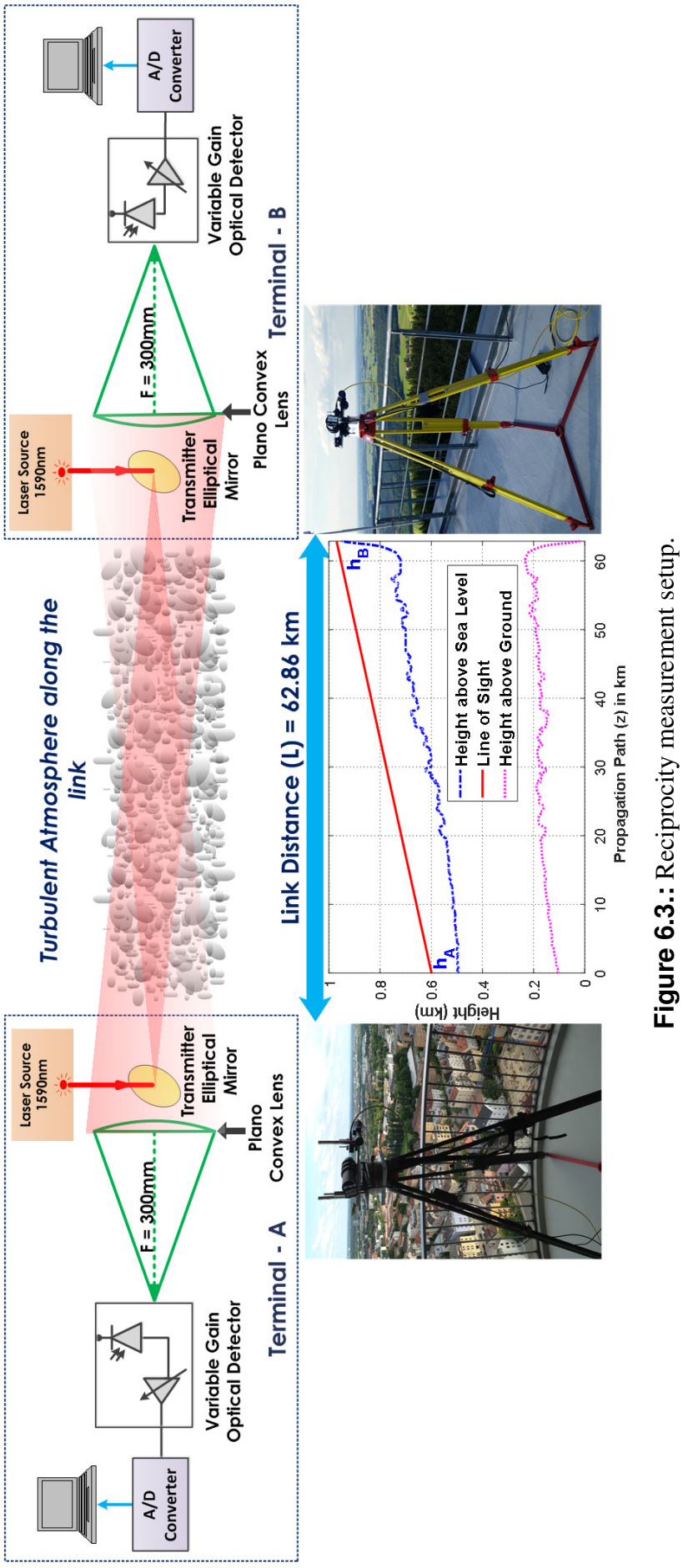

Figure 6.3.: Reciprocity measurement setup.

6.1.2. Channel Model and Parameters

To evaluate the effect of turbulence on FSO links, it is necessary to determine the C_n^2-profile based on the height above the ground. The Hufnagel-Valley (HV) model [4], often used for this purpose, scales the Index of Refraction (IRT) structural function of the atmosphere. However, this model is unsuitable for near-ground situations, such as a horizontal path ranging from a few meters to about 250 meters above ground level. For our numerical simulations, we utilized the Walters and Kunkel model [48], offering a suitable solution for our scenario detailed in Section 2.4.2.

Three values of $C_n^2(h_0)$ for $h_0 = 1m$ were selected based on our measurement time, presuming $p = \frac{2}{3}$. These values: $6.50e^{-16}$, $1.20e^{-15}$, and $8.11e^{-15}$, were chosen to best match the measured scintillation index values of 0.301, 0.537, and 1.309, as shown in Table 6.1. It's worth noting that C_n^2 is expected to be significantly smaller and fluctuate less in inter-HAP links due to a smoother C_n^2-height profile. In our scenario, a transmit beam with a large divergence can be treated as a spherical wave, as stated on page 281 of [4]. The Power Scintillation Index (PSI), detailed in Eq. (2.10), is defined as the normalized variance of received power P into a given receiver aperture diameter (D_{rx}) in Section 2.5. The Rytov variance of a spherical wave is denoted by β_0^2, and it equates to 0.4 times the Rytov variance of a plane wave, denoted by σ_R^2. This thesis employs the Power Scintillation Index (PSI), Correlation Coefficient (CCF), Normalized Mean Squared Error (NMSE), and Half Width Half Maximum auto-covariance (HWHM acov.) to assess measurement and numerical simulation results. These parameters, considered measures of reciprocity, are described in Section 2.10.1. The equations expressing the CCF and NMSE are represented by Eq. (2.20) and Eq. (2.21), respectively.

6.1.3. Experimental Results

This section introduces and scrutinizes the test results that have been validated through numerical simulation to bolster the precision of our experimental outcomes. The uniformity of results under identical conditions is affirmed by controlled simulations. The congruence between the simulated and experimental datasets underpins the veracity and statistical relevance of our experimental information. Noteworthy correlations between experimental and simulated datasets are unveiled when crucial parameters such as the Power Scintillation Index (PSI), Correlation Coefficient (CCF), Normalized Mean Squared Error (NMSE), and Half Width Half Maximum auto-covariance (HWHM acov.) are considered. Precision is guaranteed by averaging data across five timelines, offering unequivocal evidence of reciprocity in lengthy, two-way free-space optical (FSO) communication.

6.1.3.1. Analysis of Measurement Results

Table 6.1 displays a summary of measurement results. In Figure 6.4, you can view the measured optical powers at both terminals, while Table 6.1 presents observations. The Figure 6.5 graph illustrates CCF, NMSE, and PSI variations. Across different parameters, CCFs ranged from 0.803 (5 cm D_{rx}) to 0.984 (2 cm D_{rx}), PSIs from 0.24 to 2.1, and HWHM acov. from 11.05 ms to 43.65 ms. Measurements spanned from pre-sunset to night, with consistently lower power received at

terminal B due to increased turbulence near terminal A. The mean power loss due to transmit mirror obscuration was approximately 63% and 25% for 2 cm and 5 cm D_{rx}, respectively. Terminal B consistently exhibited higher PSI values, indicating more turbulence near terminal A. These results affirm the effectiveness of FSO communication in turbulent atmospheres and the potential for reciprocal CSI to enhance performance and reliability.

Time of measurement sequence (German local time)[a]	Mean received power at A (nW)	Mean received power at B (nW)	PSI at A	PSI at B	HWHM acov. at A (ms)	HWHM acov. at B (ms)	CCF	NMSE
18:57	368.64	226.92	2.034	2.118	43.65	38.65	0.894	0.4385
19:04	375.73	185.18	1.4509	1.739	32.35	28.05	0.8702	0.425
19:07	405.78	201.63	1.309	1.504	40.75	37.45	0.9104	0.258
20:30	277.13	227.94	0.513	0.584	25.05	23.35	0.9509	0.056
20:33	272.91	237.11	0.537	0.622	25.45	23.75	0.966	0.042
20:46[b]	20.29	18.54	0.352	0.493	24.15	24.05	0.984	0.025
20:49[b]	21.57	20.80	0.301	0.353	22.35	21.95	0.9807	0.014
20:54	366.86	317.69	0.430	0.498	23.65	22.05	0.9608	0.039
21:00	371.05	300.57	0.425	0.497	21.55	19.05	0.938	0.059
21:21	386.68	264.41	0.271	0.377	18.15	14.15	0.869	0.093
21:25	402.6	241.02	0.411	0.593	16.75	13.05	0.856	0.159
21:34	401.85	682.85	0.283	0.431	15.75	11.95	0.842	0.125
21:43	697.48	638.41	0.243	0.397	15.15	11.05	0.803	0.141
21:46	690.84	615.41	0.255	0.414	16.75	12.85	0.826	0.132
21:50	720.39	612.98	0.317	0.495	18.65	15.15	0.844	0.143
21:53	700.42	579.68	0.308	0.446	20.55	16.65	0.866	0.112

Table 6.1.: Summary of measurement results for the 62.86 km bidirectional FSO link.

Note: [a]All measurements were performed on July 29, 2016; local time = UTC+2; sun set: 21:30 local time, [b]For receiver aperture diameter $D_{rx} = 2cm$.

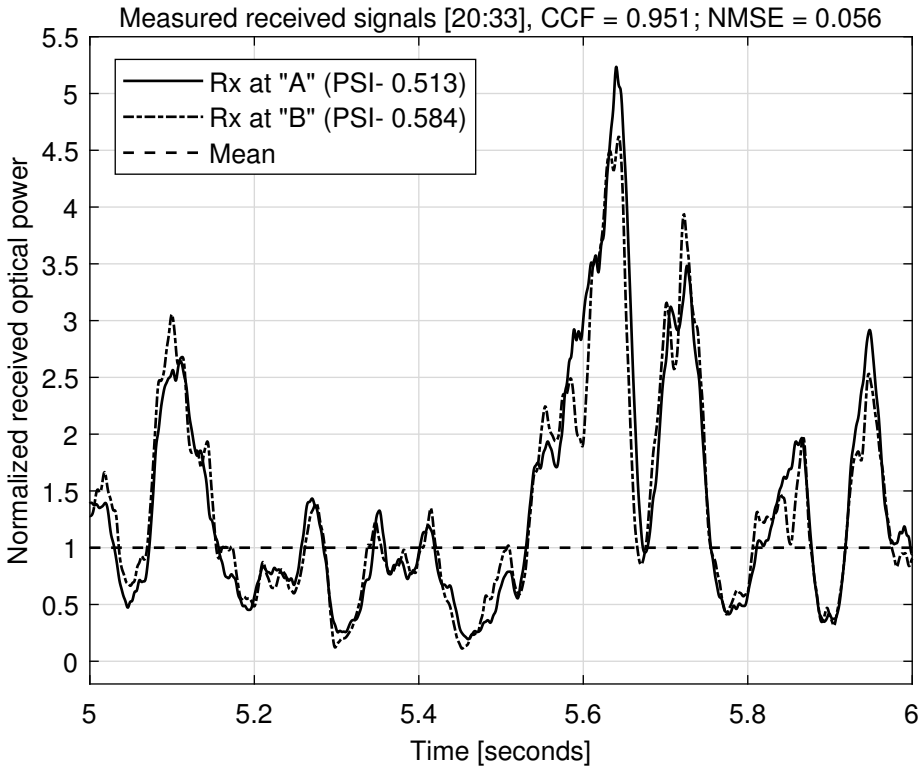

Figure 6.4.: The optical powers measured during reciprocity measurements.

Note: Simultaneously measured received optical powers at terminals A and B for 5 cm D_{rx} for the measurement sequence [20:33], as displayed in the Table 6.1.

In Figure 6.6 (a), CCF variations for mean PSI values with D_{rx} 2 cm and 5 cm are depicted. Notably, high CCFs are observed not only for PSIs < 1 but also under strong turbulence (PSIs > 1), indicating that a strong correlation can persist even in turbulent conditions. The figure also highlights that NMSE values are higher for PSIs > 1, signifying that while correlation remains high, channel estimation quality declines in strong turbulence. These results imply that reciprocal CSI remains beneficial for FSO systems under strong turbulence, enabling adaptive transmission techniques that adjust to current channel conditions. However, handling reciprocal CSI in such conditions may necessitate additional processing and compensation techniques due to reduced channel estimation quality.

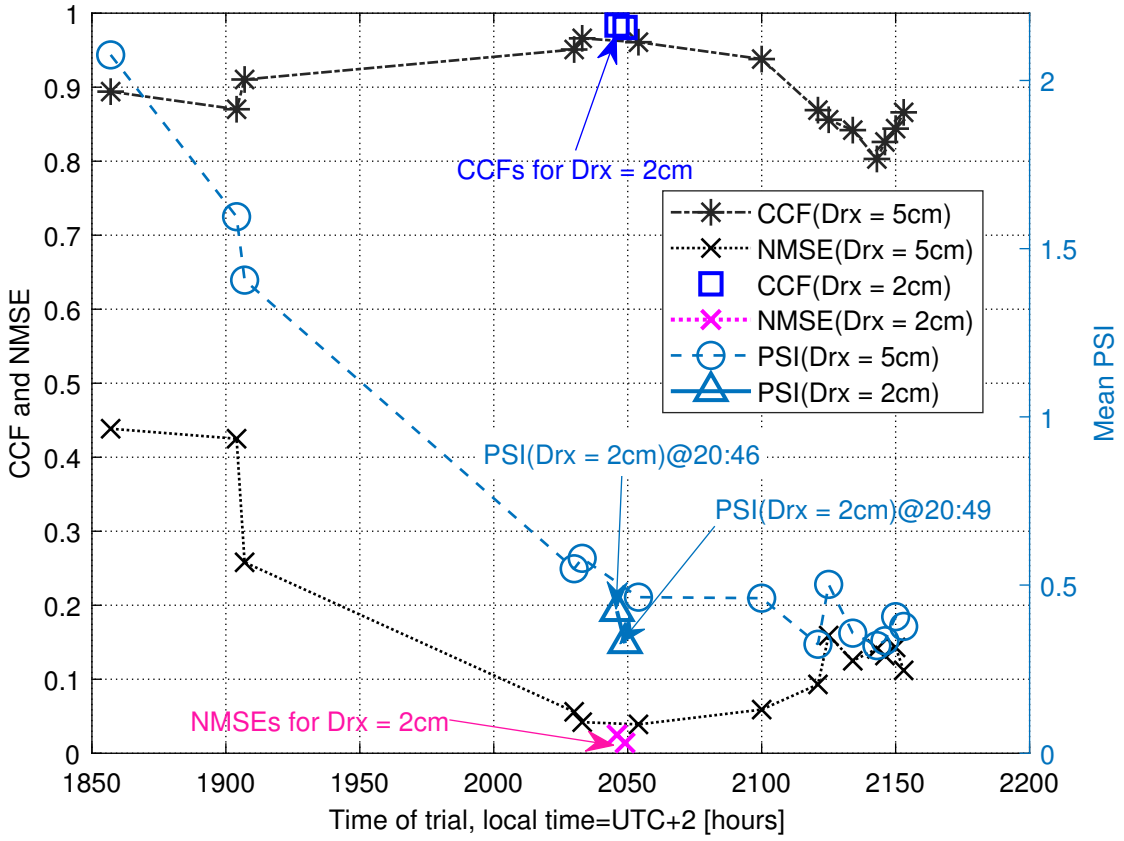

Figure 6.5.: Overall observed CCF, NMSE, and mean PSI variations over measurement time.

In Figure 6.6 (b), mean HWHM acov. values are presented for various mean scintillation strengths. Findings reveal that weaker turbulence (PSIs < 0.5) leads to faster scintillations, while PSIs > 1 result in slower scintillations (almost twice the auto-covariance time). This phenomenon is attributed to orthogonal wind speed changes along the link. Furthermore, as indicated in Table 6.1, the channel slows down and scintillation strength decreases towards sunset and night. Overall, these results underscore how atmospheric turbulence affects the speed and strength of scintillations. Understanding this can aid in designing robust FSO communication systems capable of handling variations in scintillation strength and speed induced by atmospheric turbulence.

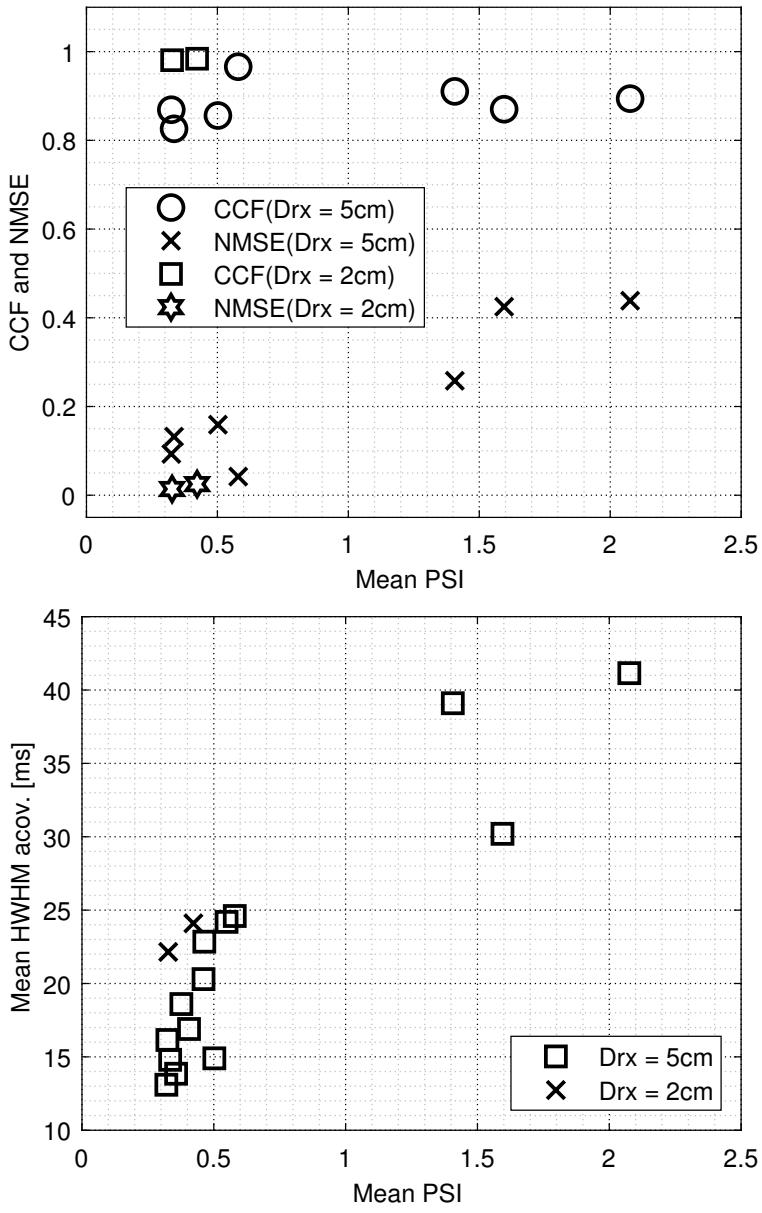

(a) CCF and NMSE for different mean PSI.

(b) Mean HWHM acov. versus mean PSI. Mean refers to average of parameters at A and B.

Figure 6.6.: CCF, NMSE and Mean HWHM auto-covariance comparison for different mean PSI.

6.1.3.2. Simulative Verification Using PILab

To get PILab simulations to match what was seen, three different measured vectors were chosen, each of which corresponded to a different scintillation strength and CCF. These vectors encompassed two 5 cm and one 2 cm D_{rx} configurations, spanning PSI values from 0.3 to 1.5, signifying turbulence ranging from weak to strong conditions [4]. The C_n^2-profile was calculated using Eq. (2.5). and used to simulate diverse turbulence conditions by adjusting $C_n^2(h_0)$ at h_0 = 1 m, as shown in Figure 6.7. PILAB conducts atmospheric propagation simulations that represent spatial and temporal turbulence dynamics through phase screens that are laterally shifted based on orthogonal winds. These winds, assumed to range from 1 m/s to 2 m/s (matching measured HWHM acov.), induce temporal fluctuations in received power signals. Through these simulations, the re-

sults consistently aligned with measured data, affirming the experimental methodology's validity. These simulations serve as valuable tools for predicting performance under varied atmospheric conditions and for designing and optimizing FSO communication systems across diverse applications.

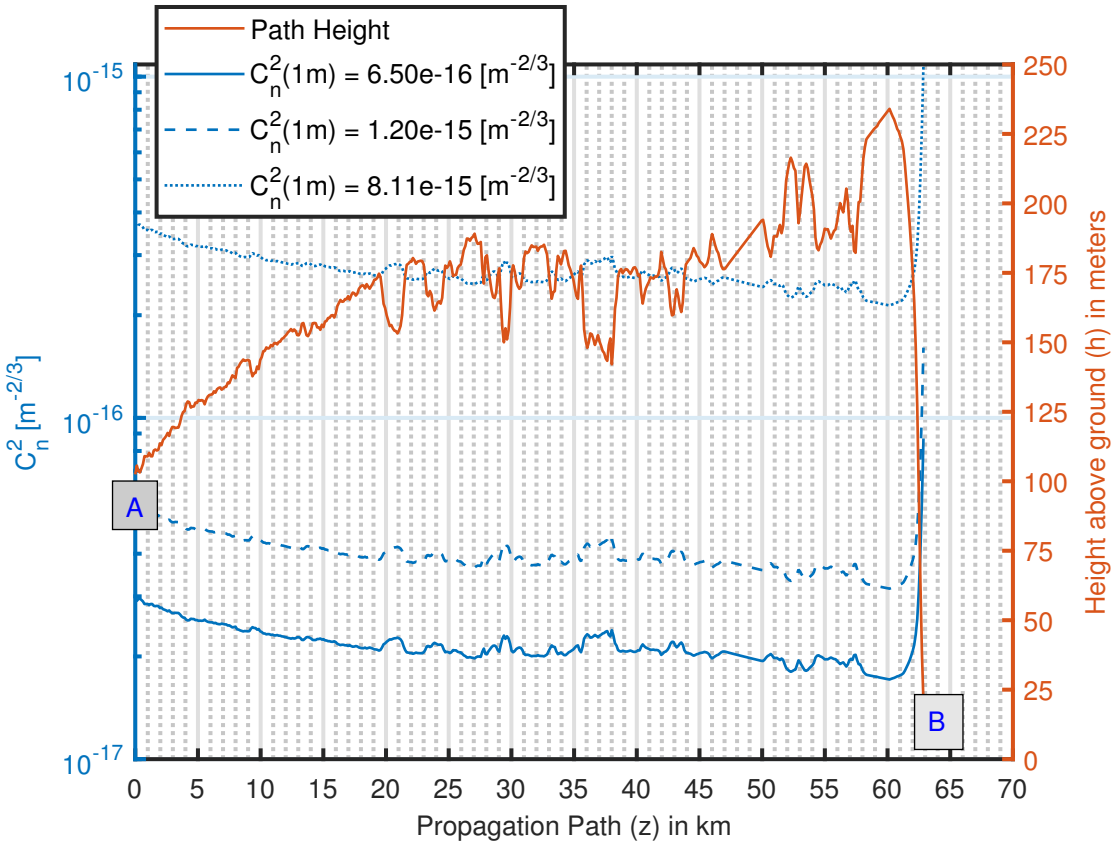

Figure 6.7.: C_n^2-profile along the propagation path z (terminal A on Augsburg-Tower, terminal B at DWD-Hohenpeissenberg).

Note: The path height refers to height above the ground and three different C_n^2-profiles used for PILab simulations are shown for chosen C_n^2-profile at 1 m (h_0).

Figure 6.8 displays two simulated instantaneous received intensity fields generated using PILab. Additionally, Figure 6.9 presents a comparative analysis, utilizing the lognormal distribution, of the estimated probability density function (PDF) against both measurement and simulation data. This comparison reveals a strong alignment between simulation outcomes and analytical as well as measured results, particularly for a PSI value of 0.537, matching the measured data. Notably, outliers in the simulated PDF values arise from the finite size of the phase screens, which are laterally displaced in accordance with wind speed. Through phase screens, PILab simulations use models of atmospheric propagation to show how turbulence changes over time and space. These screens shift laterally based on orthogonal wind, assumed within the range of 1 m/s to 2 m/s (consistent with the measured HWHM acov.). By varying $C_n^2(h_0)$ at $h_0 = 1m$, PILab successfully simulates various turbulence levels, enabling a meaningful comparison with measured data and the replication of FSO communication system behavior.

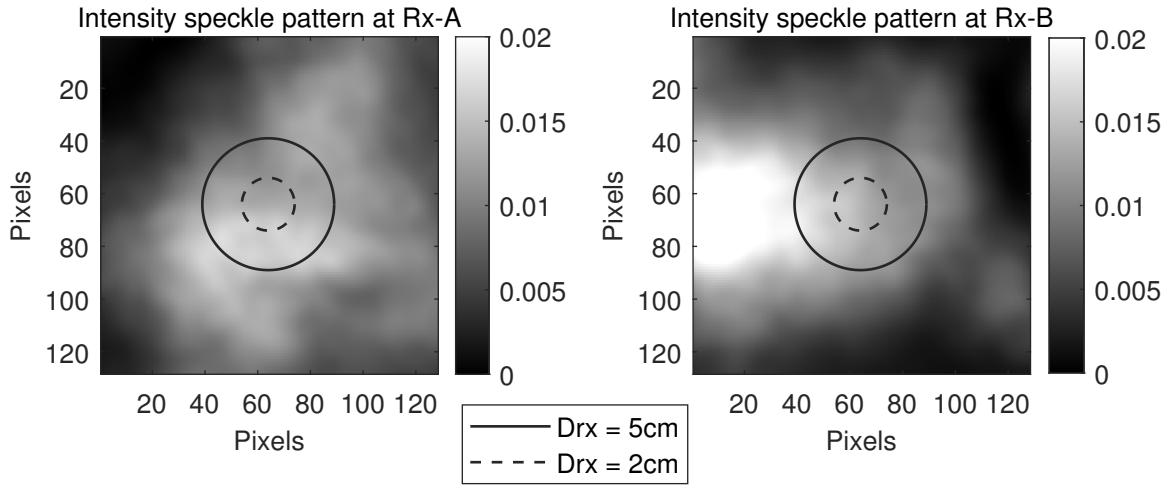

Figure 6.8.: PILab simulated intensity speckle patterns at receivers A and B.

Note: The circles represent two different D_{rx} 2 cm and 5 cm. The x and y axis are in pixels with each pixel = 1 mm. The color bars represent equally scaled absolute intensity values.

Parameters	EXP [19:07]	SIM	EXP [20:33]	SIM	EXP[a] [20:49]	SIM[a]
PSI-A	1.309	1.359	0.537	0.517	0.301	0.337
PSI-B	1.504	1.167	0.622	0.561	0.353	0.361
CCF	0.91	0.93	0.96	0.91	0.98	0.92
NMSE	0.258	0.178	0.042	0.09	0.014	0.055
HWHM acov. -A (ms)	40.75	35.65	25.45	23.95	22.35	29.75
HWHM acov. -B (ms)	37.45	32.65	23.75	24.35	21.95	26.65

Table 6.2.: Comparison of experimental observations and PILab simulations.

Note: [a]For receiver aperture diameter D_{rx} = 5 cm.

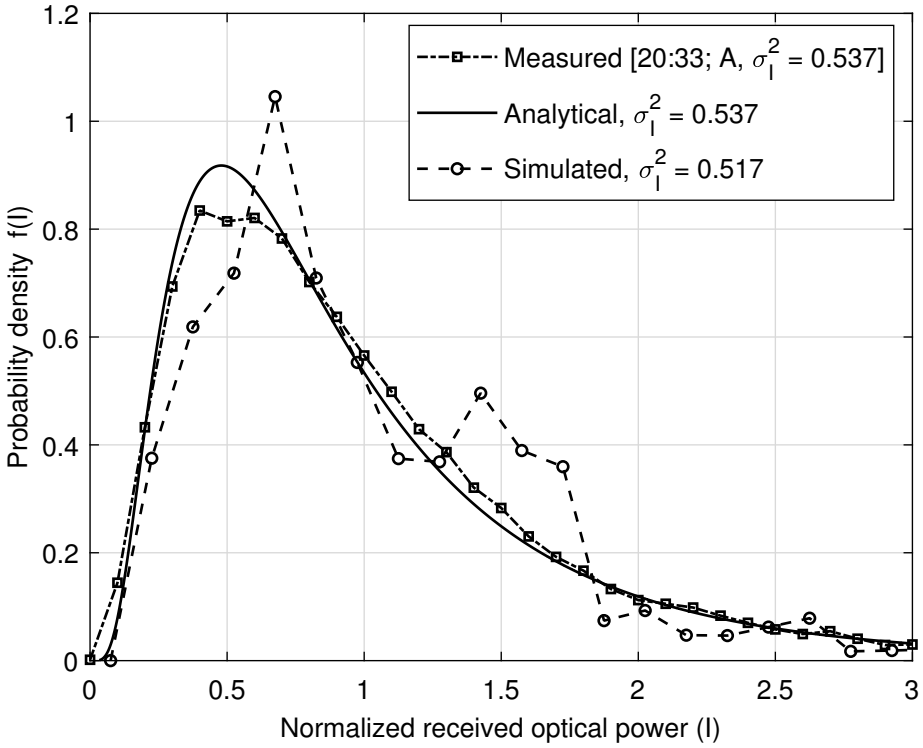

Figure 6.9.: PDFs of received power fluctuations obtained from measurements.

Note: PILab simulation, and analytical distribution for D_{rx} = 5 cm are compared.

Table 6.2 summarizes our measured and simulated results, demonstrating strong alignment across various parameters. To derive the Probability Density Function (PDF), we averaged five time series, extending the total power vector length to 10 seconds. Both experimental and simulation data show that Free-Space Optical (FSO) communication systems can operate effectively in turbulent conditions. Our findings indicate that the reciprocity of the FSO channel enhances its effectiveness and reliability. We documented the longest ground-to-ground bi-directional FSO link, with strong correlations observed in both communication directions. This enables strategies to mitigate signal scintillation caused by atmospheric turbulence. Real-time awareness of channel conditions, referred to as "reciprocal Channel State Information (CSI)," can inform adaptive methods, such as adjustments to code or data rates and hybrid Automatic Repeat reQuest (ARQ) techniques. Reciprocal CSI can reduce retransmission time by half in multi-hop High Altitude Platform (HAP) systems compared to conventional ARQ protocols, providing substantial benefits for future HAP-based global communication networks.

6.2. Performance Evaluation of Hybrid ARQ for FSO Inter-HAP Link

ARQ mechanisms are critical in free-space optical (FSO) communication systems for ensuring reliable data transmission. Signal degradation in FSO channels is caused by factors such as atmospheric turbulence and pointing errors. ARQ schemes must be tailored to the specific FSO

inter-HAP channel, fading statistics, and bit error probability (BEP) characteristics to achieve optimal performance. ARQ mechanisms have been shown in studies to be effective in mitigating errors in FSO systems [135, 136, 110, 137][135, 136, 110, 137]. These mechanisms enable the receiver to request that incorrectly received packets be retransmitted, ensuring reliable data delivery. However, the ARQ scheme's design and customization are critical factors in its effectiveness in FSO systems.

This section aims to improve on the channel model used Chapter 2 for a bi-directional symmetrical inter-HAP link with a distance of 400 km by accounting for the combined impact of optical scintillation caused by IRT and beam miss-pointing. On this refined channel model, we run simulations to generate bit error probability (BEP) characteristics. We investigate the performance of various automatic repeat request (ARQ) mechanisms in terms of transmission efficiency using event-based simulations based on the results obtained. In addition, we evaluate performance using the widely used Reed Solomon code, RS (255, 239), a Forward Error Correction (FEC) scheme. This section is laid out as follows: Section 6.2.1 includes a detailed description of the channel model as well as the scenarios chosen for performance analysis. The channel simulation, as well as the probability density function (PDF) of the received power vectors, are presented in Section 6.2.1.3. We go over the error probability in great detail in 6.2.1.4. The simulation parameters for the selected ARQ mechanisms are described and defined in Section 6.2.2.1. Section 6.2.2 contains a detailed analysis and discussion of the numerical results.

6.2.1. Inter-HAP FSO Channel

The optical link is influenced by atmospheric conditions, including optical turbulence caused by spatial intensity deviations. The Hufnagel-Valley model is used to simulate the altitude profile of the C_n^2 parameter, which represents the atmosphere's index-of-refraction structure function [4]. We calculate C_n^2-profiles in this study using two wind speeds: 10 m/s (best case) and 30 m/s (worst case). The calculations are based on data that has been measured [138]. Figure 2.4 illustrates the varying strengths of C_n^2-profiles at different altitudes, highlighting the impact of wind speeds. The intensity scintillation index (ISI) also calculates the normalized variance of irradiance fluctuations in the atmospheric channel. We consider two scenarios to assess the impact of turbulence and beam miss-pointing on the ISI: "Best" and "Worst," which correspond to the different C_n^2-profiles described in Section 2.4. The C_n^2-profiles along the Inter-HAP link path over the curved earth surface are shown in Figure 2.4 (a) indicating that the strongest turbulence occurs in the center, representing the lower part of the link.

C_n^2 **Case**	**Link Distance** L **(km)**	**HAP Height** H_{hap} **(km)**	**Graze Height** G_h **(km)**	**Intensity Scintillation Index (ISI)**
Best	400	22	18.87	0.008
Worst				0.65

Table 6.3.: Two different Inter-HAP scenarios for HAP Heights at 22 km.

We established a bi-directional inter-HAP channel with a link distance of 400 km, with HAPs positioned 22 km above sea level, resulting in a minimum graze height (G_h) of 18.87 km. Based on different C_n^2-profiles detailed in Section 2.4, we considered two scenarios: best-case and worst-case. The intensity scintillation index (ISI), which measures the standard deviation of irradiance fluctuations, was used to assess channel performance. A detailed description of these scenarios can be found in Table 6.3. In the best-case scenario, the C_n^2-profile shows smooth variations, leading to limited intensity fluctuations and a low ISI, indicating high transmission efficiency. Conversely, the worst-case scenario features a turbulent C_n^2-profile with increased intensity fluctuations and a higher ISI, resulting in lower transmission efficiency. By defining these scenarios, we can simulate the inter-HAP channel and evaluate its performance under varying conditions, enabling us to identify optimal ARQ mechanisms for each scenario and enhance transmission efficiency.

6.2.1.1. Link Budget Calculation

The link budget for an inter-HAP scenario takes into account several parameters that affect the link's performance. These parameters are detailed in Table 6.4, which includes transmitter power, aerial gains, distance, atmospheric losses, and receiver sensitivity. These factors are considered in the link budget calculation to determine the received power at the receiver and compare it to the minimum detectable signal, ensuring reliable detection. The smallest detectable signal is the smallest signal that the receiver can detect while maintaining a certain bit error ratio (BER). Table 6.4 takes into account the inter-HAP scenario's unique parameters, such as the distance between the HAPs, aerial gains, and atmospheric losses. The results of these calculations provide critical information about the performance of the link, such as the expected signal strength at the receiver and the link margin. Atmospheric losses in the link budget Table 6.4 refers to the signal attenuation caused by atmospheric conditions, such as absorption, scattering, and turbulence, as the signal travels. This loss reduces the signal strength at the receiver, impacting overall link performance.

Parameters	Symbol (Unit)	Value
Mean Transmit Power	P_{tx} (mWatt)	0.055
Link Distance	L(km)	400
Channel rate (including $8b/10b$ line code)	R (Gbps)	1.25
Wavelength	λ (nm)	1550
Transmitter Divergence, FWHM	θ_{tx} (μrad)	85
Rx- Aperture Diameter	D_{rx} (cm)	15
Atmos. Losses	a_{atmos}(dB)	0.670
Receiver sensitivity for $BER = 1E-9$	S_{rx}(nW)	128.26
FEC Coding Gain for $BER = 1E-6$ and $RS(239,255)$	FEC_{gain}(dB)	4
Link Margin	L_m (dB)	0.01

Table 6.4.: Static link budget for bi-directional Inter-HAP scenario (no dynamic scintillation loss regarded)

6.2.1.2. Impact of Pointing Error

We chose a residual pointing error of σ_{rms}= 20 μrad and a full width half maximum (FWHM) $1/e^2$divergence angle of 85 μrad to strike a balance between these competing factors. This choice is consistent with the recommendations made by [64] on the design considerations for FSO links. We hope to achieve a satisfactory trade-off between pointing losses and divergence angle by using these specific values, thereby optimizing the overall performance of the FSO Inter-HAP link.

6.2.1.3. Channel Simulation

In our inter-HAP channel scenario, we used the link budget analysis calculations to generate a time series of received power. The inter-HAP channel is affected by atmospheric turbulence, which causes scintillation effects such as fades and surges. The turbulence state is frequently modelled as a random process with a log-normal distribution in moderate turbulence conditions. We used

the methodology described in [131] to represent the interaction between turbulence and pointing error, which provides insights into the optimal representation.

Figure 5.9 depicts the probability density function (PDF) of the generated optical receiver power, which provides valuable insights into the behavior of the inter-HAP channel under various turbulence and pointing error conditions. We can examine the PDF to see the frequency of different power levels, which provides information that helps us understand the likelihood of different bit error probabilities (BEPs). This knowledge is critical for selecting the best ARQ scheme and its parameters in various scenarios. In the following sections, we will go over the simulations that were run to evaluate the transmission efficiency of various ARQ mechanisms based on the BEP characteristics of the inter-HAP channel. These simulations were created specifically to evaluate the effectiveness of these mechanisms. The simulation results will be presented and discussed, shedding light on the efficacy of various ARQ schemes and assisting in the selection of appropriate strategies for achieving efficient transmission in the inter-HAP channel.

6.2.1.4. Bit Error Probability

We consider the combined impact of atmospheric turbulence-induced fading and pointing error-induced fading on channel performance in our analysis. These fading events change the bit error probability (BEP) distribution over time. The presence of fading effects in our channel results in an uneven distribution of bit errors across the transmitted data, and the magnitude of the BEP varies depending on the channel's current state. The dynamic fading behavior of BEP for the bidirectional inter-HAP link illustrating the impacts of atmospheric and pointing errors is illustrated in Figure 2.10 (a) and Figure 2.10 (b) under both best-case and worst-case channel conditions. The horizontal straight line in these plots represents the mean value of the simulated BEP. Analyzing the BEP over time provides useful insights into the channel's performance and aids in the selection of appropriate ARQ mechanisms and parameters to improve system efficiency and reliability.

6.2.2. Performance Comparison Results

This section investigates the transmission efficiency of GBN-ARQ and SR-ARQ mechanisms through simulations that assess their performance under various constant bit error probability (BEP) values and best/worst-case inter-HAP scenarios from Table 6.3. The simulations, conducted in the OMNET++ environment, included scenarios with and without Forward Error Correction (FEC), utilizing PEP vectors derived from time-varying BEP fades as outlined in Section 6.2.1.4. The resulting ARQ performance for these fading channels is illustrated in Figure 6.10 and Figure 6.11, factoring in the mean BEP values of the fading channels. Notably, the simulation results include 95% confidence intervals for each measurement point, although these may not be visible in the figures. The ARQ performance of GBN-ARQ and SR-ARQ mechanisms can be approximated using the methods from [34]. Transmission efficiency (TE) represents the portion of the channel bit rate available for payload transport before 8b/10b line coding, as described in Section 3.4.4. The simulation results reveal that TE for both GBN-ARQ and SR-ARQ mechanisms varies significantly

with the channel's instantaneous BEP. The performance of FEC-enabled SR-ARQ consistently exceeds that of GBN-ARQ across all constant BEP values. In the best-case scenario, both mechanisms perform similarly without FEC; however, with FEC, SR-ARQ outperforms GBN-ARQ, as detailed in Section 3.5.2. Both mechanisms experience significant performance degradation in the worst-case channel scenario, especially at high BEP values, yet SR-ARQ still demonstrates better performance compared to GBN-ARQ.

6.2.2.1. ARQ Parameter Definition

We used the OMNET++ [133] simulation library to conduct a detailed analysis of various sliding-window-based ARQ mechanisms, as described in Section 5.2. We were able to evaluate the transmission efficiency of ARQ with and without the Reed Solomon code (255, 239) for FEC using this simulation environment. We ran these simulations using the simulation parameters specified in Table 6.5. The frame length for non-FEC transmissions was 239 bytes and 255 bytes for FEC transmissions. A 10-byte overhead for ARQ sequence numbers, control information, headers, and CRC check bits was also considered. The transmitter window sizes were determined using the inter-HAP link's round-trip time, frame transmission time, and a net data rate of 1 Gbps (before 8b/10b line coding). We were able to thoroughly analyse the performance of ARQ mechanisms and identify the most efficient approach for achieving reliable data transfer using these simulations.

Parameter	Without FEC	With FEC	Symbol	Unit
Total Frame Length	1912	2040	n_{total}	$bits$
Overhead	80	208	$n_{overhead}$	$bits$
Window Size	1397	1309	W_s	$frames$
Net Data Rate	1	1	R_{net}	$Gbps$
Link Distance	400	400	L	km
Propagation Delay	1.33	1.33	t_{prop}	ms
Transmission Time	1.912	2.04	t_s	μs

Table 6.5.: ARQ simulation parameters - with and without FEC

6.2.2.2. GBN-ARQ

The results presented in Figure 6.10 demonstrate the performance of GBN-ARQ with and without FEC. When FEC is not used, the transmission efficiency (TE) of GBN-ARQ performs poorly for

BEP values greater than 1E-07. The addition of FEC, on the other hand, results in a significant improvement, with the TE reaching its maximum value up to a mean BEP of 3E-04. The simulation results and analytical approximations differ at high BEP values. This is because the analytical equations used don't consider the losses of previously retransmitted frames, which can greatly affect performance at higher BEP values.

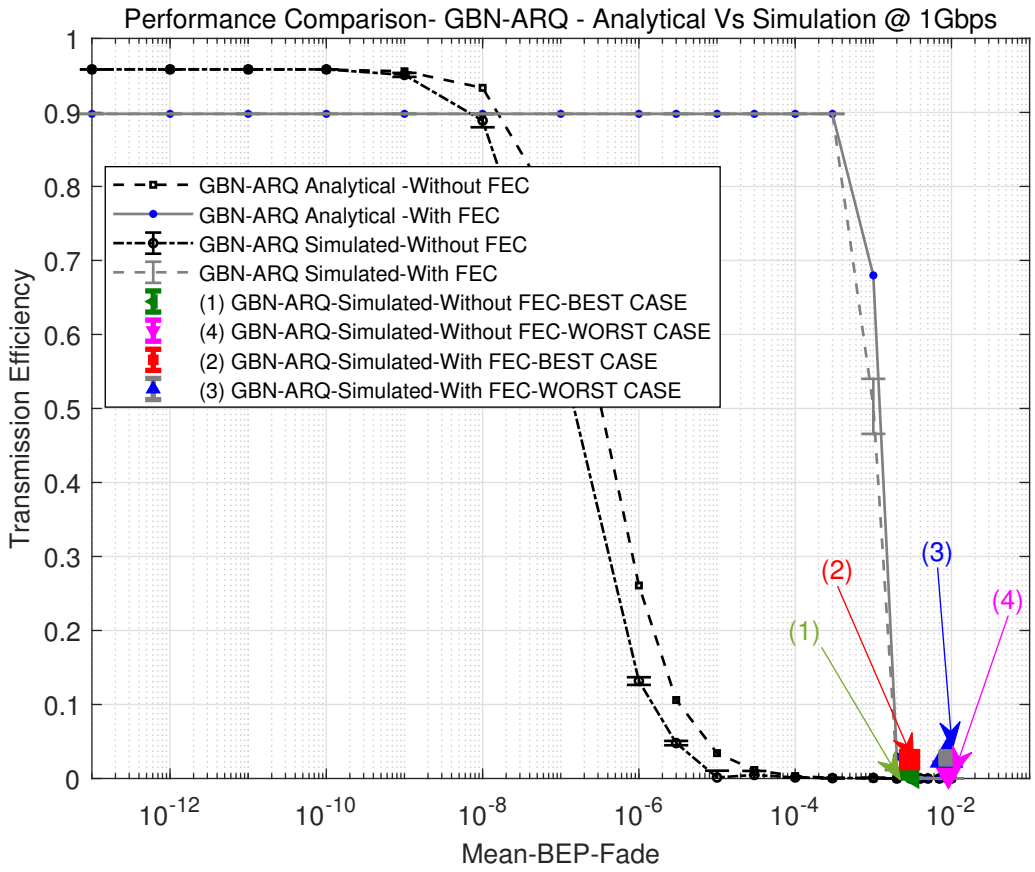

Figure 6.10.: GBN-ARQ performance analysis

Simulations were conducted for various constant BEP values in the best and worst-case inter-HAP scenarios outlined in Table 6.3. The mean BEP values were derived from time-varying BEP fade values discussed in Section 6.2.1.4, both with and without FEC. The resulting ARQ performance for these fading channels is depicted in Figure 6.10 and Figure 6.11, corresponding to the mean BEP of the fading channel. It is important to note that the figures include 95% confidence intervals for each value point, although these intervals may be difficult to observe in the graphs. Taking into account the simulation results and information from 6.2.1, it is important to note that GBN-ARQ struggles to recover within the range of BEP for both the best and worst-case channel scenarios, even when FEC is used. In the case of GBN, this limitation is due to the combination of high BEP values and the need to retransmit a large sender window. As a result, transmission efficiency falls to a few percent, as shown in Figure 6.10. The ARQ sender is overwhelmed by retransmissions as a result of this decline, negating GBN's cumulative ACK advantage.

6.2.2.3. SR-ARQ

The transmission efficiency (TE) of SR-ARQ is depicted in the results presented in Figure 6.11, showcasing different mean channel BEP fade values. The graph illustrates an enhancement in performance by combining FEC and ARQ, particularly at higher BEP values. While FEC incurs a trade-off in terms of reduced TE at lower mean BEP values, it offers advantages at higher mean BEP values. This observation aligns with the best and worst-case scenarios of the fading channel, which involve time-varying BEP values.

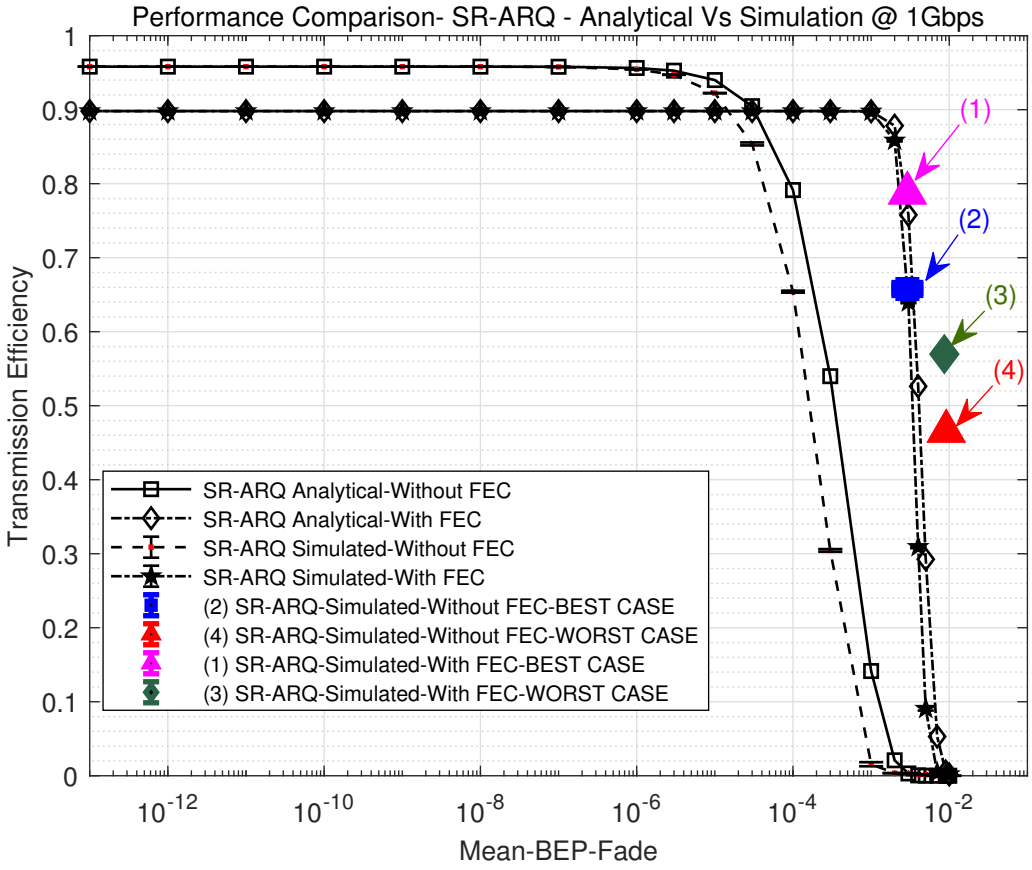

Figure 6.11.: SR-ARQ performance analysis

It is important to highlight that the differences observed between analytical approximations and simulation results at high Bit Error Probability (BEP) values arise from the exclusion of acknowledgment (ACK) losses in the backward channel within the approximation equations. This omission can significantly affect the performance evaluation, especially in challenging environments where communication reliability is critical. The lack of consideration for ACK losses means that the model may not accurately reflect the true conditions experienced during transmission, leading to discrepancies in predicted performance.

Additionally, the graph reveals a noteworthy finding: the transmission efficiency (TE) values for the best- and worst-case channel scenarios are approximately 80% and 57%, respectively. These scenarios involve turbulence-induced fading for the best-case scenario and pointing error-induced

fading for the worst-case scenario. These TE values are significantly higher than those obtained when using constant BEP values that correspond to the mean BEP of the fading channel. This suggests that periods of high BEP losses are balanced out by periods of lower losses, leading to an overall higher TE.

This observation indicates that the communication system can effectively manage periods of high error rates, which can be a valuable insight for optimizing the Automatic Repeat reQuest (ARQ) protocol. By leveraging these compensatory periods of performance, further enhancements could be made to improve the overall efficiency and robustness of the system under varying conditions. Such optimization efforts could lead to better utilization of resources and improved data transmission reliability, ultimately enhancing system performance in real-world applications.

This study aimed to compare the performance of two window-based Automatic Repeat reQuest (ARQ) protocols in an inter-High Altitude Platform (HAP) Free Space Optical (FSO) communication system using OMNET++ simulations. The simulation model accounted for turbulence-induced scintillation and fading caused by pointing errors. In terms of transmission efficiency, the Selective Repeat (SR)-ARQ protocol outperformed the Go-Back-N (GBN) protocol in both best-case and worst-case scenarios. The study also suggested strategies to improve ARQ system performance, such as adjusting the Forward Error Correction (FEC) strength based on the varying Bit Error Probability (BEP) of the channel and increasing the redundancy of ARQ acknowledgments in the reverse channel. These findings highlight the effectiveness of the ARQ protocol in inter-HAP FSO communication systems and offer promising directions for future research in developing a more intelligent ARQ system.

6.3. Evaluation of Adaptive Hybrid ARQ Performance with CSI-Based Code Rate Selection

This section focuses on the utilization of the Hybrid Automatic Repeat Request (HARQ) protocol in Free-Space Optical (FSO) systems to rectify transmission errors induced by fluctuating channel conditions. This research investigates the Transmission Efficiency (TE) of adaptive code rate HARQ, considering different qualities of Channel State Information (CSI) in inter-HAP (High Altitude Platform) scenarios. The CSI, which provides feedback regarding the receiver's power value, is employed to dynamically adjust the Reed-Solomon (RS) Forward Error Correction (FEC) code rate based on the fading behavior of the channel. Different types of CSI, including perfect, delayed, reciprocal, and fixed-mean, are considered in the investigation. The inter-HAP FSO channel is examined, specifically focusing on log-normal fading channels with varying link distances, fading strengths, and coherence times.

6.3.1. Inter-HAP FSO Scenario

Four scenarios are presented in Table 6.6 to investigate the impact of various channel state information (CSI) qualities on inter-HAP link scenarios. These scenarios are designed to investigate the

combined effect of atmospheric turbulence (PSI) and channel correlation time (τ), as indicated by the HWHM -3 dB drop in covariance function width. In these scenarios, the Power Scintillation Index (PSI), which quantifies the variance of normalized received power fluctuations [4], is used as a quantitative measure to assess the turbulence impact.

The goal of investigating various CSI qualities in these scenarios is to determine how the accuracy and timeliness of the received information affect the performance of the inter-HAP links. The study aims to capture variations in turbulence and channel correlation time, which are critical factors influencing FSO communication, by taking extreme link distances and the associated atmospheric conditions into account. The PSI is a useful metric for quantifying the effect of turbulence on signal quality, providing insights into the stability and reliability of inter-HAP links under various CSI qualities.

Scenario	**Link Distance** L **(km)**	**Round-Trip Time** RTT **(ms)**	**Channel Correlation Time** τ **(ms)**	ρ (RTT/τ) **(unitless)**	**Power Scintillation Index** PSI **(unitless)**
A.1	150	1	2	0.5	0.5
A.2			10	0.1	
B.1	900	6	2	3.0	1
B.2			10	0.6	

Table 6.6.: Scenario Description - Four different bi-directional Inter-HAP scenarios.

The information in Table 6.6 provides a basis for analyzing the results of the simulation experiments. It enables a thorough examination of the interaction between CSI qualities, atmospheric turbulence, and channel correlation time, providing valuable insights into the performance of FSO communication systems in a variety of scenarios.

6.3.2. Inter-HAP FSO Channel

In this study, the Hufnagel-Valley (H-V) model [4] is used to estimate the refractive index structure parameter C_n^2 in units of $m^{-2/3}$, which characterizes atmospheric turbulence. As a measure of the accuracy of the channel state information (CSI) obtained by the receiver, we introduce a metric, the ratio of round trip time (RTT) to half width at half maximum (HWHM). A higher value indicates that the CSI is more out of date. We generate time series of power vectors that correspond to the log-normal fading channel in our chosen inter-HAP scenarios to simulate the fading channel. The received power vectors for scenarios B.1 and B.2 at HAPs A and B are shown in Figure 6.12 (a) and Figure 6.12 (b). As discussed in Section 2.10, the Correlation Coefficient (CCF) [74] is used to measure the correlation between the two vectors and is represented by Eq. (2.20).This study

incorporates the effects of atmospheric turbulence and the timeliness of CSI in the analysis by using the Hufnagel-Valley model and introducing the RTT/HWHM ratio. The log-normal fading channel simulation allows for the investigation of the fading characteristics of the inter-HAP scenarios of interest.

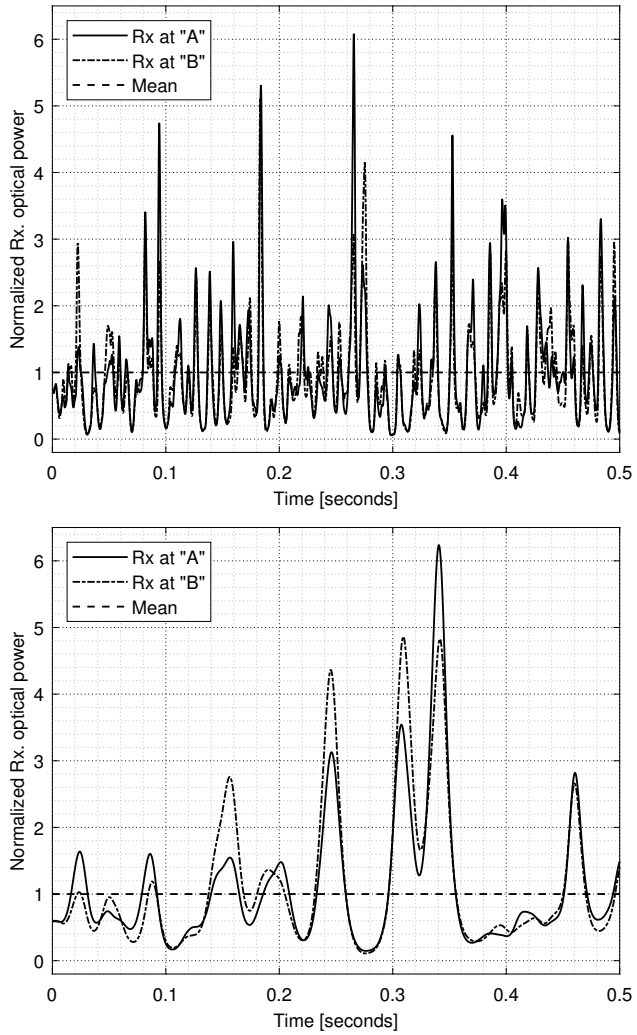

(a) Scenario B.1: CCF = 0.9, PSI = 1.0, τ = 2ms.

(b) Scenario B.2: CCF = 0.9, PSI = 1.0, τ = 10ms.

Figure 6.12.: First 500ms of the simulated vector.

The power vectors shown in Figure 6.12 (a) and Figure 6.12 (b) represent the received power fluctuations at HAPs A and B in the respective scenarios. These power vectors were generated using PILab simulations as detailed in Section 5.1.1.1.

The Correlation Coefficient (CCF) is used to quantify the correlation between these power vectors, which also serves as a measure of channel reciprocity. The study gains insight into the impact of atmospheric turbulence, CSI accuracy, and channel reciprocity on the performance of inter-HAP FSO communication by employing these modelling and simulation techniques. These insights are critical for understanding channel behavior and developing effective communication strategies in scenarios with varying levels of turbulence and CSI timeliness.

6.3.3. Evaluation Results

This section presents the simulation results evaluating the performance of the adaptive code-rate Hybrid Automatic Repeat Request (HARQ) protocol across various scenarios outlined in Table 6.6. Simulations were conducted using OMNeT++ [133] (see Section 5.2) to determine the transmission efficiency (TE), which measures the channel bit rate used for payload transmission. Performance scenarios were chosen from Table 6.6. Channel simulations for a non-reciprocal conventional channel were run using PILab (see Section 5.1.1.1), and the resulting received power vectors were fed into the OMNeT++ simulations, as shown in Figure 5.15. The Selective Repeat ARQ (SR-ARQ) scheme with adaptive code-rate control is detailed in Chapter 4. The simulations assumed a net data rate of 1 Gbps, a frame length of 255 bytes, and a transmission time of 2.04 μs (see Section 6.2.2.1). The receiver model employed an Avalanche Photo Detector (APD) with shot noise-limited slope and NRZ modulation, as described in Section 2.9.1. FEC code rates were adapted based on received power (P_{rx}) indicated by CSI (see Table 4.3). The highest achievable TE in a non-fading channel for various fixed FEC code rates is shown in Figure 4.3.

Figure 6.13 (a) and Figure 6.13 (b) depicts the TE performance for fading channels, with insets displaying TE ranging from 50% to 90%. Various scenarios were considered as depicted in Table 6.6, and the results demonstrated the effect of different CSI types on TE. R-CSI with CCF 1.0 and CCF 0.9 outperformed D-CSI and F-CSI in terms of TE in Scenario A.1, where the channel's RTT is low and the CSI is relatively up-to-date. The findings demonstrated the efficacy of using current CSI data to improve TE. The HWHM autocovariance (τ) is high when compared to the channel's RTT, resulting in a relatively low degree of outdatedness (=0.5 as described in Table 6.6) for the CSI. As a result, the CSI data is not too old and can still be used to improve TE, as demonstrated by the results.

In Scenario A.2 as depicted in Figure 6.13 (b), with a small CSI delay compared to the channel's autocovariance, P-CSI, R-CSI (CCF 1.0), and D-CSI all performed similarly in terms of TE performance for all mean received powers. Because of the decorrelation factor, R-CSI (CCF 0.9) had a lower TE. Furthermore, at a code rate of 1, F-CSI significantly improved TE performance over the ARQ-only implementation.

Scenario B.1 as depicted in Figure 6.14 (a) included a longer channel delay, which caused D-CSI and R-CSI (CCF 0.9 and 1.0) to become out of date in comparison to the channel's autocovariance. In this case, F-CSI outperformed the other CSI types in terms of TE, highlighting the benefit of using fixed-mean CSI for optimal code-rate selection. In Scenario B.2 as depicted in Figure 6.14 (b), R-CSI with a CCF of 1.0 outperformed TE starting at around 50 nW mean P_{rx}. F-CSI approached and eventually surpassed D-CSI in performance as mean P_{rx} increased.

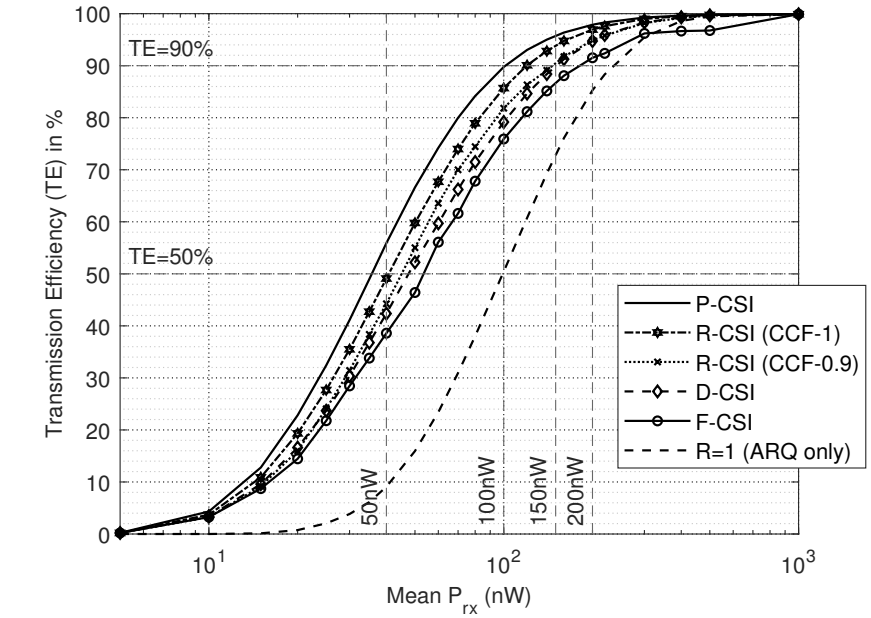

(a) Scenario A.1: L-150kms, RTT-1ms, τ-2ms, ρ-0.5, PSI-0.5.

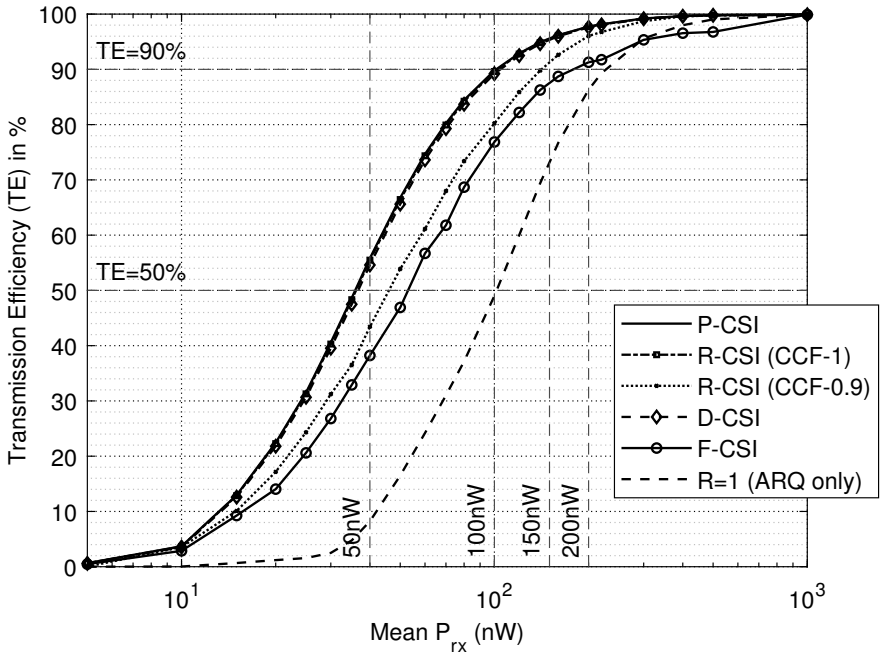

(b) Scenario A.2: L- 150kms, RTT-1ms, τ-10ms, ρ-0.1, PSI-0.5.

Figure 6.13.: Scenario A: Adaptive rate HARQ performance with CSI.

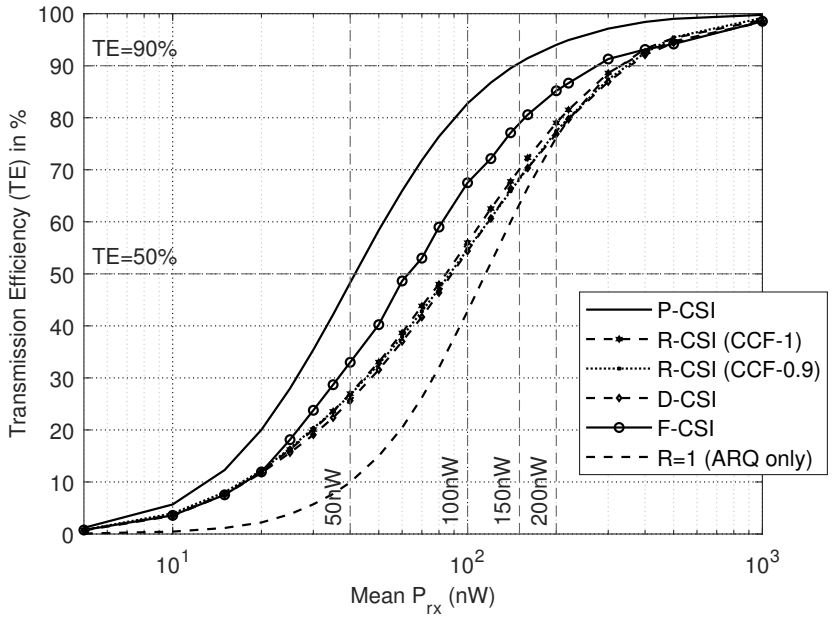

(a) Scenario B.1: L-900kms, RTT-6ms, τ-2ms, ρ-3.0, PSI-1.0.

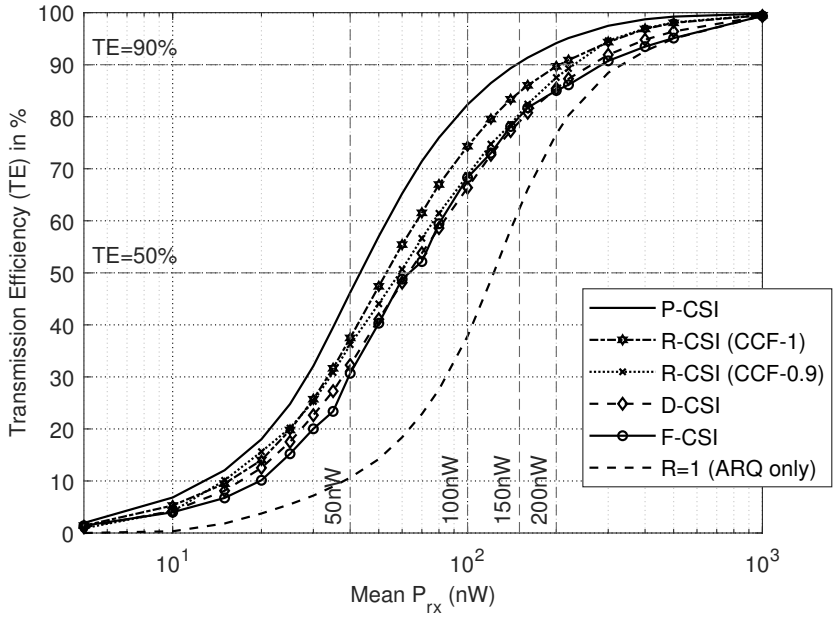

(b) Scenario B.2: L-900kms, RTT-6ms, τ-10ms, ρ-0.6, and PSI-1.0.

Figure 6.14.: Scenario B: Adaptive rate HARQ performance with CSI.

The coding gain obtained using Eq. (3.19) by the adaptive rate approach compared to ARQ (without RS-FEC) for transmission efficiencies of 90% and 50% is shown in tables Table 6.7 and Table 6.8, respectively. In Table 6.7, a negative gain is observed, which can be attributed to the reduction in transmission efficiency caused by the overhead associated with CSI. However, at higher mean received power (P_{rx}) values, this overhead becomes unnecessary.

Link Distance L **(km)**	**Correlation Time** τ **(ms)**	**Power Scintillation Index** *PSI* **(unitless)**	**Coding Gain (dB) for** $TE = 90\%$				
			P-CSI	**R-CSI (CCF=1)**	**R-CSI (CCF=0.9)**	**D-CSI**	**F-CSI**
150	2	0.5	3.61	2.82	2.15	1.71	0.71
	10		3.61	3.61	2.15	3.61	0.71
900	2	1	3.97	-0.3	-0.3	-0.3	0.96
	10		3.97	2.01	2.01	0.96	0.66

Table 6.7.: Coding gain for Adaptive Rate HARQ in the presence of Perfect (P-CSI), Reciprocal (R-CSI), Delayed (D-CSI), and Fixed Mean (F-CSI).

Note: The gain is between adaptive HARQ and ARQ only (no RS-FEC) for a TE of 90%.

The simulation results indicate that the adaptive code-rate HARQ protocol outperforms an uncoded, non-adaptive ARQ-only implementation in the presence of different CSI. The tables report positive coding gain values, demonstrating a significantly higher gain achieved by the adaptive approach. This highlights the effectiveness of employing adaptive code-rate selection based on CSI data to enhance system performance. It is important to consider that the gain obtained from the adaptive rate approach varies depending on the transmission efficiency. A higher transmission efficiency of 90% results in a positive gain, indicating an improvement in performance compared to an ARQ-only transmission. However, at 50% transmission efficiency, the gain becomes negative due to the impact of CSI overhead. This suggests that the adaptive rate approach is more advantageous when operating with higher transmission efficiencies.

Link Distance L **(km)**	**Correlation Time** τ **(ms)**	**Power Scintillation Index** *PSI* **(unitless)**	**Coding Gain (dB) for** $TE = 50\%$				
			P-CSI	**R-CSI (CCF=1)**	**R-CSI (CCF=0.9)**	**D-CSI**	**F-CSI**
150	2	0.5	4.20	3.76	3.01	3.18	2.59
	10		4.20	4.20	3.46	4.20	2.59
900	2	1	4.07	1.06	1.06	1.06	2.47
	10		4.77	3.89	3.52	3.17	3.17

Table 6.8.: Coding gain for Adaptive Rate HARQ in the presence of Perfect (P-CSI), Reciprocal (R-CSI), Delayed (D-CSI), and Fixed Mean (F-CSI).

Note: The gain is between adaptive HARQ and ARQ only (no RS-FEC) for a TE of 50%.

In conclusion, simulation results show that the adaptive code-rate HARQ protocol, utilizing RS-FEC and CSI-based rate adaptation, achieves significant coding gains compared to an uncoded, non-adaptive ARQ implementation. By selecting appropriate code rates based on CSI data, the overall efficiency and performance of the system are enhanced.

This section examined the impact of various types of channel state information (CSI) on the performance of adaptive hybrid automatic repeat request (HARQ) in optical inter-HAP links. The findings highlighted the critical role of high-quality CSI at the transmitter for optimal code rate adaptation and improved system performance. Simulations considered different fading strengths and flight time correlation times, using OMNeT++ software and transmission efficiency as performance metrics. The results indicate that transmission efficiency is improved with delayed, reciprocal, and fixed-mean CSI compared to uncoded, non-adaptive ARQ. Notably, reciprocity enhances system performance while eliminating the need for a perfect backward channel, which is essential for D-CSI. Future research may focus on predicting CSI at the transmitter to enhance efficiency in scenarios with longer channel delays.

6.4. Chapter Summary

The longest recorded ground-to-ground bidirectional Free-Space Optical (FSO) link has established reciprocity, revealing strong correlations in both experimental and numerical data. This reciprocity offers opportunities to mitigate signal scintillation caused by atmospheric turbulence. Adaptive techniques, enabled by real-time channel knowledge known as “reciprocal CSI,” allow for reduced retransmission time in multi-hop High Altitude Platform (HAP) systems compared to traditional Automatic Repeat reQuest (ARQ) protocols. The performance of different ARQ protocols and adaptive Hybrid Automatic Repeat reQuest (HARQ) schemes in inter-HAP FSO communication systems was evaluated in these studies. The results underscored the significance of channel state information, atmospheric turbulence, and pointing errors on system performance. The SR-ARQ protocol outperformed GBN-ARQ in terms of transmission efficiency, while adaptive rate HARQ outperformed uncoded ARQ. Delayed CSI and Reciprocal CSI were identified as substantial factors affecting system performance, and potential solutions such as CSI prediction and soft combining were proposed to enhance system efficiency. These studies provide valuable insights for the design and optimization of ARQ and HARQ schemes in inter-HAP FSO communication systems, and suggest promising avenues for future research.

7 | Conclusion and Outlook

This chapter provides a summary of the primary conclusions derived from the research conducted in this Ph.D. Thesis. It includes a general conclusion as well as an exploration of future research directions.

This Ph.D. thesis focused on improving the performance of inter-High Altitude Platform (HAP) Free-Space Optical (FSO) communications through the implementation of adaptive-rate hybrid automatic repeat request (HARQ) techniques and the utilization of channel state information (CSI).

FSO Inter-HAP Channel and Reciprocity Measurements

The effects of atmospheric conditions and static pointing errors on communication links have been analyzed. In a weak fluctuation regime, the scintillation index was modeled, and a lognormal fading channel was established. The RFE model was applied to the links, incorporating channel parameters into the link budgeting process. The principle of channel reciprocity was quantified, and channel simulations were performed for various scenarios, utilizing both conventional and reciprocal FSO channels with methods like PvGeT and PILab. The modeling of inter-HAP FSO channels proved to be more effective with these techniques. Additionally, the study targeted a long-range reciprocal FSO link distance of 62.86 km, involving experimental observations and numerical simulations across different FSO scenarios using the Matlab-based PILab tool.

Adaptive HARQ Analysis with CSI

The performance of SW-ARQ was found inadequate for this thesis, while GBN-ARQ, requiring a larger window size, is unsuitable for higher data rates. Its performance declines significantly at PEP values of 10^{-5} . This strongly supports the focus on SR-ARQ, particularly for FSO inter-HAP fading channels, as it efficiently avoids transmission gaps and unnecessary retransmissions of correctly received frames.

GBN-ARQ struggles to recover within the BEP range across best and worst-case channel scenarios, even with FEC, due to high BEP values and the need for large sender window retransmissions, which drastically reduces transmission efficiency. The sender becomes overwhelmed with retransmissions, negating the advantages of cumulative ACK. Notably, discrepancies between analytical approximations and simulation results at high BEP arise from excluding ACK losses in the backward channel, affecting performance evaluation under challenging conditions. The simulation graph indicates that TE values are approximately 80% for the best case and 57% for the worst case.

This thesis proposes a novel approach to managing various types of CSI by modifying the FEC code rate accordingly. It involves selecting the optimal code rate for each CSI type and optimizing it for the Receiver Front End (RFE). An adaptive code-rate selection look-up table aims to maximize transmission efficiency for each CSI type, integrated within the Selective Repeat (SR) ARQ mechanism. A comprehensive event-based selective repeat Hybrid Automatic Repeat reQuest (HARQ) model in OMNeT++ was presented. The event-based SR-ARQ simulation was merged with channel simulation to assess HARQ protocols for inter-HAP FSO links. The impact of different CSI types on the performance of adaptive HARQ was examined, highlighting the importance of high-quality CSI at the transmitter for optimal code rate adaptation and improved system performance. The simulations considered various fading strengths and correlation times,

utilizing OMNeT++ software, with transmission efficiency as the performance metric. Results indicated that using delayed, reciprocal, and fixed-mean CSI improves transmission efficiency compared to uncoded, non-adaptive ARQ. This reciprocity enhances system performance and mitigates the need for a perfect backward channel, a prerequisite for D-CSI. Future work may explore CSI prediction at the transmitter to enhance efficiency for longer channel delays.

Simulation results demonstrate that the adaptive code-rate HARQ protocol outperforms uncoded, non-adaptive ARQ when different CSI types are present. Positive coding gain values reveal a significant advantage of the adaptive method. The effectiveness of adaptive code-rate selection based on CSI data is crucial for system performance. However, the gain from this approach varies with transmission efficiency; a higher efficiency of 90% yields positive gains, while at 50%, gains can turn negative due to CSI overhead. This suggests that adaptive rate strategies are most beneficial at higher transmission efficiencies. In summary, the simulation results of the adaptive code-rate HARQ protocol, which utilizes RS-FEC and CSI-based rate adaptation, demonstrate a significant coding gain over uncoded, non-adaptive ARQ. Choosing appropriate code rates based on CSI data enhances overall system efficiency and performance.

In Section 1.4, the research questions were proposed, and the findings and conclusions resulting from the research are presented in alignment with those research questions as follows:

- **Determining Channel Impairments and Scenario Refinement:** Impairments such as atmospheric turbulence and static pointing errors impacting inter-HAP FSO links were identified and modeled in this thesis, with a focus on weak atmospheric turbulence fluctuations. Valuable insights into the structure and challenges of inter-HAP FSO communication systems were provided by this research, with emphasis placed on the importance of sensitivity, link budget, and performance measures such as Q-factor and OSNR. These insights are expected to benefit the development of future HAP-based communication systems.

- **Exploiting Reciprocal Behavior in Bidirectional FSO Channels for Enhanced Performance Efficiency:** Channel reciprocity in bidirectional FSO channels was investigated in this research to enhance efficiency, with proof presented that low-delay CSI can be used by transmitters to manage adaptive link errors. The presence of strong reciprocity in inter-HAP FSO links, was demonstrated in this research. This reciprocity offers opportunities for error control amidst atmospheric turbulence. The study enabled adaptive link error control through the utilization of reciprocal CSI, resulting in enhanced system performance and reduced retransmission time. This research also highlighted the importance of high-quality CSI at the transmitter for optimal code rate adaptation and overall system performance. Promising results were observed for reciprocal and fixed-mean CSI, while uncoded non-adaptive ARQ was found to be less efficient. The use of reciprocity eliminated the need for a perfect backward channel.

- **Choosing Suitable HARQ Technology and Dynamic Code Rate Adaptation Using CSI to Boost Performance and Address Inter-HAP FSO Channel Impairments:** This study supports the use of HARQ, adaptive Reed-Solomon code-rate techniques, and various types

of CSI to improve performance and address inter-HAP FSO link impairments. An OMNET++ simulation model was introduced to demonstrate this strategy. The research focused on modeling and simulating symmetrical inter-HAP FSO links under various scenarios. Critical factors in designing effective ARQ schemes were identified as fading behavior and identical error rates in forward and backward channels. The study found that adaptive-rate HARQ with appropriate window and packet sizes significantly enhanced transmission efficiency. Additionally, this research provided an overview of how CSI, particularly reciprocal CSI, can improve HARQ performance. The importance of adapting HARQ schemes in the absence of perfect CSI was underscored, and the benefits of reciprocal CSI in enhancing system performance and transmission efficiency were highlighted.

In conclusion, this research contributes to the progression of inter-HAP FSO communication systems by demonstrating the effectiveness of adaptive-rate HARQ techniques and the use of reciprocal CSI. The significance of adaptive transmission schemes and accurate channel estimation in mitigating the impact of channel impairments was underscored by the findings. Future research directions include the exploration of advanced HARQ techniques and the evaluation of system performance in realistic scenarios.

A Publications

1. S. Parthasarathy, D. Giggenbach, and A. Kirstädter “Channel modelling for free-space optical inter-HAP links using adaptive ARQ transmission,” Proc. SPIE 9248, Unmanned/Unattended Sensors and Sensor Networks X, 92480Q (17 October 2014); https://doi.org/10.1117/12.2067195

2. S. Parthasarathy, A. Kirstaedter and D. Giggenbach, “Simulative Performance Analysis of ARQ Schemes for Free-Space Optical Inter-HAP Channel Model,” Photonic Networks; 16. ITG Symposium, Leipzig, Germany, 2015, pp. 1-5.

3. S. Parthasarathy, A. Kirstaedter and D. Giggenbach, “Performance Analysis of Adaptive Hybrid ARQ for Inter-HAP Free-Space Optical Fading Channel with Delayed Channel State Information,” Photonic Networks; 17. ITG-Symposium; Proceedings of, Leipzig, Germany, 2016, pp. 1-7.

4. S. Parthasarathy, A. Kirstaedter and D. Giggenbach, “Adaptive HARQ with Channel State Information in Inter-HAP FSO Links,” Photonic Networks; 18. ITG-Symposium, Leipzig, Germany, 2017, pp. 1-6.

5. S. Parthasarathy, D. Giggenbach, R. Barrios, C. Fuchs and A. Kirstädter, “Simulative verification of channel reciprocity in free-space optical inter-HAP links,” 2017 IEEE International Conference on Space Optical Systems and Applications (ICSOS), Naha, Japan, 2017, pp. 154-159, doi: 10.1109/ICSOS.2017.8357227.

6. D. Giggenbach, S. Parthasarathy, A. Shrestha, F. Moll and R. Mata-Calvo, “Power vector generation tool for free-space optical links - PVGeT,” 2017 IEEE International Conference on Space Optical Systems and Applications (ICSOS), Naha, Japan, 2017, pp. 160-165, doi: 10.1109/ICSOS.2017.8357228.

7. S. Parthasarathy, D. Giggenbach, C. Fuchs, R. Mata-Calvo, R. Barrios and A. Kirstaedter, “Verification of Channel Reciprocity in Long-Range Turbulent FSO Links,” Photonic Networks; 19th ITG-Symposium, Leipzig, Germany, 2018, pp. 1-6.

Bibliography

[1] H. Henniger and O. Wilfert, "An introduction to free-space optical communications," *Radioengineering*, vol. 19, pp. 203–212, 2010.

[2] A. Majumdar and J. Ricklin, *Free-Space Laser Communications: Principles and Advances*, ser. Optical and Fiber Communications Reports. Springer New York, 2010. [Online]. Available: https://books.google.de/books?id=-wj39a3oTecC

[3] H. Kaushal and G. Kaddoum, "Optical communication in space: Challenges and mitigation techniques," *IEEE Communications Surveys Tutorials*, vol. 19, no. 1, pp. 57–96, Firstquarter 2017.

[4] L. Andrews and R. Phillips, *Laser Beam Propagation Through Random Media*, ser. SPIE Press monograph. Society of Photo Optical, 2005. [Online]. Available: https://books.google.de/books?id=4NXHYg70qqIC

[5] D. Giggenbach, R. Purvinskis, M. Werner, and M. Holzbock, "Stratospheric optical interplatform links for high altitude platforms," in *20th AIAA International Communications Satellite Systems Conference (ICSSC 2002), 2002-5-12 - 2002-5-15, Montreal, Canada*, 2002.

[6] S. Milner, S. Trisno, C. Davis, B. Epple, and H. Henniger, "A cross-layer approach to mitigate fading on bidirectional free space optical communication links," in *Military Communications Conference, 2008. MILCOM 2008. IEEE*, Nov 2008, pp. 1–6.

[7] F. Fidler, M. Knapek, J. Horwath, and W. R. Leeb, "Optical communications for high-altitude platforms," *IEEE Journal of Selected Topics in Quantum Electronics*, vol. 16, no. 5, pp. 1058–1070, Sept 2010.

[8] M. Alzenad, M. Z. Shakir, H. Yanikomeroglu, and M. S. Alouini, "Fso-based vertical backhaul/fronthaul framework for 5G+ wireless networks," *CoRR*, vol. abs/1607.01472, 2016. [Online]. Available: http://arxiv.org/abs/1607.01472

[9] T. Kapsis and A. Panagopoulos, "Power allocation for reliable and energy-efficient optical leo-to-ground downlinks with hybrid arq schemes," *Photonics*, vol. 9, p. 92, 02 2022.

[10] D. L. Fried, "Statistics of laser beam fade induced by pointing jitter," *Appl. Opt.*, vol. 12, no. 2, pp. 422–423, Feb 1973. [Online]. Available: http://ao.osa.org/abstract.cfm?URI=ao-12-2-422

[11] M. Safari, M. M. Rad, and M. Uysal, "Multi-hop relaying over the atmospheric poisson channel: outage analysis and optimization," *IEEE Transactions on Communications*, vol. 60, no. 3, pp. 817–829, March 2012.

[12] Vuong V. Mai and Hoon Kim, "Mitigation of effects of angle-of-arrival fluctuation and pointing error on airborne free-space optical systems," in *Optical Fiber Communication Conference (OFC) 2019*. Optical Society of America, 2019, p. W2A.40. [Online]. Available: http://www.osapublishing.org/abstract.cfm?URI=OFC-2019-W2A.40

[13] T. C. Tozer and D. Grace, "High-altitude platforms for wireless communications," *Electronics Communication Engineering Journal*, vol. 13, no. 3, pp. 127–137, Jun 2001.

[14] P. Pace, G. Aloi, F. De Rango, E. Natalizio, A. Molinaro, and S. Marano, "An integrated satellite-hap-terrestrial system architecture: resources allocation and traffic management issues," in *2004 IEEE 59th Vehicular Technology Conference. VTC 2004-Spring (IEEE Cat. No.04CH37514)*, vol. 5, 2004, pp. 2872–2875 Vol.5.

[15] G. Avdikos, G. Papadakis, and N. Dimitriou, "Overview of the application of high altitude platform (hap) systems in future telecommunication networks," in *2008 10th International Workshop on Signal Processing for Space Communications*, 2008, pp. 1–6.

[16] A. Aragón-Zavala, J. L. Cuevas-Ruíz, and J. A. Delgado-Penín, *High-Altitude Platforms for Wireless Communications*, 09 2008.

[17] *FSO in HAP-Based Communication Systems*. John Wiley & Sons, Ltd, 2010, ch. 7, pp. 219–238. [Online]. Available: https://onlinelibrary.wiley.com/doi/abs/10.1002/9780470971840.ch7

[18] F. D'Oliveira, F. Melo, and T. Devezas, "High-altitude platforms - present situation and technology trends," *Journal of Aerospace Technology and Management*, vol. 8, pp. 249–262, 08 2016.

[19] "Could high-altitude pseudo-satellites transform the space industry?" Nov. 2018. [Online]. Available: https://www.esa.int/Enabling_Support/Preparing_for_the_Future/Discovery_and_Preparation/Could_High-Altitude_Pseudo-Satellites_Transform_the_Space_Industry

[20] A. Mohammed, A. Mehmood, F. N. Pavlidou, and M. Mohorcic, "The role of high-altitude platforms (haps) in the global wireless connectivity," *Proceedings of the IEEE*, vol. 99, no. 11, pp. 1939–1953, Nov 2011.

[21] M. Sharma, D. Chadha, and V. Chandra, "High-altitude platform for free-space optical communication: performance evaluation and reliability analysis," *IEEE/OSA Journal of Optical Communications and Networking*, vol. 8, no. 8, pp. 600–609, Aug 2016.

[22] N. Nomikos, E. Michailidis, P. Bithas, D. Vouyioukas, and A. Kanatas, "Optimal relay location and oppurtunistic user-scheduling for stratospheric communications," 03 2018.

[23] E. T. Michailidis, N. Nomikos, P. S. Bithas, D. Vouyioukas, and A. G. Kanatas, "Outage probability of triple-hop mixed RF / FSO/ RF stratospheric communication systems," 2018. [Online]. Available: https://api.semanticscholar.org/CorpusID:201048577

[24] "Google loon project," https://x.company/projects/loon/;https://x.company/projects/loon/the-loon-collection/, 2021, accessed: 2021-10-05.

[25] B. Moision, B. Erkmen, E. Keyes, T. Belt, O. Bowen, D. Brinkley, P. Csonka, M. Eglington, A. Kazmierski, N.-h. Kim, J. Moody, T. Tu, and W. Vermeer, "Demonstration of free-space optical communication for long-range data links between balloons on project loon," pp. 100 960Z–100 960Z–14, 2017. [Online]. Available: http://dx.doi.org/10.1117/12.2253099

[26] "Facebook aquila uav," October 2020, accessed: 2021-10-05. [Online]. Available: https://www.technologyreview.com/2015/07/30/166908/meet-facebooks-stratospheric-internet-drone

[27] C. E. Shannon, "A mathematical theory of communication," *Bell System Technical Journal*, vol. 27, no. 3, pp. 379–423, 1948. [Online]. Available: https://onlinelibrary.wiley.com/doi/abs/10.1002/j.1538-7305.1948.tb01338.x

[28] Wicker, Stephen B., *Error Control Systems for Digital Communication and Storage*. Upper Saddle River, NJ, USA: Prentice-Hall, Inc., 1995.

[29] R. Comroe and D. Costello, "Arq schemes for data transmission in mobile radio systems," *IEEE Journal on Selected Areas in Communications*, vol. 2, no. 4, pp. 472–481, July 1984.

[30] S. Falahati and A. Svensson, "Hybrid type-ii arq schemes with adaptive modulation systems for wireless channels," in *Gateway to 21st Century Communications Village. VTC 1999-Fall. IEEE VTS 50th Vehicular Technology Conference (Cat. No.99CH36324)*, vol. 5, Sep. 1999, pp. 2691–2695 vol.5.

[31] S. Choi and K. Shin, "A class of adaptive hybrid arq schemes for wireless links," *IEEE Transactions on Vehicular Technology*, vol. 50, no. 3, pp. 777–790, 2001.

[32] Y. Guo, *Advances in mobile radio access networks*. Artech House mobile communications library, 2004.

[33] A. Ahmed, A. Al-Dweik, Y. Iraqi, H. Mukhtar, M. Naeem, and E. Hossain, "Hybrid automatic repeat request (harq) in wireless communications systems and standards: a contemporary survey," *IEEE Communications Surveys & Tutorials*, vol. 23, no. 4, pp. 2711–2752, 2021.

[34] Leon-Garcia, Alberto and Widjaja, Indra, *Communication networks: fundamental concepts and key architectures*, 1st ed. McGraw-Hill School Education Group, 1999.

[35] *Channel modelling for free-space optical inter-HAP links using adaptive ARQ transmission*, vol. 9248, 2014. [Online]. Available: https://elib.dlr.de/90814/

[36] S. Parthasarathy, A. Kirstaedter, and D. Giggenbach, "Simulative performance analysis of arq schemes for free-space optical inter-hap channel model," in *Photonic Networks; 16. ITG Symposium*, 2015, pp. 1–5.

[37] S. Parthasarathy and A. Kirstaedter and D. Giggenbach, "Performance analysis of adaptive hybrid ARQ for inter-HAP free-space optical fading channel with delayed channel state information," in *Photonic Networks; 17. ITG-Symposium; Proceedings of*, May 2016, pp. 1–7. [Online]. Available: https://elib.dlr.de/103654/

[38] D. Giggenbach, S. Parthasarathy, A. Shrestha, F. Moll, and R. Mata-Calvo, "Power vector generation tool for free-space optical links - pvget," in *2017 IEEE International Conference on Space Optical Systems and Applications (ICSOS)*, Nov 2017, pp. 160–165. [Online]. Available: https://elib.dlr.de/115714/

[39] S. Parthasarathy, A. Kirstaedter, and D. Giggenbach, "Adaptive HARQ with channel state information in inter-hap fso links," in *Photonic Networks; 18. ITG-Symposium*, May 2017, pp. 1–6. [Online]. Available: https://elib.dlr.de/112384/

[40] S. Parthasarathy and D. Giggenbach and R. Barrios and C. Fuchs and A. Kirstaedter, "Simulative verification of channel reciprocity in free-space optical inter-HAP links," in *2017 IEEE International Conference on Space Optical Systems and Applications (ICSOS)*, Nov 2017, pp. 154–159.

[41] S. Parthasarathy, D. Giggenbach, C. Fuchs, R. Mata-Calvo, R. Barrios, and A. Kirstaedter, "Verification of channel reciprocity in long-range turbulent FSO links," in *Photonische Netze*, ser. Photonische Netze. VDE-Verlag GMBH, Berlin, June 2018, pp. 35–40. [Online]. Available: https://elib.dlr.de/120421/

[42] L. C. Andrews, R. L. Phillips, R. Crabbs, D. Wayne, T. Leclerc, and P. Sauer, "Atmospheric channel characterization for ORCA testing at NTTR," pp. 758 809–758 809–12, 2010. [Online]. Available: http://dx.doi.org/10.1117/12.842441

[43] L. Andrews, R. Phillips, and C. Hopen, *Laser Beam Scintillation with Applications*, ser. SPIE Press monograph. Society of Photo Optical, 2001. [Online]. Available: https://books.google.de/books?id=f8Kf4l88T04C

[44] Ammar Al-Habash,Larry C. Andrews,R. L. Phillips, "Mathematical model for the irradiance probability density function of a laser beam propagating through turbulent media," *Optical Engineering*, vol. 40, no. 8, pp. 1554 – 1562 – 9, 2001. [Online]. Available: https://doi.org/10.1117/1.1386641

[45] M. Toyoshima, H. Takenaka, and Y. Takayama, "Atmospheric turbulence-induced fading channel model for space-to-ground laser communications links," *Opt. Express*, vol. 19, no. 17, pp. 15 965–15 975, Aug 2011. [Online]. Available: http://www.opticsexpress.org/abstract.cfm?URI=oe-19-17-15965

[46] J. H. Shapiro, "Reciprocity of the turbulent atmosphere," *J. Opt. Soc. Am.*, vol. 61, no. 4, pp. 492–495, Apr 1971. [Online]. Available: http://www.osapublishing.org/abstract.cfm?URI=josa-61-4-492

[47] D. Giggenbach, W. Cowley, K. Grant, and N. Perlot, "Experimental verification of the limits of optical channel intensity reciprocity," *Appl. Opt.*, vol. 51, no. 16, pp. 3145–3152, Jun 2012. [Online]. Available: http://ao.osa.org/abstract.cfm?URI=ao-51-16-3145

[48] Frederick G. Smith, *The Infrared & Electro-Optical Systems Handbook, Volume 2: Atmospheric Propagation of Radiation*, 2nd ed. SPIE-Press, 1996.

[49] *Radio Mobile - RF propagation simulation software*, 2018 (accessed June 29, 2018). [Online]. Available: http://radiomobile.pe1mew.nl/?Calculations:Propagation_calculation:Fresnel_zones

[50] J. Strohbehn and S. Clifford, *Laser beam propagation in the atmosphere*, ser. Topics in applied physics. Springer-Verlag, 1978. [Online]. Available: https://books.google.de/books?id=UsfvAAAAIAAJ

[51] S. D. Lyke, D. G. Voelz, and M. C. Roggemann, "Probability density of aperture-averaged irradiance fluctuations for long range free space optical communication links," *Appl. Opt.*, vol. 48, no. 33, pp. 6511–6527, Nov 2009. [Online]. Available: http://ao.osa.org/abstract.cfm?URI=ao-48-33-6511

[52] D. Giggenbach and F. Moll, "Scintillation loss in optical low earth orbit data downlinks with avalanche photodiode receivers," *2017 IEEE International Conference on Space Optical Systems and Applications (ICSOS)*, pp. 115–122, 2017. [Online]. Available: https://api.semanticscholar.org/CorpusID:13707246

[53] L. C. A. R. L. Phillips and C. Y. Hopen, "Aperture averaging of optical scintillations: power fluctuations and the temporal spectrum," *Waves in Random Media*, vol. 10, no. 1, pp. 53–70, 2000. [Online]. Available: https://doi.org/10.1088/0959-7174/10/1/305

[54] D. L. Fried, "Aperture averaging of scintillation," *J. Opt. Soc. Am.*, vol. 57, no. 2, pp. 169–175, Feb 1967. [Online]. Available: http://www.osapublishing.org/abstract.cfm?URI=josa-57-2-169

[55] James H. Churnside, "Aperture averaging of optical scintillations in the turbulent atmosphere," *Appl. Opt.*, vol. 30, no. 15, pp. 1982–1994, May 1991. [Online]. Available: http://ao.osa.org/abstract.cfm?URI=ao-30-15-1982

[56] F. S. Vetelino, C. Young, L. Andrews, and J. Recolons, "Aperture averaging effects on the probability density of irradiance fluctuations in moderate-to-strong turbulence," *Appl. Opt.*, vol. 46, no. 11, pp. 2099–2108, Apr 2007. [Online]. Available: http://ao.osa.org/abstract.cfm?URI=ao-46-11-2099

[57] F. S. Vetelino, C. Young, and L. Andrews, "Fade statistics and aperture averaging for gaussian beam waves in moderate-to-strong turbulence," *Appl. Opt.*, vol. 46, no. 18, pp. 3780–3789, Jun 2007. [Online]. Available: http://ao.osa.org/abstract.cfm?URI=ao-46-18-3780

[58] Larry C. Andrews, "Aperture-averaging factor for optical scintillations of plane and spherical waves in the atmosphere," *J. Opt. Soc. Am. A*, vol. 9, no. 4, pp. 597–600, Apr 1992. [Online]. Available: http://josaa.osa.org/abstract.cfm?URI=josaa-9-4-597

[59] M. Toyoshima and K. Araki, "Effects of time averaging on optical scintillation in a ground-to-satellite atmospheric propagation," *Appl. Opt.*, vol. 39, no. 12, pp. 1911–1919, Apr 2000. [Online]. Available: http://ao.osa.org/abstract.cfm?URI=ao-39-12-1911

[60] M. Toyoshima, T. Jono, K. Nakagawa, and A. Yamamoto, "Optimum divergence angle of a gaussian beam wave in the presence of random jitter in free-space laser communication systems," *J. Opt. Soc. Am. A*, vol. 19, no. 3, pp. 567–571, Mar 2002. [Online]. Available: http://josaa.osa.org/abstract.cfm?URI=josaa-19-3-567

[61] A. A. Farid and S. Hranilovic, "Outage capacity optimization for free-space optical links with pointing errors," *J. Lightwave Technol.*, vol. 25, no. 7, pp. 1702–1710, Jul 2007. [Online]. Available: http://jlt.osa.org/abstract.cfm?URI=jlt-25-7-1702

[62] A. Mustafa, D. Giggenbach, J. Poliak, and S. T. Brink, "Quantifying the effect of atmospherically-induced pointing errors in optical geostationary satellite feeder links using transmitter diversity," in *2017 IEEE International Conference on Space Optical Systems and Applications (ICSOS)*, Nov 2017, pp. 272–277.

[63] V. V. Mai and H. Kim, "Adaptive beam control techniques for airborne free-space optical communication systems," *Appl. Opt.*, vol. 57, no. 26, pp. 7462–7471, Sep 2018. [Online]. Available: http://ao.osa.org/abstract.cfm?URI=ao-57-26-7462

[64] F. David, D. Giggenbach, H. Henniger, J. Horwath, R. Landrock, and N. Perlot, "Design considerations for optical inter-hap links," in *Proceedings ICSSC 2004. 22nd AIAA International Communications Satellite Systems Conference & Exhibit 2004 (ICSSC), Monterey, CA, May 9-12, 2004, Monterey, CA.*, 2004.

[65] H. Sandalidis, T. Tsiftsis, G. Karagiannidis, and M. Uysal, "BER performance of FSO links over strong atmospheric turbulence channels with pointing errors," *Communications Letters, IEEE*, vol. 12, pp. 44 – 46, 02 2008.

[66] G. P. Agrawal, *Fiber-optic communication systems*, 3rd ed. New York : Wiley-Interscience, 2002, vol. Volume 1. [Online]. Available: https://books.google.de/books/about/Fiber_optic_communication_systems.html?id=NfhSAAAAMAAJ&redir_esc=y

[67] P. J. Winzer, *Optical Transmitters, Receivers, and Noise*. John Wiley & Sons, Ltd, 2003. [Online]. Available: https://onlinelibrary.wiley.com/doi/abs/10.1002/0471219282.eot404

[68] D. Giggenbach and R. Mata-Calvo, "Sensitivity modeling of binary optical receivers," *Appl. Opt.*, vol. 54, no. 28, pp. 8254–8259, Oct 2015. [Online]. Available: http://ao.osa.org/abstract.cfm?URI=ao-54-28-8254

[69] J. Minet, M. A. Vorontsov, E. Polnau, and D. Dolfi, "Enhanced correlation of received power-signal fluctuations in bidirectional optical links," *Journal of Optics*, vol. 15, no. 2, p. 022401, 2013. [Online]. Available: http://stacks.iop.org/2040-8986/15/i=2/a=022401

[70] Z. Kolka, V. Biolkova, O. Wilfert, and D. Biolek, "Simulation model of correlated fso channels," in *2015 Conference on Microwave Techniques (COMITE)*, April 2015, pp. 1–4.

[71] R. R. Parenti, S. Michael, J. M. Roth, and T. M. Yarnall, "Comparisons of Cn2 measurements and power-in-fiber data from two long-path free-space optical communication experiments," pp. 78 140Z–78 140Z–9, 2010. [Online]. Available: http://dx.doi.org/10.1117/12.864256

[72] R. R. Parenti, J. M. Roth, J. Shapiro, and F. G. Walther, "Observations of channel reciprocity in optical free-space communications experiments," in *Imaging and Applied Optics*. Optical Society of America, 2011, p. LTuD3. [Online]. Available: http://www.osapublishing.org/abstract.cfm?URI=LSC-2011-LTuD3

[73] R. R. Parenti, J. M. Roth, J. H. Shapiro, F. G. Walther, and J. A. Greco, "Experimental observations of channel reciprocity in single-mode free-space optical links," *Opt. Express*, vol. 20, no. 19, pp. 21 635–21 644, Sep 2012. [Online]. Available: http://www.opticsexpress.org/abstract.cfm?URI=oe-20-19-21635

[74] L. Mandel and E. Wolf, *Optical Coherence and Quantum Optics*. Cambridge University Press, 1995. [Online]. Available: https://books.google.de/books?id=dVYhAwAAQBAJ

[75] Z. Wang and A. C. Bovik, "Mean squared error: love it or leave it? a new look at signal fidelity measures," *IEEE Signal Processing Magazine*, vol. 26, no. 1, pp. 98–117, Jan 2009.

[76] N. Perlot and D. Giggenbach, "Scintillation correlation between forward and return spherical waves," *Appl. Opt.*, vol. 51, no. 15, pp. 2888–2893, May 2012. [Online]. Available: http://ao.osa.org/abstract.cfm?URI=ao-51-15-2888

[77] W. Ryan and S. Lin, *Channel Codes: Classical and Modern*. Cambridge University Press, 2009. [Online]. Available: https://books.google.de/books?id=0gwqxBU_t-QC

[78] D. J. Costello and J. Hagenauer and H. Imai and S. B. Wicker, "Applications of error-control coding," *IEEE Transactions on Information Theory*, vol. 44, no. 6, pp. 2531–2560, Oct 1998.

[79] S. Lin and D. J. Costello, *Error Control Coding*. Prentice-Hall, 2004.

[80] T. K. Moon, *Error Correction Coding: Mathematical Methods and Algorithms*. New York, NY, USA: Wiley-Interscience, 2005.

[81] R. L. Freeman, *Forward Error Correction*. John Wiley & Sons, Ltd, 2002. [Online]. Available: https://onlinelibrary.wiley.com/doi/abs/10.1002/0471208051.fre023

[82] W. W. Peterson and D. T. Brown, "Cyclic codes for error detection," *Proceedings of the IRE*, vol. 49, no. 1, pp. 228–235, Jan 1961.

[83] E. J. W. W. Wesley Peterson, *Error-Correcting Codes*, 2nd ed. MIT Press, 1972.

[84] D. J. C. MacKay, *Information Theory, Inference, and Learning Algorithms*. New York, NY, USA: Cambridge University Press, 2002.

[85] B. Sklar, *Digital Communications: Fundamentals and Applications*, 2nd ed. Prentice Hall, 11th January 2001.

[86] S. Bernard and H. F.J., "The ABCs of linear block codes," *Signal Processing Magazine, IEEE*, vol. 21, pp. 14 – 35, 08 2004.

[87] V. Chan, "Coding for the turbulent atmospheric optical channel," *IEEE Transactions on Communications*, vol. 30, no. 1, pp. 269–275, January 1982.

[88] X. Zhu and J. M. Kahn, "Free-space optical communication through atmospheric turbulence channels," *IEEE Transactions on Communications*, vol. 50, no. 8, pp. 1293–1300, Aug 2002.

[89] I. B. Djordjevic, "Adaptive modulation and coding for free-space optical channels," *IEEE/OSA Journal of Optical Communications and Networking*, vol. 2, no. 5, pp. 221–229, May 2010.

[90] A. Viterbi, "Convolutional codes and their performance in communication systems," *IEEE Transactions on Communication Technology*, vol. 19, no. 5, pp. 751–772, October 1971.

[91] C.E. Shannon and R.G. Gallager and E.R. Berlekamp, "Lower bounds to error probability for coding on discrete memoryless channels," *Information and Control*, vol. 10, no. 1, pp. 65 – 103, 1967. [Online]. Available: http://www.sciencedirect.com/science/article/pii/S0019995867900526

[92] Wicker, Stephen B., *Reed-solomon codes and their applications*. Piscataway, NJ, USA: IEEE Press, 1994.

[93] I. Reed and G. Solomon, "Polynomial codes over certain finite fields," *Journal of the Society of Industrial and Applied Mathematics*, vol. 8, no. 2, p. 300–304, 06/1960 1960. [Online]. Available: http://www.jstor.org/pss/2098968

[94] J. G. Andrews, A. Ghosh, and R. Muhamed, *Fundamentals of wimax: understanding broadband wireless networking*. Upper Saddle River, NJ, USA: Prentice Hall PTR, 2007.

[95] Z. Zhao, R. Liao, S. D. Lyke, and M. C. Roggemann, "Reed-solomon coding for free-space optical communications through turbulent atmosphere," in *2010 IEEE Aerospace Conference*, 2010, pp. 1–12.

[96] S. S. Muhammad, T. Javornik, I. Jelovcan, E. Leitgeb, and O. Koudelka, "Reed solomon coded PPM for terrestrial FSO links," in *2007 International Conference on Electrical Engineering*, 2007, pp. 1–5.

[97] S. Kumar, D. Sharma, and A. Payal, "Performance enhancement of multi channel multi beam FSO communication link with the application of reed solomon codes," *Optical and Quantum Electronics*, vol. 54, 09 2022.

[98] A. Aspreas and K. Yiannopoulos, "Reed solomon error correction in pre-amplified pulse position modulation receivers," *AEU - International Journal of Electronics and Communications*, vol. 175, p. 154859, 2024. [Online]. Available: https://www.sciencedirect.com/science/article/pii/S1434841123003333

[99] S. Al-Semari and K. Biyari, "Trellis coded modulation with outer RS codes for communication over rayleigh fading channels," in *Proceedings of IEEE Singapore International Conference on Networks/ International Conference on Information Engineering '93*, vol. 2, 1993, pp. 717–720 vol.2.

[100] Daniel J. Costello Jr. and G. David Forney Jr., "Channel Coding: The Road to Channel Capacity," *Proceedings of the IEEE*, vol. 95, pp. 1150 – 1177, Jul. 2007. [Online]. Available: http://arxiv.org/abs/cs/0611112

[101] G. S. Mitchell, "Investigation of Hamming, Reed-Solomon, and Turbo Forward Error Correcting Codes," 2009. [Online]. Available: https://api.semanticscholar.org/CorpusID:60057036

[102] S. Lin and D. Costello and M. Miller, "Automatic repeat request error control schemes," *Comm. Mag.*, vol. 22, no. 12, pp. 5–17, 1984. [Online]. Available: http://dx.doi.org/10.1109/MCOM.1984.1091865

[103] E. Weldon, "An improved selective-repeat arq strategy," *IEEE Transactions on Communications*, vol. 30, no. 3, pp. 480–486, March 1982.

[104] S. Lin and P. Yu, "A hybrid arq scheme with parity retransmission for error control of satellite channels," *IEEE Transactions on Communications*, vol. 30, no. 7, pp. 1701–1719, July 1982.

[105] S. B. Wicker, "Hybrid-arq reed-solomon coding in an adaptive rate system," in *IEEE International Conference on Communications, World Prosperity Through Communications,*, June 1989, pp. 1383–1387 vol.3.

[106] P. Frenger, S. Parkvall, and E. Dahlman, "Performance comparison of harq with chase combining and incremental redundancy for hsdpa," in *IEEE 54th Vehicular Technology Conference. VTC Fall 2001. Proceedings (Cat. No.01CH37211)*, vol. 3, Oct 2001, pp. 1829–1833 vol.3.

[107] W. Yafeng, Z. Lei, and Y. Dacheng, "Performance analysis of type iii harq with turbo codes," in *The 57th IEEE Semiannual Vehicular Technology Conference, 2003. VTC 2003-Spring.*, vol. 4, April 2003, pp. 2740–2744 vol.4.

[108] J. S. Harsini, F. Lahouti, M. Levorato, and M. Zorzi, "Analysis of non-cooperative and cooperative type ii hybrid arq protocols with amc over correlated fading channels," *IEEE Transactions on Wireless Communications*, vol. 10, no. 3, pp. 877–889, March 2011.

[109] E. Zedini and A. Chelli and M. Alouini, "On the performance analysis of hybrid ARQ with incremental redundancy and with code combining over free-space optical channels with pointing errors," *IEEE Photonics Journal*, vol. 6, no. 4, pp. 1–18, Aug 2014.

[110] A. R. Hammons and F. M. Davidson, "On the design of automatic repeat request protocols for turbulent free-space optical links," *MILCOM 2010 MILITARY COMMUNICATIONS CONFERENCE*, pp. 808–813, 2010. [Online]. Available: https://api.semanticscholar.org/CorpusID:22300039

[111] J. Yin, H. Liu, R. Huang, Z. Gao, and Z. Wei, "Performance of a ppm hard decision-based ARQ-FSO system in a weak turbulence channel," *Chin. Opt. Lett.*, vol. 15, no. 6, p. 060101, Jun 2017. [Online]. Available: http://col.osa.org/abstract.cfm?URI=col-15-6-060101

[112] A. Touati, M. O. Hasna, and F. Touati, "Harq performance over fso channels with atmospheric fading and pointing errors," in *2018 14th International Wireless Communications Mobile Computing Conference (IWCMC)*, June 2018, pp. 158–163.

[113] Hoang D. Le and Vuong V. Mai and Chuyen T. Nguyen and Anh T. Pham, "Design and analysis of sliding window arq protocols with rate adaptation for burst transmission over fso turbulence channels," *J. Opt. Commun. Netw.*, vol. 11, no. 5, pp. 151–163, May 2019. [Online]. Available: http://jocn.osa.org/abstract.cfm?URI=jocn-11-5-151

[114] O. Aboelala, I. E. Lee, and G. C. Chung, "A Survey of Hybrid Free Space Optics (FSO) Communication Networks to Achieve 5G Connectivity for Backhauling," *Entropy*, vol. 24, no. 11, 2022. [Online]. Available: https://www.mdpi.com/1099-4300/24/11/1573

[115] H. Moradi, M. Falahpour, H. H. Refai, P. G. LoPresti, and M. Atiquzzaman, "Ber analysis of optical wireless signals through lognormal fading channels with perfect csi," in *17th International Conference on Telecommunications*, April 2010, pp. 493–497.

[116] G. S. H. De Silva, W. G. Cowley, and G. Lechner, "Using channel state information for low-latency applications in free-space optical communication," in *2016 Australian Communications Theory Workshop (AusCTW)*, Jan 2016, pp. 7–12.

[117] M. Petkovic, G. T. Djordjevic, and I. B. Djordjevic, "Analysis of mixed RF/FSO system with imperfect csi estimation," in *2017 19th International Conference on Transparent Optical Networks (ICTON)*, Jul. 2017, pp. 1–7.

[118] T. Eyceoz and A. Duel-Hallen and H. Hallen, "Deterministic channel modeling and long range prediction of fast fading mobile radio channels," *IEEE Communications Letters*, vol. 2, no. 9, pp. 254–256, Sep. 1998.

[119] H. Viswanathan, "Capacity of markov channels with receiver csi and delayed feedback," *IEEE Transactions on Information Theory*, vol. 45, no. 2, pp. 761–771, March 1999.

[120] K. Haesik, *Channel Estimation and Equalization*, 1st ed. Wiley Telecom, 2015, pp. 279–299.

[121] G. Caire and D. Tuninetti, "The throughput of hybrid-arq protocols for the gaussian collision channel," *IEEE Transactions on Information Theory*, vol. 47, no. 5, pp. 1971–1988, July 2001.

[122] T. Koch, “Is the assumption of perfect channel-state information in fading channels a good assumption?” in *2009 2nd International Symposium on Applied Sciences in Biomedical and Communication Technologies*, Nov 2009, pp. 1–6.

[123] R. Tandon, S. Mohajer, H. V. Poor, and Shlomo Shamai, “Feedback and delayed csi can be as good as perfect csi,” in *2012 IEEE International Conference on Communications (ICC)*, June 2012, pp. 2355–2359.

[124] J. B. Andersen and J. Jensen and S. H. Jensen and F. Frederiksen, “Prediction of future fading based on past measurements,” in *Gateway to 21st Century Communications Village. VTC 1999-Fall. IEEE VTS 50th Vehicular Technology Conference (Cat. No.99CH36324)*, vol. 1, Sep. 1999, pp. 151–155 vol.1.

[125] A. Duel-Hallen and and H. Hallen, “Long-range prediction of fading signals,” *IEEE Signal Processing Magazine*, vol. 17, no. 3, pp. 62–75, May 2000.

[126] R.-F. Liao, H. Wen, J. Wu, H. Song, F. Pan, and L. Dong, “The rayleigh fading channel prediction via deep learning,” *Wireless Communications and Mobile Computing*, vol. 2018, pp. 1–11, 07 2018.

[127] Z. Shen, J. G. Andrews, and B. L. Evans, “Short range wireless channel prediction using local information,” 2003.

[128] J. Horwath, N. Perlot, D. Giggenbach, and R. Jungling, “Numerical simulations of beam propagation through optical turbulence for high-altitude platform crosslinks,” pp. 243–252, 2004. [Online]. Available: http://dx.doi.org/10.1117/12.529282

[129] N. Perlot, J. Horwath, and R. Juengling, “Modeling wind in simulations of atmospheric optical propagation,” pp. 140–150, 2005. [Online]. Available: http://dx.doi.org/10.1117/12.590700

[130] J. M. Martin and S. M. Flatté, “Simulation of point-source scintillation through three-dimensional random media,” *J. Opt. Soc. Am. A*, vol. 7, no. 5, pp. 838–847, May 1990. [Online]. Available: http://www.osapublishing.org/josaa/abstract.cfm?URI=josaa-7-5-838

[131] U. Gujar and R. Kavanagh, “Generation of random signals with specified probability density functions and power density spectra,” *IEEE Transactions on Automatic Control*, vol. 13, no. 6, pp. 716–719, 1968.

[132] A. Varga, “The OMNET++ discrete event simulation system,” *Proc. ESM’2001*, vol. 9, 01 2001.

[133] A. Varga and R. Hornig, "An overview of the OMNeT++ simulation environment," in *Proceedings of the 1st International Conference on Simulation Tools and Techniques for Communications, Networks and Systems and Workshops*, ser. Simutools '08. ICST, Brussels, Belgium, Belgium: ICST (Institute for Computer Sciences, Social-Informatics and Telecommunications Engineering), 2008, pp. 60:1–60:10. [Online]. Available: http://dl.acm.org/citation.cfm?id=1416222.1416290

[134] Bowerman, P.N. and Scheuer, E.M., "Calculation of the binomial survivor function (reliability applications)," *IEEE Transactions on Reliability*, vol. 39, no. 2, pp. 162–166, 1990.

[135] K. Kiasaleh, "Hybrid arq receiver for packet communications over free-space optical channels," 2006. [Online]. Available: https://doi.org/10.1117/12.681355

[136] C. Kose and T. R. Halford, "Incremental redundancy hybrid arq protocol design for fso links," in *MILCOM 2009 - 2009 IEEE Military Communications Conference*, Oct 2009, pp. 1–7.

[137] K. Kiasaleh, "Hybrid arq for fso communications through turbulent atmosphere," *IEEE Communications Letters*, vol. 14, no. 9, pp. 866–868, Sep. 2010.

[138] R. E. Good, R. R. Beland, E. A. Murphy, J. Brown, and E. M. Dewan, "Atmospheric Models Of Optical Turbulence," in *Defense, Security, and Sensing*, 1988. [Online]. Available: https://api.semanticscholar.org/CorpusID:124756999